SYNTHESIS AND MOLECULAR PROPERTIES OF NEW MgCl$_2$ BASED MOLECULAR ADDUCTS TOWARDS CATALYTIC POLYOLEFIN PRODUCTION

A THESIS SUBMITTED TO THE

UNIVERSITY OF PUNE

FOR THE DEGREE OF

DOCTOR OF PHILOSOPHY

IN CHEMISTRY

BY

S. EDWIN GNANAKUMAR

CATALYSIS DIVISION

NATIONAL CHEMICAL LABORATORY

PUNE 411 008

INDIA

Dr. CHINNAKONDA S. GOPINATH

(RESEARCH GUIDE)

June 2013

DECLARATION BY RESEARCH SCHOLAR

I hereby declare that the thesis "**Synthesis and Molecular Properties of New MgCl$_2$ based Molecular Adducts Towards Catalytic Polyolefin Production"** submitted for the degree of Doctor of Philosophy to the University of Pune has been carried out by me at the Catalysis and Inorganic Chemistry Division, National Chemical Laboratory, Pune – 411 008, India, under the supervision of Dr. Chinnakonda S. Gopinath. Such material as has been obtained by other sources has been duly acknowledged in this thesis. I declare that the present work or any part thereof has not been submitted to any other University for the award of any other degree or diploma.

Date: June 17, 2013   **S. Edwin Gnanakumar**
Catalysis Division,
National Chemical Laboratory,
Pune 411 008,
Maharashtra,
India

CERTIFICATE BY RESEARCH GUIDE

This is to certify that the work incorporated in the thesis entitled, "**Synthesis and Molecular Properties of New MgCl$_2$ based Molecular Adducts Towards Catalytic Polyolefin Production"** submitted by **S. Edwin Gnanakumar,** for the Degree of **Doctor of Philosophy,** was carried out by the candidate under my supervision in the Catalysis Division, National Chemical Laboratory, Pune – 411 008, India. Such material as has been obtained from other sources has been duly acknowledged in the thesis. To the best of my knowledge, the present work or any part thereof has not been submitted to any other University for the award of any other degree or diploma.

Date: June 17, 2013   **Dr. C. S. Gopinath**
Catalysis Division   **(Research Supervisor)**
National Chemical Laboratory,
Pune 411 008,
Maharashtra,
India

DEDICATED TO MY DAD

Acknowledgement

Pune   *S. Edwin Gnanakumar*

June-2013

Table of Contents

Chapter 4: Bulky $MgCl_2.xROH$ molecular adducts and its influence in PE production
Part A: $MgCl_2.6C_6H_{11}OH$

Chapter 5: Ether and bifunctional molecular adduct of $MgCl_2$ and its structural studies

Part A:$MgCl_2.xTHF$ (x = 1.5, 2 and 4)

Part B: $MgCl_2.2THFA$

Chapter 6: Conclusions and Future Outlook

List of Publication

Abbreviation

Z-N	Ziegler-Natta
PP	Polypropylene
PE	Polyethylene
ID	Internal electron donor
ED	External electron donor
LB	Lewis Base
EtOH	Ethanol
BzOH	Benzyl alcohol
CyOH	Cylcohexyl alcohol
9-FM	9-fluorenemethanol
THF	Tetrahydrofuran
THFA	Tetrahydrofurfuryl alcohol
MgMeOH	$MgCl_2.6CH_3OH$
MgEtOH	$MgCl_2 \cdot 6EtOH$
MgBzOH	$MgCl_2 \cdot 6BzOH$
MgCyOH	$MgCl_2.6CyOH$
MgTHFA	$MgCl_2.2THFA$
XRD	X-Ray diffraction
NMR	Nuclear Magnetic Resonance
TGA	Thermo gravimetric analysis
DTA	Differential thermal analysis
BET	Brunauer-Emmett-Teller
BJH	Barrett-Joyner-Halenda
SEM	Scanning electron microscope
GPC	Gel permeation chromatography
CPMAS	Cross-polarization magic angle spinning
HPDEC	High power proton decoupling

Chapter 1

Introduction

1. Introduction

1.1 Discovery of Ziegler-Natta catalyst

Before the discovery of Ziegler-Natta (Z-N) catalyst, polyolefin productions have been carried out at extremely harsh condition such as 1000-3000 atm pressure and 250 ^{o}C. In the history of polyolefin production one of the huge success is connected with the name of Ziegler and Natta. It was an accidental discovery by Prof. Karl Ziegler in 1953 and he found the combination of $TiCl_3$ and Et_3Al worked for ethylene polymerization reaction [1, 2]. Few months later, Prof. Giulio Natta used the same catalyst for propylene polymerization. Propylene polymerization results with mixture of stereoisomers of polypropylene [3, 4]. Both of them shared Noble Prize in 1963 for their great contribution in polyolefin production. After the name of the discoverers the ethylene and propylene polymerization catalysts are commonly referred to Ziegler and Ziegler-Natta (Z-N) catalysts, respectively. Polyolefin industries started to grow rapidly ever since the discovery of $TiCl_4$ derived catalysts in late 1950s. Enormous effort has been made to increase the productivity of catalyst for ethylene polymerization and stereospecificity for propylene polymerization. In the commercial production of polyolefins, conventional Ziegler and Z-N catalysts have the limitation of requiring an additional step for the removal of the catalyst residue (de-ashing) and separation of stereoregular polymers from the product [5].

Depending on the catalyst solubility in the reaction medium Z-N catalyst was divided into two classes,

1. Heterogeneous supported catalytic system based on titanium compounds combination with alkyl aluminium as co catalyst for olefin polymerization. This class of Z-N catalyst have been used majority in the industrial production. Commercial catalysts are supported with a high surface area material. Both $TiCl_4$ and $TiCl_3$ give active catalysts [6, 7].

2. Homogenous catalysts based on Ti, Zr and Hf complexes. Along with this class of catalyst, methylalumoxane (MAO) has been used as co catalyst. Traditionally these catalysts include metallocenes but also feature multidentate oxygen and nitrogen based ligands [8].

1.2 Mechanism of Z-N catalyst
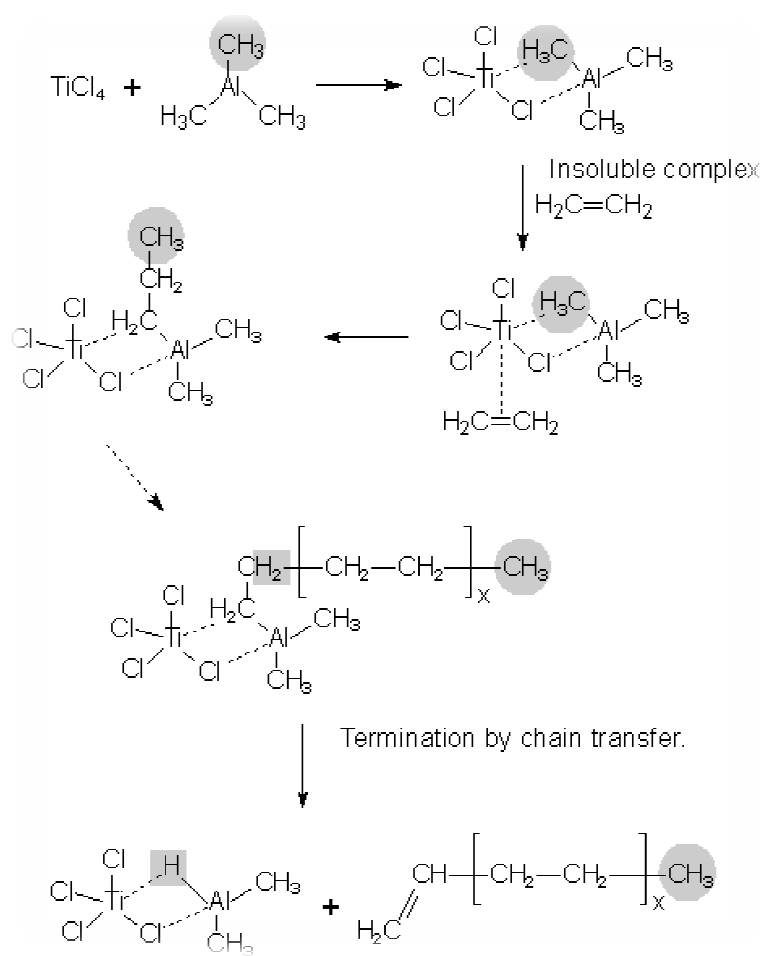
Figure 1.1: *Mechanism of heterogeneous Z-N catalyst for 1-olefin polymerization [9].*

The mechanism of heterogeneous Z-N catalyst is poorly understood because it takes place on the surface of an insoluble particle, a complicated and difficult circumstances to investigate experimentally. The mechanism shown below is one of several models proposed to at least partially explain the action of the Z-N systems, but it is only an approximation of

the more complex process that actually occurs. Mostly accepted mechanism in Z-N catalyst is Cossee-Arlman mechanism [10-13] for the C-C bond formation of the polymer. Alkene polymerization on Ti-solid catalyst occurs on the Ti centre located on the outer surface of the catalyst crystallites. Some of the Ti atoms on the surface of the crystallite will react with cocatalyst i.e., organoaluminum to form Ti-C bond. At the same time alkene will coordinate with the vacant site of Ti over the crystallite surface. After this step insertion of alkene in Ti-C bond will occur. The above steps will be followed successively many thousand times to form long polymer chain.

1.3 MgCl$_2$ supported Z-N catalyst

In late 1960s Kashiwa's discovery of MgCl$_2$ supported TiCl$_4$ catalyst has boosted up the polymer catalyst field because of the innovative improvement in the polymer productivity and drastic cut down in the production cost [14]. Kashiwa's approach was to enhance the activity as well as to find a suitable support which should have the same crystal structure of TiCl$_3$, and the same can be plated with Ti^{n+} active species in TiCl$_4$ solution. After the investigation over many crystal structures, MgCl$_2$ found to have the same crystal structure (structure) that of TiCl$_3$, and Mg^{2+} and Ti^{4+} having the very similar ionic radii, 0.68 and 0.65 Å, respectively. Active sites are located on the edges and surface of crystalline structure of MgCl$_2$. This heterogeneous MgCl$_2$ supported TiCl$_4$ catalyst has high surface area and pore volume, hence gives extremely high activity, and higher isotactic index for polypropylene (PP) compared to conventional Z-N catalysts. Among the commercial polyolefin catalyst, MgCl$_2$ supported Z-N catalyst constitute major portion due to its multifold higher activity and stereospecificity and the reduction of the steps involved polymerization process with polyolefin industry. Until 2004, more than 51% of industrial production for polyethylene (PE) and about 95% of industrial PP production prefer to use MgCl$_2$ supported TiCl$_4$ catalyst [5, 15].
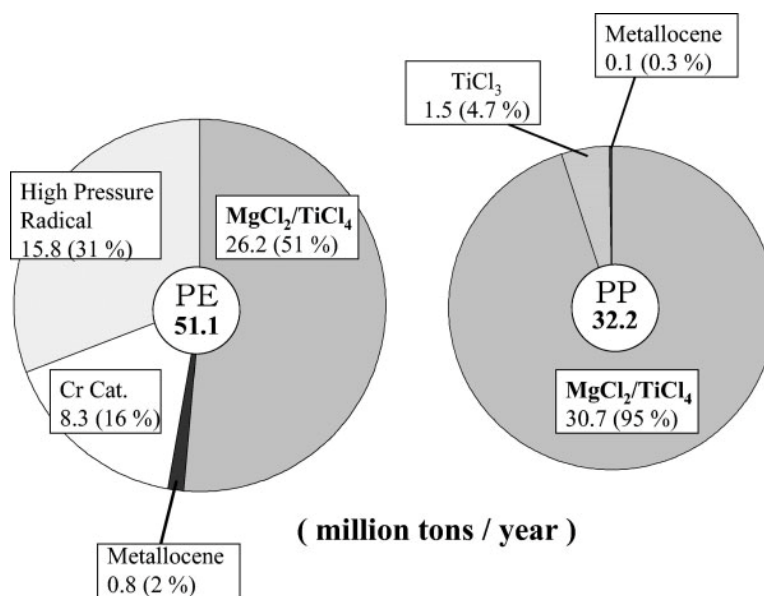
Figure 1.2: *World handling of catalysts for PE and PP production [15].*

1.4 Relevant Structural Features of TiCl$_3$ and MgCl$_2$

TiCl$_3$ exists in four crystalline forms or polymorphs. In all crystalline form titanium present in an octahedral coordination sphere. These forms can be distinguished by crystallographic structure as well as by their magnetic properties. β-TiCl$_3$ crystallizes as brown needles with "chain like" structure. β-TiCl$_3$ structure consists of chains of TiCl$_6$ octahedra that share opposite faces such that the closest Ti—Ti distance is 2.91 Å. This short distance indicates strong metal-metal interactions [16]. The other α, β, and δ-TiCl$_3$ forms having "layered" structure are violet in colour [17, 18]. In α-TiCl$_3$, the chloride anions are hexagonal close-packed. In γ-TiCl$_3$, the chlorides anions are cubic close-packed. Finally, disorder in shift successions, causes an intermediate between alpha and gamma structures, called the δ- TiCl$_3$ form. The TiCl$_6$ share edges in each form, with 3.60 Å being the shortest distance between the titanium cations. This large distance between titanium cations precludes direct metal-metal bonding [19].

α-TiCl$_3$ can be prepared by reduction of TiCl$_4$ with aluminium powder or H$_2$. β -TiCl$_3$ can be prepared by the reaction between TiCl$_4$ and AlR$_3$ and it can be converted to γ-TiCl$_3$ by

heating. The latter catalyst has much higher stereoregulating ability in propylene polymerization, while β-TiCl₃ is an effective catalyst for the production of cis-1,4-polyisoprene. δ-TiCl₃ form can be prepared by long-lasting grinding of γ - or α-TiCl₃. δ-TiCl₃ has a more disordered structure because of sliding of Cl–Ti–Cl triple layers during mechanical activation [20, 21].

Table 1.1: *Comparision between the crystallographic parameters of $MgCl_2$ and $TiCl_3$ crystalline modifications.*

Product	α-MgCl₂	γ-TiCl₃	β-MgCl₂	α-TiCl₃
Structure	Cubic close packed layer structure		Hexagonal close packed layer structure	
Lattice parameter (Å)	a = b = 3.63 c = 17.79	a' = b' = 3.54 a' = a/√3 c = 17.58	a = b = 3.64 c = 5.93	a' = b' = 3.56 a' = a/√3 c = 5.87 c' = c/3
Crystalline form	Rhombohedral		Rhombohedral	
Space group	R -3 m	P -3₁ 12 R 3 m for Cl atoms	P -3 m 1	P -3 m 1
Specific gravity (g/cm³)	2.33	2.71	2.32	2.71
Cation coordination	Octahedral		Octahedral	
Atomic distance (Å)	Mg-Cl = 2.56	Ti-Cl = 2.51	Mg-Cl = 2.51	Ti-Cl = 2.51

$MgCl_2$ crystallizes in the cadmium chloride motif, which features octahedral Mg^{2+}. Anhydrous $MgCl_2$ is a Lewis acid, although a very weak one. In $MgCl_2$, the atoms are arranged in two-dimensional hexagonal groups, with repetition periods $a = b = 3.64$ Å, $\gamma = 120^o$ which represent 'structural' triple layers. In these structural layers, the magnesium atoms are packed between two layers of chlorine atoms, to which the magnesium atoms are octahedrally coordinated and strongly bonded. The stacking of structural layers along the

direction normal to the layers, at a distance of 5.90 Å, in accordance with a regular hexagonal structure of packing of the bulkier halogen atoms, gives rise to the α-MgCl$_2$ (c = 17.7 Å) and β-MgCl$_2$ (c = 5.90 Å) modifications [22, 23].

In the δ modifications of MgCl$_2$, the crystal dimensions become smaller and structurally disordered, related to the way the Cl–Mg–Cl sandwich layers are piled up along the c axis. In these disordered active forms of MgCl$_2$, successive Cl–Mg–Cl sandwich layers are stacked along the *c*-axis according to a hexagonal sequence, or rotated by ± 60$^{\mathrm{o}}$ with regard to each other. In addition, the catalytic activity becomes higher [22,23].

Table 1.2: *Comparison between the crystallographic parameters of the active forms of MgCl$_2$ and TiCl$_3$ crystalline modifications.*

Product	δ-MgCl$_2$	δ-TiCl$_3$
Structure	Close packed layered structure with stacking defects	
Lattice parameter (Å)	a = b = 3.63 c = 5.93	a = b = 3.54 c = 5.86
Specific gravity (g/cm^3)	2.33	2.71
Cation coordination	Octahedral	
Atomic distance (Å)	Mg-Cl = 2.57	Ti-Cl = 2.51

1.5 MgCl$_2$ as Z-N catalytic support

A highly active Z-N catalyst was made possible by binding TiCl$_4$ to the surface of anhydrous MgCl$_2$. The stereospecific polymerization of propylene in the industrial process is carried out with Z-N catalysts, in which the active sites are located on the edge faces of MgCl$_2$ crystallites. The discovery of chemically or mechanically activated MgCl$_2$ [24-26] performs as perfect support for the fixation of the titanium chlorides opened a new era in the field of Z-N catalyst in both industrial and academic prospective. *"Super active catalysts"* may be prepared through prolonged milling of crystalline anhydrous MgCl$_2$ (usually in the α-

modification) with a Lewis base (LB), usually referred to as an 'internal donor', before contact with $TiCl_4$. Such catalysts are used in combination with an aluminum alkyl compound as cocatalyst and a second Lewis base, generally called an 'external donor' for olefin polymerization [21, 22]. However, nowadays, the activated $MgCl_2$ support is prepared by chemical means, from magnesium chloride/alcohol complexes or by reaction of magnesium alkyls or alkoxides with other halogenated compounds [21, 22]. Controlled morphology supports are prepared by rapid cooling of emulsions of molten $MgCl_2 \cdot nEtOH$ adducts (n $\cong$ 2–3) in mineral oil. This process gives rise to spherical particles with a narrow size distribution.

1.6 Electron Donor

The use of $TiCl_4$ (catalyst) and Et_3Al (co-catalyst) alone was found to produce polyolefin but with very low productivity and stereo specificity. This problem was overcome by the addition of correct Lewis base (electron donors), by which it possible to obtain highly active and stereoselective catalysts.

In $MgCl_2$ supported Z-N catalysis, electron donor are classified into two types,

(i) **Internal Electron Donor (ID):** This is supported on the $MgCl_2$ surface with $TiCl_4$ during catalyst preparation

(ii) **External Electron Donor (ED):** This is introduced with Et_3Al at the start of propylene polymerization.

It was generally accepted that ID was displaced from the catalyst surface by the reaction with Et_3Al, and ED had a function of supplying electron-donor molecules on the catalyst surface. By finding such a combination of electron donors, one can end up with highly active and stereospecific Z-N catalyst. In general, the effect of these donors is usually in: (i) catalyst activity, (ii) catalyst stereoselectivity, and (iii) polymer molecular weight distribution [15]. The first catalyst system, ethyl benzoate has been used as internal donor in

combination with a second aromatic ester such as methyl p-toluate as external donor [27]. Subsequently, catalysts containing a diester (e.g. diisobutyl phthalate) as internal donor were developed, used in combination with an alkoxysilane external donor of type $RR´Si(OMe)_2$ or $RSi(OMe)_3$ [28-30]. It was proved that a dialkyl phthalate as ID was displaced from the surface of active catalyst, and an alkoxysilane as ED was fixed on the catalyst surface as a stereospecificity improver instead of ID [31–34]. The function of ED is not only improve the stereospcificity of the catalyst but also to enhance the molecular weight of polypropylene produced [35, 36]. The combination $MgCl_2/TiCl_4$/phthalate ester – AlR_3 – alkoxysilane is presently the most extensively used catalyst system in PP manufacture.
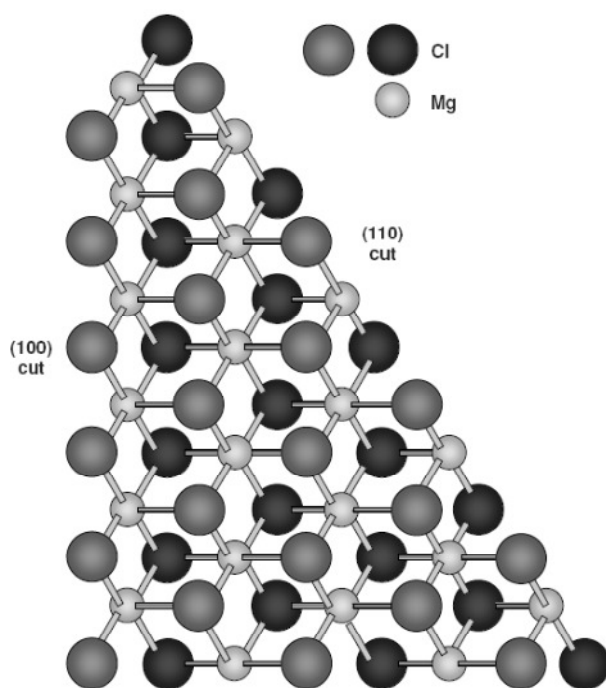
Figure 1.3*: Model of $MgCl_2$ layer showing the (100) and (110) lateral cuts [21, 37].*

ID plays dual role in $MgCl_2$ supported Z-N catalysis. First role is to stabilize small primary crystallites of magnesium chloride. Second role is to control the amount and distribution of $TiCl_4$ in the final catalyst. The reaction of a magnesium chloride support with $TiCl_4$ leads to adsorption of the latter on lateral cleavage surfaces of $MgCl_2$, such as the (110)

and (100) cuts shown in Figure 1.3. As indicated by Giannini [37], the magnesium atoms on these lateral cleavage surfaces are coordinated with 4 or 5 chlorine atoms, as opposed to 6 chlorine atoms in the bulk of the crystal. These lateral cuts correspond to (110) and (100) faces of $MgCl_2$, as shown in Figure 1.3.

However, very recently, the crystal structure of $MgCl_2$ supports has been re-evaluated by Busico et al. who concluded that the surface with five-coordinate Mg cations should be indexed as (104) rather than (100) [38]. Periodic DFT calculations indicated that the (104) surface has relatively low energy and is the dominant lateral surface in well-formed large crystals, as well as in activated supports prepared by ball milling [38].

It has been recommended that bridged, dinuclear Ti_2Cl_8 species can coordinate to the (100) facet of $MgCl_2$ and lead to the formation of chiral, isospecific active species (Figure 1.4). It is pointed out that Ti_2Cl_6 species formed by reduction upon contact with $AlEt_3$ would be similar to analogous species in $TiCl_3$ catalysts [39, 40]. Consequently, it has been proposed [41] that a probable characteristic of the ID is favoured coordination on the more acidic (110) face of $MgCl_2$, such that this face is prevailingly occupied by donor and the (100) facet is prevailingly occupied by Ti_2Cl_8 dimers. Recent studies over [42, 43] mechanistic and modelling have suggested valid evidence for the formation of the active species on the (110) cut of $MgCl_2$.
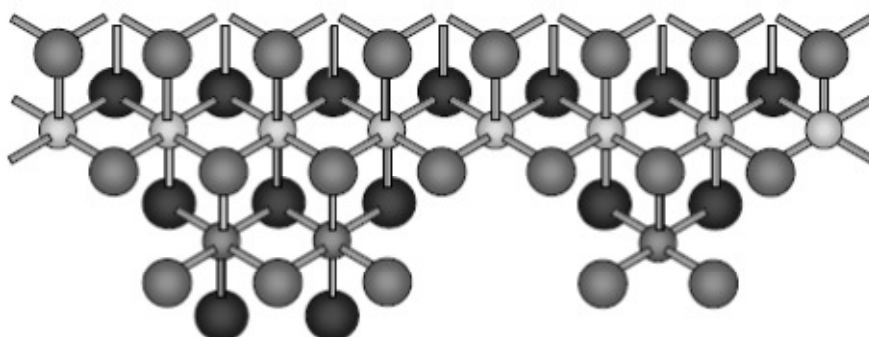
Figure 1.4: *Model showing dimeric and monomeric Ti species on a (100) lateral cut of $MgCl_2$ [21, 37].*

Studies indicated that a monoester ID such as ethyl benzoate is coordinated to $MgCl_2$ and not to $TiCl_4$ in Z-N catalysts [44]. In the search for donors giving catalysts with improved performance, it was thought [45] that bidentate donors should be able to form strong chelating complexes with tetracoordinate Mg atoms on the (110) face of $MgCl_2$, or binuclear complexes with two pentacoordinate Mg atoms on the (100) facet. This initiated the development of the $MgCl_2/TiCl_4$/phthalate ester catalysts, used as mentioned above in combination with an alkoxysilane as ED. However, effectiveness of a catalyst system depends more on the combination/choice of donors rather than on the individual internal or external donor [46].

The search for $MgCl_2$-supported catalysts which do not require the utilization of an external donor led to the identification of bidentate internal donors which not only had the right oxygen-oxygen distance for effective coordination with $MgCl_2$ but which, in contrast to phthalate esters, were not removed from the support upon contact with $AlEt_3$ and which were not reactive with $TiCl_4$ throughout catalyst preparation. It was found [45, 47-49] that certain 2,2-disubstituted-1,3-dimethoxypropanes satisfied all these requirements. The best performance in terms of productivity and isotacticity was obtained when bulky substituents in the 2-position resulted in the diether having a most probable conformation [50] with an oxygen-oxygen distance in the range 2.8 - 3.2 Å. The successive "generations" of high activity $MgCl_2$-supported catalyst systems for polypropylene are summarized below [21]:

1. $MgCl_2/TiCl_4$/ethyl benzoate - AlR_3 - aromatic ester

2. $MgCl_2/TiCl_4$/phthalate ester - AlR_3 - alkoxysilane

3. $MgCl_2/TiCl_4$/diether - AlR_3

1.7 Generations of Heterogeneous Z-N catalyst

Till now there are 6 generations of Z-N catalysts have been invented and being used

for polyolefin production. The difference in these generations is in: (i) catalyst, (ii) support, and (iii) donors. A summary of different generations is in **Table 1.3** [21, 51].

Generation (Year)	Catalyst composition	Productivity (kg PP/g cat)	Isotactic Index (%)	Remarks
1st (1954)	δ-TiCl$_3$ * 0,33AlCl$_3$ + AlEt$_2$Cl	2-4	90-94	No morphological control, deashing and atactic removal necessary
2nd (1970)	δ-TiCl$_3$ + AlEt$_2$Cl	10-15	94-97	Granular catalyst, deashing necessary
(1968	MgCl$_2$/TiCl$_4$ + AlR$_3$		40	First MgCl$_2$ based catalyst for PE, very low stereo control
3rd (1968)	MgCl$_2$/TiCl$_4$/Benzoate + AlR$_3$/Benzoate	15-30	95-97	First MgCl$_2$ based catalyst for PE, very low stereo control low, H$_2$ response, broad MWD
4th (1980)	MgCl$_2$/TiCl$_4$/Phtalate + AlR$_3$/Silane	40-70	95-99	Spherical catalyst with controlled porosity, medium medium-high stereo control, medium H$_2$ response, medium MWD
5th 1988)	MgCl$_2$/TiCl$_4$/Diether + AlR$_3$/Silane (opt.)	70-130	95-99	Same as 4th generation but very high activity, narrow MWD, excellent H$_2$ response
6th (1999)	MgCl$_2$/TiCl$_4$/ Succinate + AlR$_3$/Silane	40-70	95-99	Same as 4th generation but broad MWD

1.8 Challenges in Heterogeneous Z-N catalysis

Though technologically Z–N catalyst has matured to a sophisticated level, the molecular science behind the understading of each components in the complication Z-N

catalytic system is very much limited. In detail the role of support and various key interactions of the active components in the heterogeneous Z−N catalyst is still unclear [43, 52−57]. Some of the key challenges needs to be addressed to understand the catalytic system clearly in order to develop even better catalyst in the coming days. In fact it is a big challenge to techniques, such as, surface science, structural, spectroscopy, and theoretical methods to shed more light on the following aspects [58-62].

- ❖ The precise structure of active sites on the specific surface of $MgCl_2$

- ❖ Exact role of electron donors on the activation of $MgCl_2$ surface.

- ❖ Nature of the electron donor and stoichiometry around $MgCl_2$ and its influence in the activity

- ❖ Role of alkyl aluminium cocatalysts.

- ❖ Exact oxidation state of Ti^{n+} present in the active catalyst.

Practical difficulties associated with the present Z-N catalytic system is partly due to the complex nature of active sites of $TiCl_x$ on $MgCl_2$ under polymerization conditions, low content of the active sites and the high sensitivity of catalyst components present in Z−N systems toward the oxygen and atmosphere at ambient conditions. Drawbacks associated with huge gap between the model catalyst and real word catalyst reduces the importance of using modern surface science and spectroscopic techniques. However efforts are on to overcome the shortcomings of various techniques, used to acquire the valuable information regarding the components of advanced Z-N system at ambient conditions by employing actual real-world catalysts or models close to that [63].

1. 9 Objective of the Thesis

A survey of the reports for polyolefin production by Z-N catalyst since 1950s shows $MgCl_2$ is the successful support to attain maximum activity as well as stereospecificity. The important point for the improved performances of the supported catalyst is the nature of the

MgCl$_2$ precursors, obtained as complexes with Lewis bases, which undergo direct titanation. Among other features, the type of Lewis base and Lewis base/MgCl$_2$ ratios in the precursor determine, the activity and the isotacticity degree of the resulting polymer. two step process involving removal of alcohol to form MgCl$_2$ and subsequent addition of TiCl$_4$ leads to modest catalytic performances of MgCl$_2$ supported Z-N catalyst. Thus, the removal of alcohol from the solvate could be a method for producing nanostructures tailored for the olefin polymerization catalytic system [57]. The aim of the current thesis is to contribute towards a deeper understanding of MgCl$_2$ precursor structure and active catalyst, relating to polymerization activity and polymer properties; thereby to a greater control, of the structure of MgCl$_2$/ROH crystalline adducts that, until now, has not been resolved, and that takes part in the catalytic system of Z-N polymerization.

- ❖ To observe how the different alcohols as Lewis base (methanol, ethanol, cylcohexanol, benzyl alcohol and 9-Fluorenemethanol) can influence the structure of MgCl$_2$ precursor and thereby affecting the polymerization activity.

- ❖ To understand how different stoichiometry of alcohol around MgCl$_2$ precursor for particular Lewis base (methanol) can affect the polymerization activity.

- ❖ To notice how MgCl$_2$ precursor having different functional group of Lewis base such as ether and bifunctional Lewis base having both alcohol and ether functionalities can influence the polymerization activity.

For the above understanding, each components in the complicated system presented in the Z-N catalyst (MgCl$_2$/Lewis Base – TiCl$_4$/Et$_3$Al) needs to be studies in detail. In order to understand the complex system consisting of multicomponents, which are interacting with one another, it is essential to understand the physicochemical properties of each component and then allow them to interact together with increasing complexity [57]. The present thesis describes a synthesis procedure to make well-defined single phase MgCl$_2$·ROH molecular

adduct and it has been used as a support material to synthesize active Z–N catalyst. Structural insights of molecular adduct and active Z-N catalyst has been examined through structural, spectroscopic and textural studies toward a better understanding of Z–N catalysis in polymerization reaction at molecular level.

1.10 Outline of the Thesis

CHAPTER 1 This chapter presents a brief introduction about the fruits of heterogeneous catalysis especially heterogeneous olefin polymerization Z-N catalyst in the modern world, Importance of Z-N catalytic system in industrial process and history of invention till $MgCl_2$ supported Z-N catalyst. Also this chapter describes the importance of structure of $MgCl_2$ and its different crystalline phase as supporting material for Z-N catalyst. Role of Lewis base has been described in this chapter. Finally we concluded this chapter by mentioning various challenging problems need to be solved in the understanding of heterogeneous Z-N catalyst, in order to make better or design an efficient supported olefin polymerization Z-N catalyst followed by scope and outline of the thesis.

CHAPTER 2 deals with the synthesis strategies of various molecular adducts such as $MgCl_2.xCH_3OH$, $MgCl_2.6C_6H_5CH_2OH$, $MgCl_2.6C_6H_{11}OH$, $MgCl_2.xEtOH.n9FM$, $MgCl_2.2THFA$ and different stoichiometries of $MgCl_2.xTHF$ adduct by azeotropic distillation method. Above molecular adducts have been used to prepare titanated active Z-N catalyst. This chapter describes the details of the catalytic activity studies of ethylene polymerization using different co-catalyst and reaction conditions. Also this chapter briefly describes the working principle of various physico-chemical methods used such as Raman spectroscopy, N_2 adsorption-desorption isotherm studies, solid state NMR, and gel permeation chromatography etc.

CHAPTER 3 $MgCl_2.6CH_3OH$ and its different stoichiometries i.e.,

MgCl$_2$.xCH$_3$OH, and their corresponding titanated active catalysts have been structurally thoroughly characterised by various physico-chemical methods. All the titanated active catalyst showing less crystalline in nature with δ-MgCl$_2$ present as a support due to disturbance in Cl-Mg-Cl triple layer structure. Active catalyst synthesized from different stoichiometries show different surface area with different Ti loading. All the active catalysts showing type-IV H3- mesoporosity with narrow pore size distribution. Among all titanated catalysts, active catalyst derived from MgCl$_2$.1.3CH$_3$OH having highest surface area of 123 m^2/g. Lowest titanium loading (4.9%) observed on active catalyst prepared by the molecular adduct dealcoholated at 105°C (Ti-MgMeOH-105). Ethylene polymerization activity results with different co-catalysts suggested, high yield of PE i.e., 8180 g/mmol of Ti obtained with active catalyst derived from MgCl$_2$.2.9CH$_3$OH (Ti-MgMeOH-105) with Me$_3$Al as a co-catalyst.

CHAPTER 4 is divided into Part A, B and C for Lewis base cylcohexanol, benzyl alcohol and 9-fluorene methanol, respectively. In this chapter different well defined molecular adduct of MgCl$_2$ have been synthesized using different bulky alcohols namely benzyl alcohol, cyclohexanol and 9-fluorene methanol as Lewis base. Titanated active Z-N catalysts were synthesized by routine procedure using corresponding molecular adducts as a support and characterized thoroughly. Titanium content in the active catalyst, surface area, porosity and organic residue present in the final catalyst have been different in each catalyst depends on the Lewis base used to prepare the supporting material. In the case of benzyl alcohol adduct, titanation leads to the formation of benzyl chloride which trapped in the pores of the final catalyst leads higher titantion (17%) followed by poor polymerization activity. But cyclohexanol adduct derived catalyst shows lower titanation (9%) with better surface area (236 m^2/g) leads to better polymerization (1918 g/mmol of Ti with iBu$_3$Al as co-catalyst) results. Studies on 9-fluorene methanol adduct derived catalyst exhibits the highest surface

area (410 g/m^2) and good control over the polymer properties in terms of molecular weight distribution (MWD=6.4 with iBu$_3$Al co-catalyst). This study shows, how the nature of precursor i.e., Lewis base, controls the active catalyst property and thereby polymerization activity and polymer property.

CHAPTER 5 Well defined and various stoichiometries of MgCl$_2$ molecular adduct have been derived from tertrahydrofuran (MgCl$_2$.1.5THF, MgCl$_2$.2THF and MgCl$_2$.4THF) and bi-functional tetrahydrofurfuryl alcohol (MgCl$_2$.2THFA) as Lewis bases. Structural insights for molecular adducts have been derived from various physico-chemcial characterization methods. Ethylene polymerization results have been correlated with the structure of the molecular adduct, amount of titanation and surface area of the active catalyst. Series of results suggests stoichiometry of the adducts as well the functional group on Lewis base exhibit more control over the active sites there by controlling the polymer properties such as MWD.

CHAPTER 6 Summarizes the conclusions derived based on the observation and results obtain from the entire study. Scope of further research work in the area of the present studies has also been described briefly.

1.11 Reference

1. Ziegler, K. Belgian Patent, 533, 362, 1954.
2. Ziegler, K. *Angew. Chem., Int. Ed. Engl.*, **1964,** *76*, 545.
3. Natta, G. *J. Polym. Sci.,* **1955,** *16,* 143.
4. Natta, G. *Angew. Chem., Int. Ed. Engl.,* **1964,** *76,* 553.
5. Kashiwa, N. *Polym. J.,* **1980,** *12,* 603.
6. Hill, A.F. Organotransition Metal Chemistry Wiley-InterScience: New York, **2002,** pp. 136–139.
7. Kissin, Y.V. Alkene Polymerization Reactions with Transition Metal Catalysts" Elsevier: Amsterdam, **2008;** Chapter 4.
8. "Handbook of Transition Metal Polymerization Catalysts" Ray Hoff, Robert T. Mathers, Eds. **2010** John Wiley & Sons.

9. http://chem.chem.rochester.edu/~chem421/zn.htm

10. Cossee, P. J. *J. Catal.,* **1964,** *1,* 80.

11. Arlman, E. J. J. Catal. **1964,** *1,* 89.

12. Arlman, E. J.; Cossee, P. J. Catal, **1964,** *1,* 99.

13. Allegra, G. Die Makromolekulare Chemie, **1971,** *145,* 235.

14. Kashiwa, N.; Fujimura, H.; Tokuzumi, Y. JP Patent 1031698.

15. Kashiwa, N. *J. Polym. Sci., Part A: Polym. Chem.,* **2004,** *42,* 1.

16. http://en.wikipedia.org/wiki/Titanium%28III%29_chloride

17. G. Natta, P. Corradini, and G. Allegra, *J. Polym. Sci.* **1961,** *51,* 399.

18. Boor, J Ziegler–Natta Catalysts and Polymerizations, Academic Press, Inc., New York, **1979.**

19. Greenwood, Norman N.; Earnshaw, Alan. **1997.** Chemistry of the Elements (2nd ed.). Butterworth–Heinemann. ISBN 0080379419.

20. Guidetti, G.; Zannetti, R.; Ajo, D.; Marigo, A.; Vidali, M. *Eur. Polym. J.* **1980,** *16,* 1007 .

21. Chadwick, J.C. Ziegler–Natta Catalysts, Encyclopedia of Polymer Science and Technology, vol. *6,* **2003,** p. 517.

22. Auriemma, F.; De Rosa, C. *J. Appl. Cryst.* **2008,** *41,* 68.

23. Andoni, A. A flat model approach to Ziegler-Natta oleifin polymerization catalysts, PhD Thesis, **2009.**

24. Bart, J. C. *J. Mater. Sci.,* **1995,** *30,* 2809.

25. Coutinho, F.M. B.; Xavier, J. L. L. *Polymer Bulletin.* **1977,** *39,*133.

26. Terano, M. Ishii, K. (1985) Proc Int Symp Fut Asp Olefin Polym Tokyo 25: 277.

27. P.C. Barbè, G. Cecchin, L. Noristi, *Adv. Polym. Sci.* **1987,** *81,* 1.

28. Luciani, L.; Kashiwa, N.; Barbe, P. C.; Toyota, A. JP Patent 1612306 (applied in 1976).

29. Parodi, S.; Noristi, L.; Giannini, U.; Barbe, P. C.; Sacata, U. JP Patent 1962732 (applied in 1981).

30. Ishimaru, N.; Kioka, M.; Toyota, A. JP Patent 2723137 (applied in 1989).

31. Soga, K.; Shiono, T. In Transition Metal Catalyzed Polymerizations; Quirk, R. P., Ed.; Cambridge University Press: New York, **1988;** p 266.

32. Sacchi, M. C.; Tritto, I.; Shan, C.; Mendichi, R.; Noristi, L. *Macromolecules* **1991,** *24,* 6823.

33. Kioka, M.; Kashiwa, N. *J Mol Catal* **1993,** *82,* 11.

34. Noristi, L.; Barbe, P. C.; Baruzzi, G. *Makromol Chem* **1991,** *192,* 1115.

35. Soga, K.; Shiono, T.; Doi, Y. *Makromol Chem* **1988,** *189,* 1531.

36. Seppala, J. V.; Harkonen, M.; Luciani, L. *Makromol Chem* **1989,** *190,* 2535.

37. Simonazzi, T.; Giannini, U. *Gazz. Chim. Ital.***1994,** *124,* 533.

38. Busico, V. ; Causà, M. ; Cipullo, R.; Credendino, R. ; Cutillo, F.; Friederichs, N.; Lamanna, R.; Segre, A. ; Van Axel Castelli, V. *J. Phys. Chem. C* **2008,** *112,* 1081.

39. Corradini, P.; Busico, V. ; Guerra, G.; Kaminsky, W.; Sinn, H. eds., Transition Metals and Organometallics as Catalysts for Olefin Polymerization, Springer-Verlag, Berlin, **1988,** p. 337.

40. Busico,V.; Corradini, P.; De Martino, L.; Proto, A.; Savino, V.; Albizzati*, E. Makromol. Chem.***1985**, 186, 1279.

41. E.P. Moore, Polypropylene Handbook. Polymerization, Characterization, Properties, Processing, Applications, Hanser Publishers, Munich, 1996

42. Giannini, U. *Makromol. Chem. Suppl*. **1981,** *5*, 216.

43. Busico, V.; Causà, M.; Cipullo, R.; Credendino, R..; Cutillo, F.; Friederichs, N.;. Lamanna, R.; Segre, A.; Van Axel Castelli, R. *J. Phys. Chem. C* **2008,** *112* , 1081.

44. Terano, M.; Kataoka, T.; Keii, T. *Makromol. Chem.***1987***,* 188.

45. Albizzati, E.; Giannini, U.; Morini, G.; Smith, C.A.; Zeigler, R.C.; Fink, R..; Mülhaupt, Brintzinger, H.H. eds., Ziegler Catalysts. Recent Scientific Innovations and Technological Improvements, Springer-Verlag, Berlin,**1995,** p- 413.

46. Sacchi, M.C.; Tritto, I.; Shan, C.; Mendichi, R.; Zannoni, G.; Noristi, L. *Macromolecules,* **1991,** *24,* 6823.

47. E. Albizzati, P.C. Barbè, L. Noristi, R. Scordamaglia, L. Barino, U. Giannini, G. Morini (to Himont), Eur. Pat. 361494 Filed 29 Sept. 1989.

48. Morini, G.; Cristofori, A. (to Montell) Eur. Pat. 728724 Filed 21 Feb. 1996.

49. Albizzati, E.; Giannini, U.; Morini, G.; Galimberti, M.; Barino, L.; Scordamaglia,R. *Macromol. Symp.*, **1995**, *89,* 73.

50. Barino, L.; Scordamaglia, R. Macromol. Symp. 89 (1995) 101.

51. Chadwick, J.C.; Garoff, T.; Severn, J.R. Tailor-Made Polymers via Immobilization of Alpha-Olefin Polymerization Catalysts, Eds. Severn, J.R.; Chadwick, J.C.WILEY-VCH, Weinheim, **2008,** Ch. 2

52. Kim, S. H.; Somorjai, G. A. *J. Phys. Chem. B,* **2002,** *106,* 1386.

53. Sobota, P. *Coordin, Chem. Rev.,* **2004,** *248,* 1047.

54. Andoni, A.; Chadwick, J. C.; Milani,S.; Niemantsverdriet, J.W.; Thüne, P. . *J.Catal.,* **2007,** *247,* 129.

55. Thushara, K.S.; Mathew, R.; Ajithkumar, T. G.; Rajamohanan, P. R.; Bhaduri, S.; and Gopinath, C. S.*J. Phys. Chem. C,* **2009,** *113,* 8556.

56. Lee, M. Y.; Scott, S. L.; *Chem. Eur. J.* **2011,** *17,* 4632.

57. Seenivasan, K.; Sommazzi, A.; Bonino, F.; Bordiga, S.; Groppo, E. *Chem. Eur. J.* **2011,** *17,* 8648.

58. (a) Magni, E.; Somorjai, G.A. *Surf. Sci.* **1996,** *345,* 1. (b) Kim, S. H.; Craig, R. T.; Somorjai, G. A. *Langmuir,* **2000, 16,** 9414

59. Mori, H.; Hasebe, K.; Terano, M. *Macromol. Chem. Phys.* **1998,** 199, 2709.

60. Kim, S. H.; Craig, R. T.; Somorjai, G. A. *Langmuir* **2000,** *16,* 9414

61. Boero, M.; Parrinello, M.; Terakura, K. *J. Am. Chem. Soc.* **1998,** *120,* 2746.

62. Puhakka, E.; Pakkanen, T. T.; Pakkanen, T. A. *J. Phys. Chem. A* **1997,** *101,* 6063.

63. Sozzani, P.; Bracco, S.; Comotti, A.; Simonutti, R.; Camurati, I. *J. Am. Chem. Soc.* **2003,** *125,* 12881.

Chapter 2

Experimental Section

2. Experimental Section

Development of new $MgCl_2.xLB$ supporting material for Z-N polymerization catalyst is essential in order to achieve better activity and tailored properties of polymers [1]. The Lewis base and controlling the stoichiometric ratio of the Lewis base to $MgCl_2$ and the synthesis method of the molecular adduct influences the activity and properties of the polyolefin obtained [2]. To prepare the active heterogeneous Z-N catalyst numerous amount of interest has been shown on $MgCl_2.xLB$ molecular adducts [3-6]. $MgCl_2.nTHF$ [7, 8], $MgCl_2.nEB$ [9-12] $MgCl_2.nEtOAc$ [10, 12] and $MgC1_2.2B$ [12] (THF = tetrahydrofuran; EB = ethyl benzoate; EtOAc = ethyl acetate; B = monoesters, alcohols and ketones) are some of the adducts have been used to prepare very active Z-N catalysts. For the synthesis of $MgCl_2.xLB$ molecular adduct, various physical and chemical syntheses have been used [13, 14]. However in the present work, azeotropic distillation method with toluene as a solvent has been used to prepare the well-defined single phase molecular adduct between $MgCl_2$ and alcohol or (Lewis base). Synthesized molecular adduct has been used as a supporting material for the titanated active Z-N catalyst preparation. Introduction and theory of various physical, structural and spectroscopic characterization techniques employed in the characterization of $MgCl_2.xLB$, its active Z-N catalyst and polymer analysis investigation have been described.

2.1 MgCl₂ supported Z-N catalyst synthesis

All manipulations involving air or moisture sensitive reactions were carried out by following the standard procedures under ultra-high pure N_2 atmosphere using standard Schlenk techniques. Partially hydrated (~5% H_2O) $MgCl_2$, titanium tetrachloride, methanol, ethanol, cyclohexanol, benzyl alcohol, 9-fluorenemethanol and dry stabilized THF (all from Sigma Aldrich), trimethylaluminium (TMA, 1.0 M solution in heptane), triethyl aluminium (TEA, 0.6 M solution in heptane), and triisobutylaluminium (TIBA, 1.1 M solution in

toluene) (all from Acros Organics) were used as received. Chlorobenzene (Sigma−Aldrich) was used after drying over anhydrous calcium hydride. n-Hexane and toluene (from Merck) were dried by refluxing with sodium prior to use. Ethylene (purity of 99.99%) obtained from a commercial plant and used without further purification for polymerization.

2.1.1 MgCl$_2$.xLB supporting material synthesis

We followed toluene azeotropic method to synthesize single phase molecular adduct having definite stoichiometry and structure. In order to understand molecular aspects of Z-N catalyst, we prepared well defined precursor and then went further to understand the complicated components of the Z-N system after titanation [15]. Toluene has been used as a solvent to form azeotropic mixture with the water present in the reaction mixture. Here in the synthesis of molecular adduct Dean-Stark apparatus has been used.

2.1.1.1 Preparation of MgCl$_2$.6CH$_3$OH

MgMeOH adduct was synthesized using a well-established azeotropic distillation method [9, 13]. Partially hydrated MgCl$_2$ (0.1 M) and 1.2 M dried methanol were added in the required quantity of toluene in a 200 mL round-bottom flask. The above reaction mixture was refluxed under stirring for 3 h at 105 °C. Subsequently, the solution was kept at 0 °C for 3 h for crystallization of the MgMeOH adduct. The white precipitate was washed with 800 mL of hexane, dried at room temperature under vacuum for 30 min, and stored in a vacuum desiccator [16].

2.1.1.2 Different stoichiometries of MgCl$_2$.xCH$_3$OH (MgMeOH)

For the synthesis of MgCl$_2$.xCH$_3$OH, three different temperatures (55 °C, 105 °C and 155 °C) have been chosen according to MgMeOH thermo gravimetric analysis profile. MgCl$_2$.6MeOH has been taken in 100 mL RB in inert atmosphere and heated in controlled N$_2$ gas flow for 1h at different temperature to prepare three different stoichiometries of

MgMeOH adduct, namely $MgCl_2.5.6CH_3OH$ (55 ^oC), $MgCl_2.2.9CH_3OH$ (105 ^oC) and $MgCl_2.1.3CH_3OH$ (155 ^oC).

2.1.1.3 Preparation of $MgCl_2.6C_2H_5OH$ (MgEtOH)

Partially hydrated $MgCl_2$ (0.1 M) and 1.2 M dried ethanol were added in the required quantity of toluene in a 200 mL round-bottom flask. The above reaction mixture was refluxed under stirring for 3 h at 110 °C. Subsequently, the solution was kept at 0 °C for 2 h for crystallization of the MgEtOH adduct. The white precipitate was washed with 500 mL of hexane, dried at room temperature under vacuum for 30 min, and stored in a vacuum desiccators [17, 18].

2.1.1.4 Preparation of $MgCl_2.6C_6H_{11}OH$ (MgCyOH)

Partially hydrated $MgCl_2$ (9.6 g, 0.1 M) and 104 mL (1 M) of cyclohexanol were taken in 500 mL of toluene in a 1 L round-bottom flask and refluxed under stirring conditions for 6 h at 135 °C. Subsequently, the solution was kept at 0 °C for 3 h for crystallization of MgCyOH. White precipitate obtained was washed with 800 mL of hexane, dried at RT in vacuum for 30 min, and stored in a vacuum desiccators [19].

2.1.1.5 Preparation of $MgCl_2.6PhCH_2OH$ (MgBzOH)

A standard procedure for the handling of air and moisture sensitive materials has been followed for the synthesis of the $MgCl_2.6PhCH_2OH$ adduct. The azeotropic distillation method has been followed to synthesize the MBA adduct as reported previously [16-19]. In a typical preparation method, in 500 mL RB flask equipped with a magnetic stirrer, 0.1 M partially hydrated $MgCl_2$ has been taken with 1.8 M benzyl alcohol. The above reaction mixture was refluxed at 140 ∘C under continuous azeotropic distillation of toluene water for 2 h. The resulting solution was cooled and maintained at 0 ∘C for crystallization. The transparent crystalline white solid adduct obtained was washed at least five times with dry n-hexane, dried and stored in a vacuum desiccator [20].

2.1.1.6 Preparation of MgCl$_2$.xEtOH.n9FM

Partially hydrated MgCl$_2$ (0.05 M) was added with 2g of 9FM and 2 ml of dried ethanol and toluene was taken in a 200 mL round-bottom flask. The above reaction mixture was refluxed under stirring for 3 h at 110 °C. Subsequently, the solution was kept at 0 °C for 2 h for crystallization of the MgEtOH adduct. The white precipitate was washed with 500 mL of hexane, dried at room temperature under vacuum for 30 min, and stored in a vacuum desiccators.

2.1.1.7 Preparation of MgCl$_2$.nTHF (n = 1.5, 2 and 4)

2.1.1.7.a Preparation of MgCl$_2$.nTHF (n = 1.5 and 2)

Partially hydrated MgCl$_2$ (1g) and dried THF (4mL) were added in the required quantity of toluene in a 100 mL round-bottom flask. The mixture was refluxed at 110°C for 3h. Finally RB was cooled for 2h and washed with hexane. The resulting white precipitate dried at room temperature under vacuum for 15 min and stored in a vacuum desiccators. Above procedure is followed with 15mL of THF to prepare MgCl$_2$.2THF.

2.1.1.7.b Preparation of MgCl$_2$.4THF

Partially hydrated MgCl$_2$ (1g) and dried THF (25mL) were added 100 mL round-bottom flask. The mixture has been stirred for 48 h. Finally product has been washed with hexane. The resulting white precipitate dried at room temperature under vacuum for 15 min and stored in a vacuum desiccators.

2.1.1.8 Preparation of MgCl$_2$.2THFA

Partially hydrated MgCl$_2$ (1g) and dried THFA (5mL) were added in the required quantity of toluene in a 100 mL round-bottom flask. The mixture was refluxed at 130 ^{o}C for 3 h. Finally RB was cooled for 2 h and washed with hexane. The resulting white precipitate dried at room temperature under vacuum for 15 min and stored in a vacuum desiccator.

2.1.2 Preparation of Active Z-N catalyst

2.1.2.1 Preparation of active catalyst over $MgCl_2.xROH$

Titanation of $MgCl_2.xROH$ adduct has been carried out by following the procedures given in the literature [14, 16-20], with following minor modifications. Twenty-eight grams of $MgCl_2.xROH$ adduct has been taken with 220 mL of chlorobenzene and stirred for 1 h at 110 °C. Subsequently, 220 mL of $TiCl_4$ was added over a period of 10 min and stirred further for 1 h. Resulting solid product was washed with two 100 mL portions of $TiCl_4$. Finally, the solid catalyst was filtered and washed several times with dry hexane at 60 °C until all the physisorbed Ti-species was removed. Then, $Ti-MgCl_2.nROH$ catalyst was dried under vacuum and stored in dry N_2 atmosphere.

2.1.2.2 Preparation of active catalyst over $MgCl_2.nLB$ (LB = THF, THFA)

Titanation has been carried out with different ratio of Mg/Ti ratio i.e., 1/2; 1/5; 1/10; 1/15. Required quantity of $TiCl_4$ has been added with the adduct in N_2 atmosphere with chlorobenzene as a solvent. The mixture was stirred for 48 h at room temperature. Finally solvent was dried completely and stored in vacuum desiccator.

2.2 Ethylene Polymerization

Ethylene polymerization was carried out in a Buchi Glas Uster glass polyclave reactor fitted with a thermocouple, an automatic temperature control unit and stirring speed of 500 rpm. In a typical polymerization, 0.5 L of dry hexane was added to the reactor at 75 °C, followed by alkyl aluminium (solution in n-heptane), and the catalyst was introduced into the reactor under dry N_2 stream and then evacuated. Ethylene (5 bar) was then fed at a constant pressure. Polymerization was carried out for 1 h at 75 °C. Atmospheric pressure reaction was carried out in a glass reactor by continuously passing ethylene gas for 1 h at 75 °C.

2. 3 Physico-chemical Characterization

2.3.1 Introduction

Physicochemical characterization techniques are important to understand any material including catalysts. X-ray diffraction, spectroscopy, microscopy, and methods based on adsorption and desorption are the routine material characterization techniques were employed. It gives information about structure, crystalline phase, crystallite size, optical properties, surface structure, textural properties, nature of active sites, morphology, particle size, acidity and other characteristic features. Further, these techniques will help to understand the structure-activity relationship to improve the activity of the catalyst for various applications. In this thesis, a number of analytical techniques have been used to characterize the molecular adducts, active catalysts and polymer obtained which include X-ray diffraction analysis (XRD), Thermo Gravimetric - Differential thermal analysis (TG-DTA), Infrared spectroscopy (IR), Raman spectroscopy, surface area and pore volume measurements, Nuclear Magnetic Resonance spectroscopy (NMR) scanning electron microscopy (SEM), optical microscopy and Gel permeation chromatography (GPC).

2.3.1.1 Instrument specifications and methods employed

XRD patterns were recorded on a Philips X'Pert Pro powder X-ray diffractometer using Cu K_α radiation (l = 1.5418 Å) with a flat sample stage in the Bragg–Brentano geometry. The diffractometer was equipped with a Ni filter and X'celerator as detector. The samples were scanned in the range $2\theta = 5–75^o$ and the scans were collected. All molecular adducts and titanated catalysts were protected with a thin layer of nujol or handled strictly under dry N_2 atmosphere to avoid any degradation due to interaction with atmospheric components. The structure analysis was attempted by the Rietveld refinement method using the X'Pert Plus software and the model structure was adopted from the structural data reported in the literature [17, 21]. Optical microscopic images of these adducts were recorded

on an Olympus make (BX50, Japan) optical microscope. Triblock copolymer and toluene were added to the adduct, and the resultant solution was sonicated for 10 min to obtain a uniform dispersion. A thin liquid layer from the above solution was employed for recording images, mainly to avoid particle agglomeration. The morphology of the catalyst was examined by environmental scanning electron microscopy (SEM). A high-resolution FEI QUANTA 200 3D SEM was used to measure the surface morphology [22]. The surface area of the catalysts was determined by the Brunauer–Emmett–Teller (BET) method via nitrogen adsorption on NOVA 1200 Quanta Chrome Equipment [23]. Thermal analyses of these adducts were recorded by Perkin–Elmer Diamond's thermogravimetry (TG) and differential thermal analysis (DTA) with alumina as the internal standard. Raman spectra were recorded on a Horiba JY Lab RAM HR 800 spectrometer excited with 633 nm lasers. While recording Raman measurements, to avoid any degradation of materials, a low temperature setup (Linkam-Examine-THMS 600 setup connected to a TP94 temperature programmer and LN94 unit to cool the stage below ambient temperature using liquid nitrogen) was employed [24]. The sample temperature was maintained below 0 ^{o}C to avoid any degradation from atmospheric moisture.

All of the solid state NMR measurements were carried out on a Bruker Avance 300 spectrometer operating at a static field of 7.04 T, resonating at 75.5 MHz for ^{13}C, using a 4 mm double resonance MAS probe [25]. Samples in the form of a fine powder were packed into a 4 mm O.D. zirconia rotor under nitrogen atmosphere and spun at 8 or 10 kHz. ^{13}C CPMAS measurements were performed using a standard Ramped- Amplitude Cross-Polarization (RAMPCP) pulse sequence [26] using a recycle delay of 50 to 120 s and a contact time of 2500 ms. Chemical shifts were referred (0 ppm) to the CH_2 carbon of adamantine (38.48 ppm) for ^{13}C. Single pulse MAS (HPDEC) spectra were acquired with a 45 degree flip angle and relaxation delays varying from 3 to 120 s.

Molecular weight distributions and polydispersities of polyethylene materials were determined using GPC (Waters 150-C ALC/GPC) at 135 ^{o}C in 1,2,4-trichlorobenzene as solvent. μ-Styragel columns were used and the peaks were calibrated with polystyrene. A 0.3–0.4% w/v solution was used at a flow rate of 1 mL min^{-1}

2.3.2 Theory and Experimental Procedures

The following part of second chapter gives a brief account of the theory and principle of selected characterization techniques used for the current study.

2.3.2.1 Raman Spectroscopy

Vibrational spectroscopy is an excellent method for identifying substances by providing unique fingerprint spectra. Raman spectroscopy is one of the fastest and non-destructive analytical techniques that give the vibrational spectrum and physical as well as chemical information of many materials. Among all vibrational techniques, Raman spectroscopy appears as unique method for the analysis in material science. In 1928, an Indian physicist Chandrashekhara Venkata Raman, known as C.V. Raman, discovered the phenomena of inelastic scattering of light, known as the Raman effect. This explains the shift in wavelength of a small fraction of radiation scattered by molecules, having different frequency from that of the incident beam [27]. This shift in wavelength depends upon the chemical structure of the molecules responsible for scattering. Raman spectroscopy utilizes scattered light to gain knowledge about molecular vibrations which can provide information regarding the structure, symmetry, electronic environment and bonding of the molecule, thus permits the quantitative and qualitative analysis of the individual compounds. The irradiation of a molecule with a monochromatic light always results in two types of light scattering, elastic and inelastic. In elastic scattering, no change in photon frequency occurs. Conversely, the inelastic scattering, which is accompanied by the shift in photon frequency due to excitation or deactivation of molecular vibrations in which either the photon may lose some

amount of energy or gains energy. Thus, three types of phenomena can occur. First, when the light is incident on a molecule, it can interact with the molecule but the net exchange of energy (i.e., in terms of wavelength λ_e) is zero, so the frequency of the scattered light is the same as that of the incident light ($\lambda_e = \lambda_s$). This process is known as Rayleigh scattering. Second, the light can interact with the molecule and the net exchange of energy is the energy of one molecular vibration. If the interaction causes the light photon to gain vibrational energy from the molecule then the frequency of the scattered light will be higher than that of the incident light ($\lambda_e = \lambda_s + \lambda_y$), known as anti-Stokes Raman scattering. Third, if the interaction causes the molecule to gain energy from the photon then the frequency of the scattered light will be lower than that of the incident light ($\lambda_e = \lambda_s - \lambda_y$), this process is known as Stokes Raman scattering. Raman spectra bring direct results of the analysis without sample preparation and easy interpretation of the results making it as a time saving and cost effective technique.
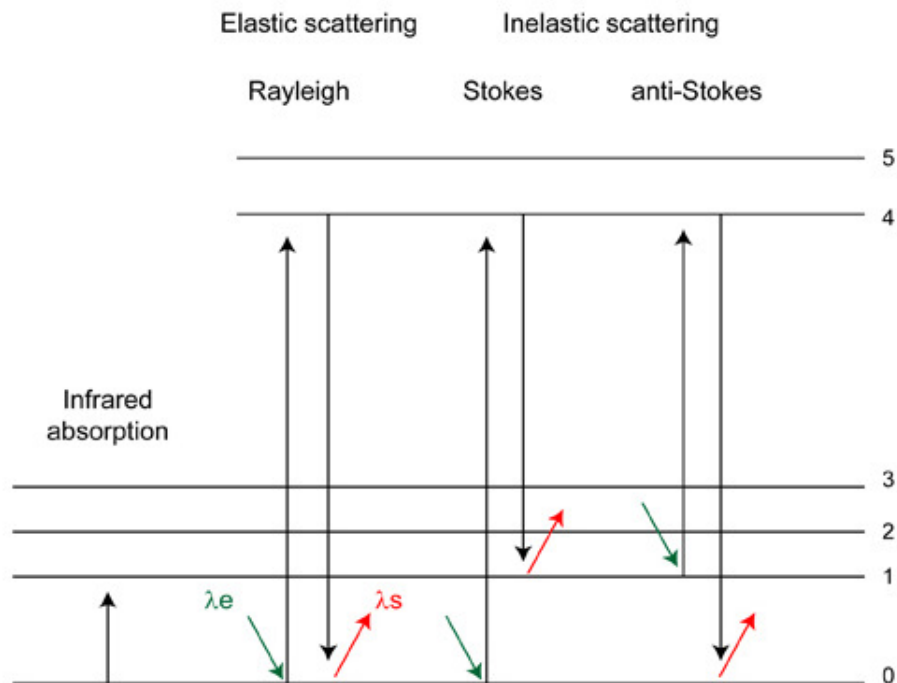
Figure 2.1: *Simplified energy level diagram. he shift in wavelength between the excitation light (λ_e) and the scattered light (λ_s) is related to Raman shift (ΔV in cm^{-1} ; $\Delta V = 1/ \lambda_y$) according to: $\Delta V = (1/ \lambda_e) + (1/ \lambda_s)$.*

2.3.2.2 Surface Area Determination by BET Method

Surface area is a significant powder property of nano-crystalline materials. The nano powders consisting of ultra fine crystals are typically characterized by a large surface-to-volume ratio. Thus, they exhibit large surface area owing to higher surface energy. The specific surface area of powder samples was measured through BET method [28] by using the BET equation,

$$P/V_{ads} (P_0-P) = 1/V_mC + [(C-1)/V_mC] \times (P/P_0)$$

where P = adsorption equilibrium pressure, P_0 = standard vapor pressure of the adsorbent, V_{ads} = volume at STP occupied by molecules adsorbed at pressure P, V_m = volume of adsorbate required for a monolayer coverage, and C = constant related to heat of adsorption. It is based on the determination of the amount of gas that is adsorbed on the surface of a powder in a monomolecular layer. To determine the surface area by the BET method, the amount of gas adsorbed in a monomolecular layer on the surface of a powder and the area occupied by a molecule of the adsorbed gas must be known. The latter value is 16.2×10^{-20} m^2 for a nitrogen molecule.

To differentiate the adsorption mechanism between micro-pore and to that in meso and macro-pores, the t-plot analysis was developed by Lippens and de Boer and the same was applied [29]. The method consists of plotting the adsorption isotherm in terms of the volume of the adsorbate versus the statistical film thickness, t. The pore size distribution is obtained from the analysis of the desorption isotherms by applying the Barret-Joyner-Hollenda (BJH) expand model [30] which involves the area of the pore walls and uses the Kelvin equation to correlate the partial pressure of nitrogen in equilibrium with the porous solid to the size of the pores where the capillary condensation takes place.

2.3.2.3 Optical Microscope

A microscope is in principle nothing else than a simple lens system for magnifying small objects. The first lens, called the objective, has a short focal length (a few mm), and creates an image of the object in the intermediate image plane. This image in turn can be looked at with another lens, the eye-piece, which can provide further magnification. Morphology of the samples prepared was studied by OLYMPUS polarized optical microscope (POM). The sample is dispersed in a mixture of tri-block copolymer and toluene, the resultant solution was sonicated for few minutes to get dispersion of samples. A drop of the solution is placed on a glass slide and the slides were then transferred to the sample stage and the photomicrographs of the sample were recorded using Olympus digital camera.

2.3.8 Solid state NMR Spectroscopy

NMR spectroscopy is a research technique that exploits the magnetic properties of certain atomic nuclei to determine physical and chemical properties of atoms or the molecules in which they are present. It relies on the phenomenon of nuclear magnetic resonance and can provide detailed information about the structure, dynamics, reaction state, and chemical environment of molecules. The principle behind NMR is that many nuclei have spin and all nuclei are electrically charged. If an external magnetic field is applied, an energy transfer is possible between the base energy to a higher energy level (generally a single energy gap). The energy transfer takes place at a wavelength that corresponds to radio frequencies and when the spin returns to its base level, energy is emitted at the same frequency. The signal that matches this transfer is measured in many ways and processed in order to yield an NMR spectrum for the nucleus concerned. In general, NMR is a physical phenomenon in which magnetic nuclei in a magnetic field absorb and re-emit electromagnetic radiation. In quantum mechanical terms, the nuclear magnetic moment of a nucleus can align with an externally applied magnetic field of strength B_o in only $2I+1$ ($I =$ spin quantum

number) ways, either with or against the applied field B_o. For a single nucleus with I=1/2 and positive g, only one transition is possible (D I=1, a single quantum transition) between the two energy levels The energetically preferred orientation has the magnetic moment aligned parallel with the applied field (spin m=+1/2) and is often given the notation a, whereas the higher energy anti-parallel orientation (spin m=-1/2) is referred to as b. The rotational axis of the spinning nucleus cannot be orientated exactly parallel (or anti-parallel) with the direction of the applied field Bo (defined in our coordinate system as about the z axis) but must process (motion similar to a gyroscope) about this field at an angle, with an angular velocity given by the expression This energy is at a specific resonance frequency which depends on the strength of the magnetic field and the magnetic properties of the isotope of the atoms.
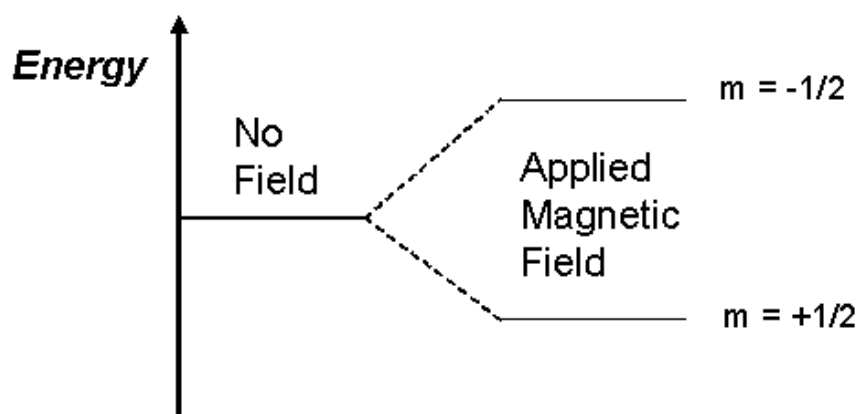
Figure 2.2: *Energy levels for a nucleus with spin quantum number ½.*

Solid-state NMR spectroscopy is a powerful tool for the investigation of crystalline and amorphous solids. It can provide a lot of information about local structure around selected atoms/nuclei and is extensively employed in the studies of new inorganic, organic and hybrid materials, and also of solids of biological interest. Literature survey shows only few reports are available that solid-state NMR spectroscopy is being used extensively to elucidate the structure of the $MgCl_2$ based molecular adduct as a support material for Ziegler-Natta polymerization. [31] Solid–state NMR investigations of $MgCl_2$ supported Ziegler-Natta catalyst rely on spectroscopy of ^{13}C nuclei. Though this NMR-active isotope of carbon is

quite rare (natural abundance of 1.1%), ^{1}H-^{13}C cross-polarization (CP) magic-angle spinning (MAS) technique has years ago developed into a routine technique with which well resolved and intense ^{13}C spectra can be acquired in a matter of hours. Resolution of signals within ^{13}C NMR spectra of well crystalline materials is sometimes almost comparable to resolution of signals within the spectra of solutions.^{1}H NMR spectroscopy, which is very much exploited in solution NMR, is not yet as widespread in solid-state NMR. The reason is in the very strong proton-proton homonuclear dipolar interactions which lead to inhomogeneous broadening of NMR signals. Because of that, solid- state ^{1}H NMR spectra are often featureless compositions of many overlapped absorption lines, from which not much structural information is accessible.
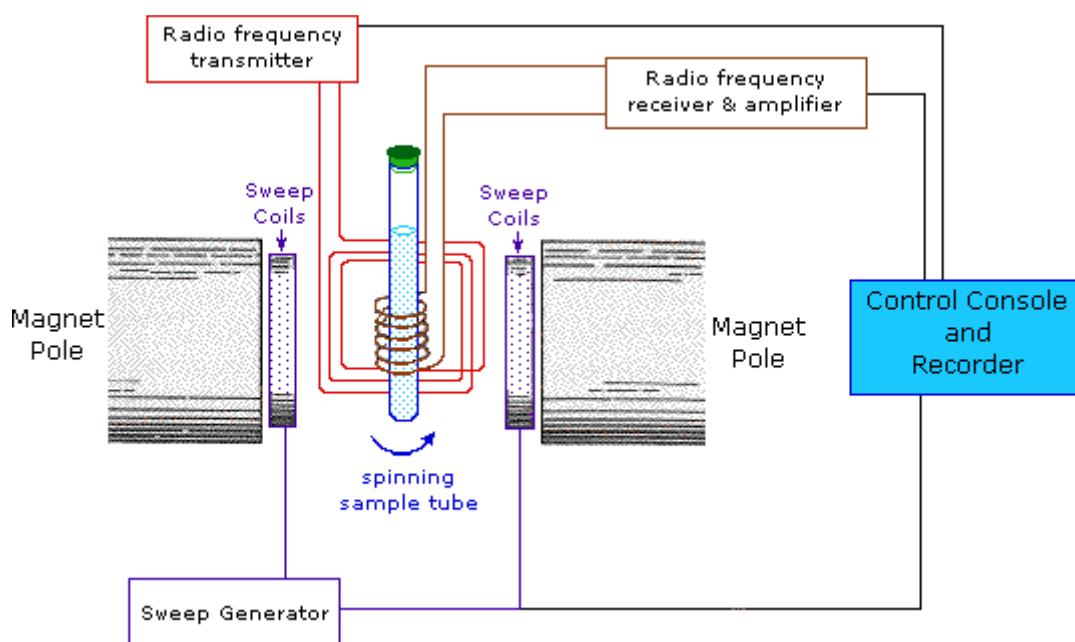
Figure 2.3: *Schematic diagram of NMR spectroscopy.*

Solid state NMR experiments were carried out on a Bruker Avance 300 spectrometer operating at a static field of 7.04 T, resonating at 300 MHz for 1H and 75.5 MHz for ^{13}C, equipped with 4 mm double resonance MAS probes. The operating frequencies for ^{1}H and ^{13}C were 300 and 75.4 MHz, respectively. The samples were packed into a 4mm zirconia rotor and loaded into a Bruker's 4 mm MAS probe and spun about the magic angle (54.74^o) at

8/10 kHz. The 90° pulses for proton and carbon were 2.6 (~96 kHz) and 3.0 (~83 kHz), respectively. The 1H radio frequency (rf) field strength for heteronuclear two pulse phase modulation (TPPM) decoupling was carried out at 100 kHz. All single-pulse excitation (SPE) experiments were done using a 30°flip angle and with a recycle delay of 5/20 s, and cross-polarization (CP) experiments were performed using a recycle delay of 3 s and a contact time of 2.5 ms using a standard ramp-CP pulse sequence with the RF power 83 kHz. All the chemical shifts were referenced to TMS by using adamantine as an external standard. Typically, 128-2048 scans were collected depending on the sensitivity of the sample.

Magic-angle spinning (MAS)

Magic-angle spinning is used routinely in the vast majority of solid-state NMR experiments, where its primary task is to remove the effects of chemical shift anisotropy and to assist in the removal of heteronuclear dipolar coupling effects. It is also used to narrow lines from quadrupole nuclei and is increasingly the method of choice for removing the effects of homonuclear dipolar coupling from NMR spectra. This latter application requires very high spinning rates however, and so is not yet routine in all laboratories.
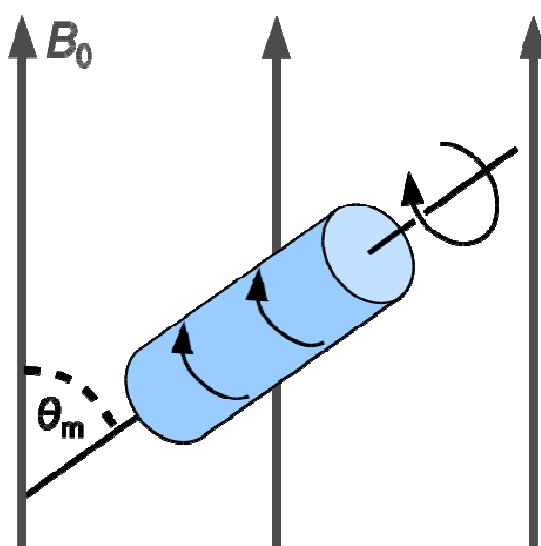
Figure 2.4: *Magic-angle spinning: The sample (blue) is rotating with high frequency inside the main magnetic field (B_0). The axis of rotation is tilted by the magic angle θ_m with respect to the direction of B_0.*

In nuclear magnetic resonance, magic angle spinning (MAS) is a technique often used to perform experiments in solid-state NMR spectroscopy [32-33]. By spinning the sample (usually at a frequency of 1 to 70 kHz) at the magic angle θ_m (ca. 54.74°, where $\cos 2\theta_m = 1/3$) with respect to the direction of the magnetic field, the normally broad lines become narrower, increasing the resolution for better identification and analysis of the spectrum.

In any condensed phase, a nuclear spin experiences a great number of interactions. The main three interactions (dipolar, chemical shift anisotropy, quadrupolar) often lead to very broad and featureless lines. However, these three interactions in solids are time-dependent and can be averaged by MAS. The nuclear dipole-dipole interaction, between magnetic moments of nuclei averages to zero only at the magic angle, θ_m . The chemical shift anisotropy, a nuclear-electron interaction, averages to a non-zero value. The quadrupolar interaction is only partially averaged by MAS leaving a residual secondary quadrupolar interaction. In liquids, e.g. a solution of an organic compound, most of these interactions will average out because of the rapid time-averaged molecular motion that occurs. This orientation averaging in solution is mimicked by MAS of a solid. This causes the signal to become much narrower, giving rise to the isotropic value (which is of interest for structural determination of solid materials and compounds) and spinning sidebands which occur at multiples of the spinning speed and can be used to determine the chemical shift anisotropy of the nuclei.

The physical spinning of the sample is achieved via an air turbine mechanism. These turbines (or rotors) come in a variety of diameters (outside diameter), from 1.3-15.0 mm, and are usually spun on air or nitrogen gas. The rotors are made from a number of different materials such as ceramics e.g. zirconia, silicon nitride or polymers such as poly(methyl methacrylate) (PMMA), polyoxymethylene (POM). The cylindrical rotors are axially symmetric about the axis of rotation. Samples are packed into the rotors and these are then

sealed with a single or double end cap. These caps are made from number of different materials e.g. Kel-F, Vespel, zirconia or boron nitride depending on the application required.

High - Power Proton Decoupling

High-power decoupling is the simplest technique which removes the effects of heteronuclear coupling. Consider the case of dipolar-coupled ^{1}H and ^{13}C spins, where the ^{13}C spins are to be observed. The method consists of applying continuous irradiation of very high power (100-1000 watts) at the frequency of the proton resonance. The required pulse sequence for the ^{13}C nuclei is then applied and the ^{13}C FID measured while continuing the ^{1}H radiation. It is worth noting that the pulses used for decoupling ^{1}H in samples with abundant ^{1}H spins do not need to be particularly broad banded, i.e. they do not need to cover a wide frequency range. Because of the homonuclear dipolar coupling between the ^{1}H nuclei in such samples, the effects of a rf pulse applied to any part of the ^{1}H spectrum are transmitted among all coupled ^{1}H. This is because the rf radiation applied to the ^{1}H spin affects the z-component of spin of each ^{1}H nucleus which is close to resonance with the irradiation [34].

2.3.2.4 Gel Permeation Chromatography

Gel permeation chromatography (GPC) is a type of size exclusion chromatography (SEC) in which particles is separated based on their size, or in more technical terms, their hydrodynamic volume [35]. The technique is more often used for the polymer analysis. In this technique organic solvent is used as the mobile phase and beads of porous polymeric material as stationary phase. Polydispersity index (PDI) as well the molecular weight are the important properties to consider the when characterizing polymers. Polymers can be characterized by a variety of definitions for molecular weight including the number average molecular weight (M_n), the weight average molecular weight (M_w), the size average molecular weight (M_z), or the viscosity molecular weight (M_v). GPC allows for the

determination of PDI as well as M_v and based on other data, the M_n, M_w, and M_z can be determined.

The principle of GPC is, different sizes of polymer particles will elute (filter) through at different rates. Column consists of a hollow tube tightly packed with extremely small porous polymer beads designed to have pores of different sizes. Pores may be depressions on the surface or channels through the bead. Smaller particles enter into the pores, larger particles don't. So larger analytes spend little time in the pores and are eluted quickly. There is a limited range of molecular weights that can be separated by each column. Therefore the size of the pores for the packing should be chosen according to the range of molecular weight of analytes to be separated. For polymer separations the pore sizes should be of the order of the polymers being analyzed. If a sample has a broad molecular weight range it may be necessary to use several GPC columns in continuous manner with one another to fully resolve the sample.

In GPC, the concentration by weight of polymer in the eluting solvent is monitored continuously with a detector. Currently there are many detector types available. They can be divided into two main categories. The first is concentration sensitive detectors which includes UV absorption, differential refractometer (DRI) or refractive index (RI) detectors, infrared (IR) absorption and density detectors. Molecular weight sensitive detectors include low angle light scattering detectors (LALLS), multi angle light scattering (MALLS) [36]. The resulting chromatogram is therefore a weight distribution of the polymer as a function of retention volume. The most sensitive detector is the differential UV photometer and the most common detector is the differential refractometer (DRI). When characterizing copolymer, it is necessary to have two detectors in series [37]. For accurate determinations of copolymer composition at least two of those detectors should be concentration detectors [36]. The

determination of most copolymer compositions is done using UV and RI detectors, although other combinations can be used [38].

1.11 Reference

1. Albizzati, E.; Galimberti, M. *Catal. Today* **1998,** *41,* 159.

2. Sozzani, P.; Bracco, S.; Comotti, A.; Simonutti, R.; Camurati, I. *J. Am. Chem. Soc.* **2003,** *125,* 12881.

3. Luciani, L.; Kashiwa, N.; Barbe, P. C.; Toyota, A. (to Montedison S.p.A. and Mitsui Petrochemical Ind., Ltd), Ger. Offenl. 2643 143, 2 June 1977; *Chem. Abs.* **1978,** *87,* 68893v.

4. Giannini, U.; Albizzati, E.; Parodi, S. (to Montedison), US Pat. 4277589, 7 July **1981**.

5. Sivaram, S.; Srinivasan, P. R. "In Advanced Polyolefins", Proceedings of the ACS International Symposium, **1985,** edited by R. B. Raymond and T. Cheng (Plenum, New York, 1987) p. 283.

6. Giannini, U., G. Giunchi, E. Albizzati and P. C. Barbe, *NATO ASI Ser. C* **1987,** *215* 473.

7. Handlir, K.; Holecek, J.; Benes, L. *Coll. Czech. Chem. Comm.* **1985,** *50* 2422.

8. Handlir, K.; Holecek, J.; Klikorka, J.; Bocek, V. *Chem. Prum.* **1986**, *36,* 72.

9. S. A. Sergeev, G. D. Bukatov, V. A. Zakharov and E. M. Moroz, *Makromol. Chem.* **1983,** *184,* 2421.

10. Handlir, K.; Holecek, J.; Vecorek, P.; Ved. P.S., Vys. S. *Chemickotechnol. Pardubice* **1987**, *50a,* 43.

11. Abis, L.; Albizzati, E.; Giannini, U.; Giunchi, G.; Santoro, E.; Noristi, L. *Makrornol. Chem.* **1988,** *189,* 1595.

12. Noto, V. D.; Bresadola, S.; Zannetti, R.; Viviani, M. *Z. Kristallogr.* **1993**, *204,* 263.

13. Bart, J. C. J. *J. Mater. Sci.* **1995,** *30,* 2809.

14. Bhaduri, S.; Gupta, V. K.U.S. Patent 6,841,633, 2005, and references therein.

15. Seenivasan, K.; Sommazzi, A.; Bonino, F.; Bordiga, S.; Groppo, E. *Chem. Eur. J.* **2011,** *17,* 8648

16. Gnanakumar, E. S.; Gowda, R. R.; Kunjir, S. ; Ajithkumar, T. G.; Rajamohanan, P. R.; Chakraborty, D.; Gopinath, C. S. *ACS Catal.* **2013,** *3*, 303.

17. Thushara, K. S.; Gnanakumar, E. S.; Mathew, R.; Jha, R. K.; Ajithkumar, T. G.; Rajamohanan, P. R.; Sarma, K.; Padmanabhan, S.; Bhaduri, S.; Gopinath, C. S. *J. Phys. Chem. C* **2011,** *115,* 1952.

18. K. S. Thushara, R. Mathew, T. G. Ajithkumar, P. R. Rajamohanan, S. Bhaduri, C.S. Gopinath, *J. Phys. Chem. C* **2009,** *113,* 8556.

19. Gnanakumar, E. S.; Thushara, K. S.; Gowda, R. R.; Raman, S. K.; Ajithkumar, T. G.; Rajamohanan, P. R.; Chakraborty, D.; Gopinath, C. S. *J. Phys. Chem. C.* **2012,** *116,* 24115.

20. Gnanakumar, E. S.; Thushara, K. S.; Bhange, D. S.; Mathew, R.; Ajithkumar, T. G.; Rajamohanan, P. R.; Bhaduri, S.; Gopinath, C. S. *Dalton Trans.* **2011,** *40,* 10936.

21. (a) Mapa, M.; Thushara, K. S.; Saha, B.; Chakraborty, P.; Janet, C. M.; Viswanath, R. B.; Nair, C. M.; Murty, K. V. G. K.; Gopinath, C. S. *Chem. Mater.* **2009,** *21,* 2973. (b) Vijayaraj, M.; Gopinath, C. S. *J. Catal.* **2006,** *241*, 83.

22. (a) Sivaranjani, K.; Agarkar, S.; Ogale, S. B.; Gopinath, C. S. *J. Phys. Chem. C* **2012,** *116,* 2581. (b) Sivaranjani, K.; Verma, A.; Gopinath, C. S. *Green Chem.* **2012,** *14,* 461.

23. (a) Sivaranjani, K.; Gopinath, C. S. *J. Mater. Chem.* **2011,** *21,* 2639. (b) Reddy, A. S.; Gopinath, C. S.; Chilukuri, S. *J. Catal.* **2006,** *243,* 278.

24. (a) Maity, N.; Rajamohanan, P. R.; Ganapathy, S.; Gopinath, C. S.; Bhaduri, S.; Lahiri, G. K. *J. Phys. Chem. C* **2008,** *112,* 9428. (b) Naik, B.; Parida, K. M.; Gopinath, C. S. *J. Phys. Chem. C* **2010,** *114,* 19473. (c) Mapa, M.; Gopinath, C. S. *Chem. Mater.* **2009,** *21,* 351.

25. Metz, G.; Wu, X.; Smith, O. S. *J. Magn. Reson., Ser. A* **1994,** *110,* 219.

26. (a) Sreeja, V.; Smitha, T. S.; Nand, D.; Ajit Kumar, T. G.; Joy, P. A. *J. Phys. Chem. C* **2008,** *112,* 14737. (b) Mathew, T.; Sivaranjani, K.; Gnanakumar, E. S.; Yamada, Y.; Kobayashi, T.; Gopinath, C. S. *J. Mater. Chem.* **2012,** *22,* 13484.

27. Raman, C.V.; Krishnan, R.S. *Nature* **1928,** *121,* 501.

28. Atkins, P.W. Physical Chemistry, Oxford University Press, London,**1990.**

29. Lippens, B. C.; de Boer, J. H. *J. Catal.***1965,** *4,* 319.

30. Barret, E. P.; Joyner, L. G.; Halenda, P. H. *J. Amer. Chem. Soc.***1951,** *73,* 373

31. Sozzani, P.; Bracco, S.; Comotti, A.; Simonutti, R.; Camurati, I. *J. Am. Chem. Soc.* **2003,** *125,* 12881.

32. Hennel, J. W.; Klinowski, J. "Magic Angle Spinning: A Historical Perspective". In Klinowski,, J. New techniques in solid-state NMR. Springer. **2005,** pp-1.

33. Andrew, E.R. "Magic Angle Spinning". In Anne McDermott. Solid State NMR Studies of Biopolymers. John Wiley & Sons. **2010,** pp-83.

34. Duer, M. J. "Introduction to Solid-state NMR spectroscopy". Blackwell Publishing Ltd. **2004,** pp -77.

35. Skoog, D.A. Principles of Instrumental Analysis, 6th ed.; Thompson Brooks/Cole: Belmont, CA, **2006,** Chapter 28.

36. Trathnigg, B. *Prog. Polym. Sci.* **1995,** *20,* 615.

37. Sandler, S.R.; Karo, W.; Bonesteel, J.; Pearce, E.M. Polymer Synthesis and Characterization: A Laboratory Manual; Academic Press: San Diego, **1998.**

38. Pasch, H. *Adv. Polym. Sci.* **2000,** *150,* 1.

Chapter 3

MgCl$_2$.xCH$_3$OH Adduct and Its Influence on Polymerization Activity

3.1 Introduction

Invention of the TiCl$_4$-derived polymerization catalyst by Ziegler and Natta in the 1950s, led the growth of polyolefin industries. In the ever steadily increasing polyolefin market, demand for polyethylene and polypropylene are satisfied by the polymerization reaction using the heterogeneous Z−N catalyst [1−3]. The components of the above Z−N catalyst generally consist of TiCl$_4$ as an active part, alkyl aluminium (R$_3$Al) as a cocatalyst, and MgCl$_2$ as a support. Apart from these three components, to increase the activity and stereospecificity of the catalyst, Lewis bases or electron donors (ED) such as alcohols, esters, and ethers have been added. The advantages of MgCl$_2$-supported Z−N catalysts are their extremely high activity and high isotactic index in stereo specific polymerization reactions [3]. Another benefit from a polymer product point of view is that, by controlling the porosity and morphology of the catalyst particle, properties of the polymers can be tuned [4−10].

Due to vast industrial impact of the Z−N catalyst, theoretical [11−15] and experimental [21−26] efforts have been made to understand the active sites. Despite a significant amount of research, many aspects are yet to be properly understood about the Z−N catalyst: importantly, (a) the precise structure of the active sites on the specific surface of MgCl$_2$, (b) the exact role of electron donors on the activation of the MgCl$_2$ surface, (c) the nature of the electron donor and stoichiometry around MgCl$_2$ and its influence in the activity, and (d) the role of aluminium alkyl co-catalysts. Although the advantages of MgCl$_2$-supported catalysts are massive compared with other types of polymerization catalysts, the complexities present in the system requires scientific understanding and thereby appropriate improvement in the catalyst design and development [11, 22−24]. Much less scientific rational was behind the advanced version of the supported Z−N catalyst because of the poor molecular level understanding aspects. From an industrial point of view, a definite correlation between the structural and electronic structure of the catalyst support to the catalytic activity

would primarily help the huge production of polyolefin business worldwide. Therefore, it is a great challenge to surface science, spectroscopy, and computational methods to elucidate the molecular aspects of the Mg-containing catalyst support to obtain better understanding of Z−N catalyst systems [13, 19−26].

The method of preparing the support, especially the nature of the molecular adduct and the alcohol employed, drastically influence the catalytic activity through porosity [27−31]. Indeed, a *"super active"* catalyst support, prepared from $MgCl_2$ and ethanol [24] or isopropyl alcohol [29], has been reported in the literature. A Z−N catalyst support has been prepared by treating $MgCl_2$ with an alcohol. Although the preparation method is simple, a profound understanding of the control of alcohol molecules in the supporting material, $MgCl_2 \cdot xROH$, is decisive, since the productivity and isotacticity of the Z−N catalyst depends on the $ROH/MgCl_2$ ratio [32, 33]. Today, ethanol has been used routinely as an activator for many industrial heterogeneous Z−N catalyst systems. In general, super active catalyst synthesis involves removal of alcohols from the molecular adduct and simultaneous introduction of $TiCl_4$ into the $MgCl_2$ lattice to produce a porous nanostructure of the Z−N system, which influences the catalytic activity and the properties of the polymer [32−34]. It is well understood that the nature of the alcohol in the $MgCl_2 \cdot xROH$ predominantly decides the catalytic activity and, thus, the properties of the polymers; however, very few reports are available on the influence of different alcohols on the activity [29−31, 35, 36].

Until now, theoretical research work has been focused on the interaction of $TiCl_4$ with the specific cut surfaces of α-$MgCl_2$. Consequently the structure of the $MgCl_2 \cdot xROH$ support has a good influence on the insertion of $TiCl_4$ on the proper facet of $MgCl_2$ [37−39]. It has been speculated that $MgCl_2 \cdot xROH$ with different alcohols exposes different crystal planes of $MgCl_2$ and hence, the variation in activity. In addition, the porous character of the $TiCl_4/MgCl_2$ catalyst is also important for its catalytic activity. Thus, a fair amount of

knowledge about the structural aspects of $MgCl_2 \cdot xROH$ precursor is required. To date, there have been only a few single crystal structures MgEtOH and MgBzOH that have been made available in the literature among the molecular adducts, mainly because of the difficulties in preparing single crystals [40, 41]. Powder XRD and solid state NMR methods also provide significant structural details of these adducts. A detailed solid state NMR study of the ethanol adduct revealed the presence of mixed phases of $MgCl_2 \cdot xEtOH$ ($1 \leq x \geq 3$) [24]. Crystal structures of $MgCl_2 \cdot xEtOH$ (x = 1.5, 2.8, and 3.3) have been resolved using an *ab initio* method from the data derived from high resolution XRD [42]. Many such efforts are required for better understanding of the structural aspects of molecular adducts.

In this chapter, we describe the synthesis of a single phase molecular adduct of $MgCl_2 \cdot 6CH_3OH$ (MgMeOH) as the supporting material. The simplest Lewis base with one carbon namely, methanol has been chosen to reduce the complexities during the characterization of the adduct as well as the final active catalyst. To the best of our knowledge, no detailed studies of $MgCl_2 \cdot 6CH_3OH$ are available in the literature [43]. For a deeper understanding of multi component complex systems of this type, which interact with each other, it is vital to identify the physicochemical properties of the individual components and to allow the complexities to increase systematically [44]. An active catalyst (Ti-MgMeOH) has been prepared, characterized and evaluated for polymerization activity. Both MgMeOH adduct and Ti-MgMeOH, the active catalyst, have been subjected to various structural, spectroscopic, and morphological characterizations to understand the system thoroughly. The Ti-MgMeOH catalyst shows much better activity compared with many other commercial catalysts based on Ti-MgEtOH Z–N catalysts. Further to understand the influence of the stoichiometry of the $MgCl_2$ precursor on the activity of the catalyst, single phase MgMeOH have been subjected to dealcoholation at different temperature to prepare methanol adduct with different stoichiometric ratios. Similarly, structural and spectroscopic

techniques have been used to understand the MgCl$_2$ precursor. Each precursor have been used to prepare the corresponding active catalyst and screened for ethylene polymerization. Structure-activity correlations have been made to understand the complex active system in better manner.

3.2 Results and Discussion

3.2.1 Characterization of MgMeOH adduct

3.2.1.1 Powder X-ray diffraction
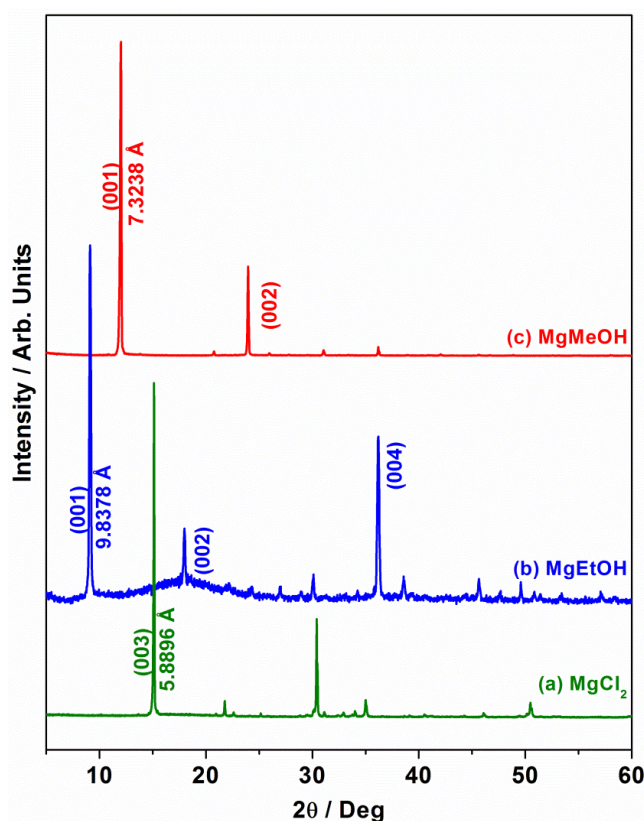
Figure 3.1: *Powder X-ray diffraction pattern of (a) anhydrous MgCl$_2$, (b) MgEtOH, and (c) the MgMeOH adduct.*

Figure 3.1 shows the powder XRD of anhydrous MgCl$_2$, MgEtOH and MeMeOH adducts. The diffraction pattern of MgCl$_2$ corresponds to a rhombohedral crystal structure with cubic close packing that shows strong diffraction features at 2θ value of 15.1° (003) and 35° (004). The XRD pattern of MgMeOH adduct gives a high-intensity peak at a 2θ of 11.9°

(001) (d = 7.3238 Å) and 23.8° (002). Similarly, the XRD pattern of the MgEtOH adduct shows a strong diffraction pattern of the (001) plane at 2θ of 9° (d = 9.8378 Å) and further diffractions at 18° (002) and 36° (004) characteristics for rhombohedral structure [24, 27, 45]. The selective high intensity of the (001), (002), and (004) planes are evident for the preferentially oriented (00l) growth of MgMeOH and MgEtOH adduct crystallites in the present azeotropic distillation preparation method. High-intensity (00l) planes characterize the growth of crystallites along the z-axis of the layered structure of $MgCl_2$ to form octahedral coordinated molecular adducts [27]. The smaller d value of the MgMeOH adduct compared with the MgEtOH adduct is directly correlated to the smaller size of methanol compared with ethanol.

3.2.1.2 Thermal analysis

Figure 3.2 shows the thermogravimetry and differential thermal analysis of MgMeOH adduct. Temperature of the sample was ramped from ambient to 300 °C at 5 °C/min under flow of nitrogen (99.999%) at 40 mL/min. Well-defined sharp DTA peaks and the associated weight loss indicate the systematic sequential dissociation of methanol molecules from the MgMeOH adduct [27, 29, 31]. The dissociation of the first methanol molecule occurs at 82 °C (which is above the boiling point of methanol, 65 °C) shows the interaction of methanol with $MgCl_2$ is strong. However, it is also to be noted that weight loss begins from 35 °C. Further, sharp weight loss occurs at 111, 130, 147, 176, and 235 °C because of the loss of second to sixth methanol molecules, respectively, in a stepwise manner. Weight loss >100 °C clearly indicates the methanol molecules bound strongly with $MgCl_2$. In addition, in DTA analysis, six different peaks/transitions are also observed, indicating the successive dealcoholation. Sharp and well-defined DTA peaks underscore the intra-molecular interaction between the methanol molecules and $MgCl_2$. On the basis of the molecular formula $MgCl_2 \cdot 6CH_3OH$, the calculated weight loss is in excellent agreement with that of

experimental weight loss observed (68%), within an error margin of ±1%. From the above

calculation also, the ratio of MeOH/MgCl$_2$ has been derived to be six.
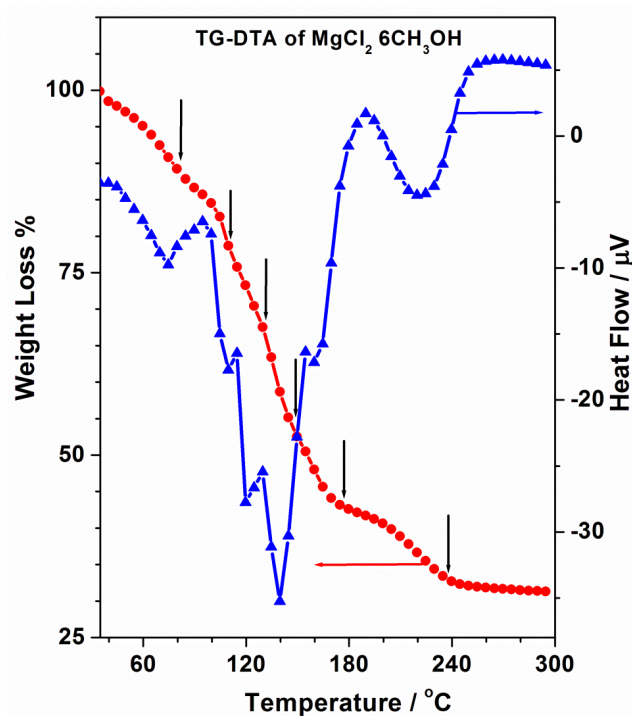
Figure 3.2: *Thermal analysis of the MgMeOH adduct. Temperature was ramped from ambient to 300 °C at 5 °C/min under a flow of ultrapure N$_2$ at 40 mL/min.*

3.2.1.3 Raman Analysis

Raman spectra of anhydrous MgCl$_2$, MgMeOH adduct, and liquid methanol are

shown in Figure 3.3 MgCl$_2$ has a rhombohedral structure with a D$_{3d}$ space group and has a

layered structure. The Mg^{2+} ion is coordinated to six chloride ions in the distorted octahedral

geometry [46, 47]. MgCl$_2$ shows a high, intense peak at 243 cm^{-1}, which has been assigned to

the A$_{1g}$ breathing mode of MgO$_6$ octahedra in the lattice. No other peaks were observed for

MgCl$_2$. Liquid methanol shows a strong peak for C–O stretching at 1033 cm^{-1}, a medium

intense peak for the –CH$_3$ bending mode at 1445 cm^{-1}, a –C–H symmetric stretching peak at

2832 cm^{-1}, and a –C–H anti-symmetric peak at 2941 cm^{-1} [48]. The adduct, MgMeOH,

shows an extra peak at 708 cm^{-1}, in addition to the features observed for neat methanol. This

specific Raman mode indicates the formation of a Mg–O bond between MgCl$_2$ and the

alcoholic oxygen to form a MgO$_6$ octahedron [35, 36, 47]. There is a significant shift in the

above Raman feature compared with MgEtOH (684 cm^{-1}), and it is attributed to the change in electronic and structural features of MgMeOH and MgEtOH. Above points suggests that MeOH interacts more strongly with MgCl$_2$ than with EtOH.
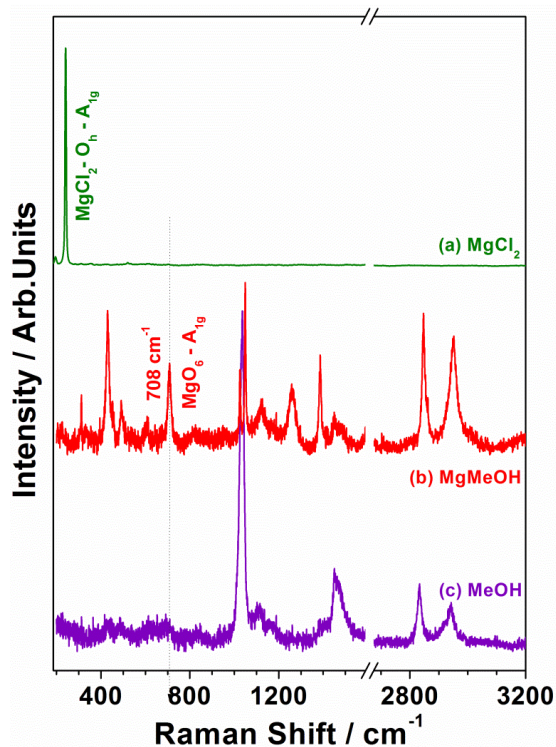
Figure 3.3: *Raman spectra of (a) MgCl$_2$, (b) MgMeOH, and (c) MeOH.*

3.2.1.4 Solid State NMR

The ^{1}H MAS spectrum of MgMeOH (Figure 3.4a) shows both broad and narrow features. Two narrow peaks are observed at 4.2 and 6.3 ppm for the MgMeOH adduct, indicating the presence of protons from −CH$_3$ and −OH, respectively. The ^{13}C CPMAS spectrum (Figure 3.4b) of the MgMeOH adduct shows a single peak at 50.2 ppm. The absence of splitting in the ^{13}C peak clearly shows the presence of only one type of carbon in MgMeOH. From the ^{13}C CPMAS spectrum, we could conclude that the MgMeOH has been prepared in a single phase. ^{13}C single pulse excitation MAS spectrum of MgMeOH also exhibited only one environment at 50.2 ppm.
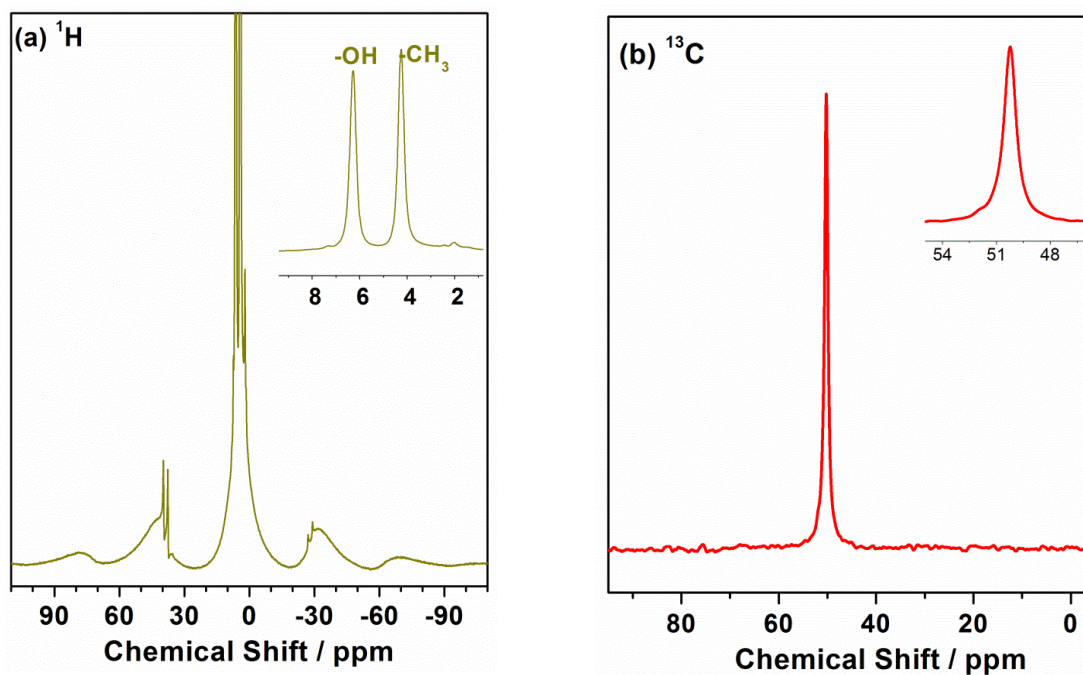
Figure 3.4: *(a) ^{1}H MAS and (b) ^{13}C CPMAS NMR spectrum of MgMeOH.*

3.2.1.5 Scanning Electron Microscope
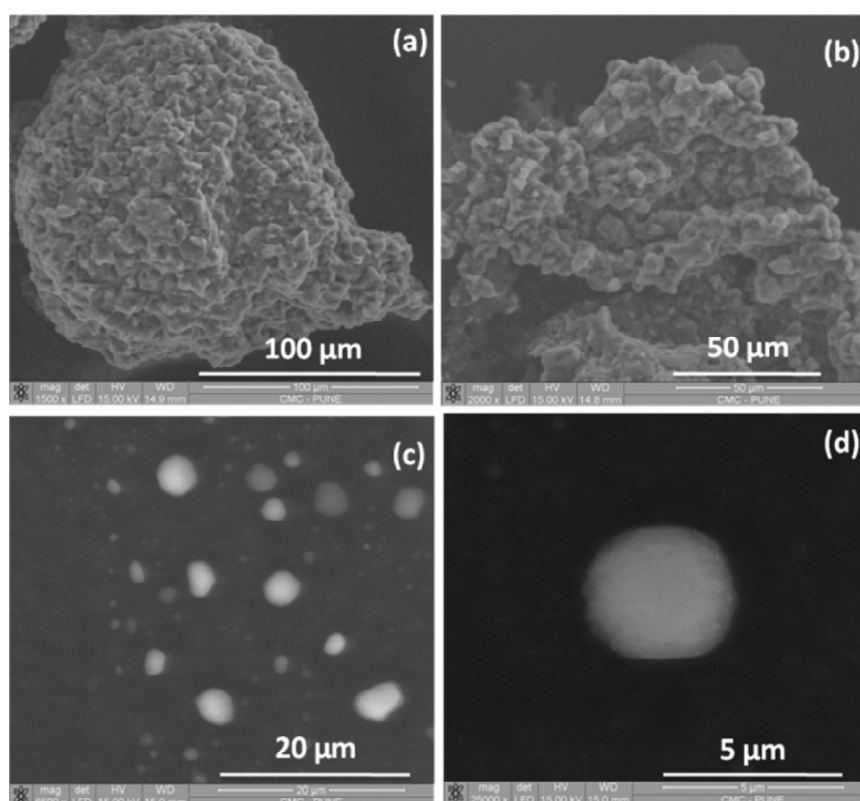
Figure 3.5: *SEM image of the MgMeOH adduct. All the images were recorded at 15 KV. Magnification factors for a−d are 1500, 2000, 6500, and 25000, respectively.*

SEM images of the MgMeOH adduct are shown in Figure 3.5 The images in Figure 3.5a and b were recorded after dispersing the MgMeOH adduct in anhydrous hexane [30]. It is evident that agglomerated particles with large distribution sizes are present in the MgMeOH adduct. The images in Figure 5c and d were recorded by dispersing the adduct in toluene−triblock copolymer solution to avoid agglomeration [30, 31]. The SEM images clearly show particles with an average size of ~5 μm. Close observation of the SEM image of the MgMeOH particles indicates that the surface is not uniformly spherical.

3.2.2 Characterization of titanated adduct

3.2.2.1 Powder X-ray diffraction

Powder XRD of Ti−MgMeOH active catalyst is shown along with anhydrous $MgCl_2$ and MgMeOH adduct in Figure 3.6. After $TiCl_4$ treatment, the characteristic peaks for the MgMeOH adduct completely disappear and broad diffraction features appear around 15°, 29−33°, and 50°. Because of the removal of methanol molecules from MgMeOH, a drastic change occurs from the highly oriented crystalline nature of the MgMeOH adduct into the $TiCl_x$ incorporated nano-crystalline $MgCl_2$ catalyst [10,30,31,49]. The broad, low-intensity peak around 15° is due to the stacking of −Cl−Mg−Cl− triple layers along the (003) crystallographic directions. This also signifies that the triple layer structure is severely ruptured, mainly to incorporate $TiCl_x$ in the $MgCl_2$ unit. The particle size of MgMeOH, measured from the SEM results shown in Figure 6 is ~5 μm; however, the crystallite size, calculated by the Scherrer equation from the XRD results in Figure 6, is 14 nm for Ti−MgMeOH. The above size reduction is attributed to the change in long range order on the MgMeOH adduct to short-range order after titanation. Stacking faults in the triple layers could be identified further by a halo, broad peak between 29° and 33° and a peak around 50°. A similar kind of XRD is reported for titanated catalyst in the literature, clearly indicating the highly disordered δ-$MgCl_2$ crystallographic form [49,50].
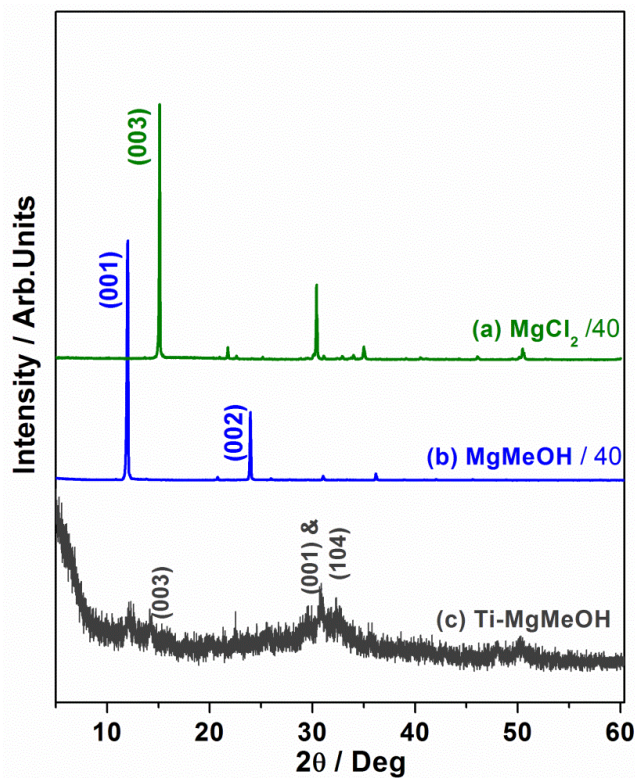
Figure 3.6: *Powder XRD of (a) MgCl₂, (b) the MgMeOH adduct, and (c) the Ti−MgMeOH active catalyst.*

3.2.2.2 Solid State NMR
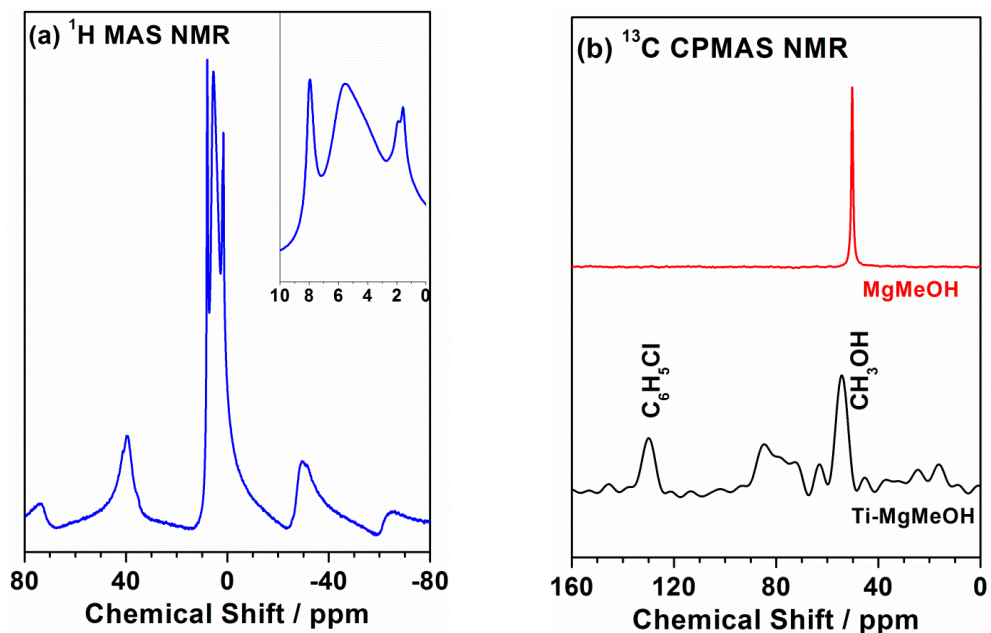
Figure 3.7: *(a) ^1H and (b) ^{13}C CPMAS NMR spectra of the Ti−MgMeOH active catalyst.*

The solid state NMR spectrum of the active catalyst is shown in Figure 3.7. ^{1}H MAS NMR (Figure 3.7a) shows a peak around 8 ppm in active catalyst confirms the presence of physisorbed chlorobenzene, which has been used in the preparation of the active catalyst for washing away any extra $TiCl_4$. A broad peak is observed between 6 and 4 ppm that is attributed to methanol and other small organic molecules trapped in the pores of the Ti−MgMeOH during the active catalyst synthesis. The broadness of the peak is due to the highly restricted motion of the molecules in the pores of the active catalyst. Another peak around 1.7 ppm is due to the trapped hydrocarbon present in the pores of the active catalyst.

The ^{13}C CPMAS NMR of the titanated catalyst is shown in Figure 3.7b. The peak observed at 130 ppm confirms the presence of chlorobenzene. Apart from this peak, a few more peaks are observed at 84, 54, and 20−15 ppm. During the preparation of Z−N catalysts, $TiCl_4$ interacts with MgMeOH, and there are chances for formation of HCl and CH_3OH and many cascade reactions involving either or both HCl and CH_3OH. This lead to formation of small molecules such as ethers, chlorinated methanol/ether, etc. trapped in pores. The peaks observed in the region 90−70 ppm are attributed to oxygenated species such as $CH_3−O−CH_3$, $Cl−CH_2OH$, or $Cl−CH_2−O−CH_3$ molecules formed during the above synthesis of Ti-MgMeOH. A peak at 54 and 20−15 ppm indicates free methanol molecules and hexane molecules adsorbed inside the pores of the active catalyst, respectively.

3.2.2.3 Thermal Analysis

TG and DTA analyses of the Ti−MgMeOH catalyst are shown in Figure 3.8. Significant differences have been observed in the TG and DTA of MgMeOH adduct and the active catalyst, Ti−MgMeOH. First, the total weight loss obtained in Ti−MgMeOH was 38%, compared with 68% in the case of MgMeOH. This net weight loss difference could be due to the removal of most of the methanol during the active catalyst preparation. As discussed in solid state NMR analysis of active catalyst, trapped organic molecules, such as

chlorobenzene, hexane, ethers, and chlorinated CH₃OH molecules in the pores, seem to desorbed during the ramping in TG−DTA and lead to weight loss.
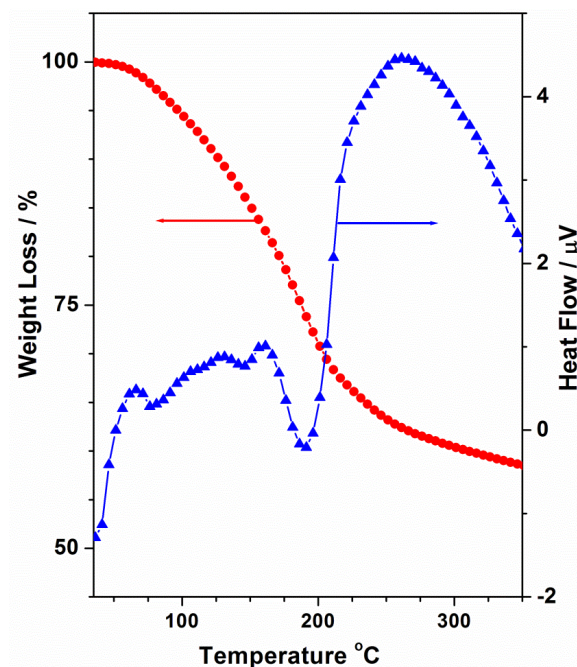
Figure 3.8: *Thermal analysis of the Ti−MgMeOH active catalyst. The temperature was ramped from ambient to 300 °C at 5 °C/min under a flow of ultrapure N₂ at 40 mL/min.*

3.2.2.4 Scanning Electron Microscope
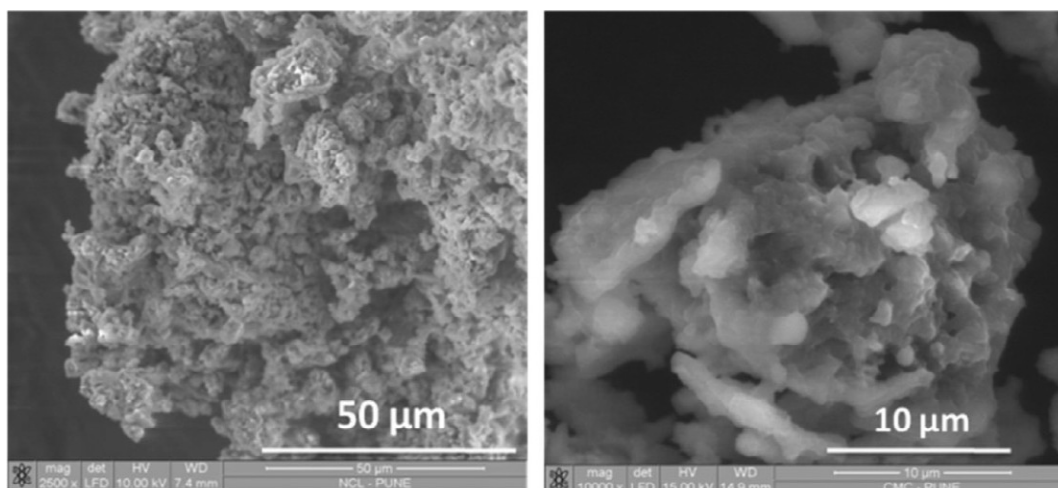
Figure 3.9: *SEM image of Ti-MgMeOH active catalyst. Images were recorded at 10 (left) and 15 KV (right), respectively. Magnification factors for a and b are 2500 and 10000, respectively.*

Figure 3.9 shows the SEM images of the Ti−MgMeOH active catalyst. The images were recorded after the sonication of dispersed Ti−MgMeOH catalyst in triblock copolymer and toluene solution to avoid any agglomeration [35] and to resist the atmospheric degradation due to the air-sensitive nature of the catalyst. The SEM image clearly shows the highly porous nature of the catalyst.

3.2.2.5 N_2 adsorption isotherm analysis
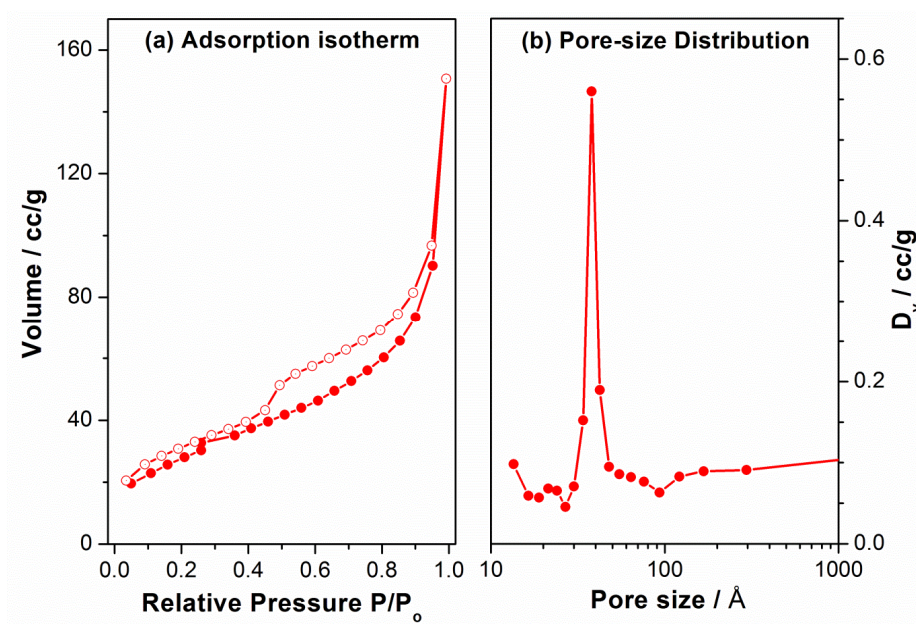
Figure 3.10: (a) *Adsorption isotherm and (b) pore size distribution of the Ti−MgMeOH catalyst.*

The BET method was used to measure the surface area of the Ti−MgMeOH active catalyst from N_2 adsorption−desorption isotherm analysis; the results are shown in Figure 3.10. The surface area of the active catalyst was 102 m^2/g which is higher than many commercial Ti-MgEtOH catalysts (32 m^2/g). The average pore diameter of Ti−MgMeOH was calculated, from the desorption branch of the adsorption isotherm, to be 41 Å, with a pore volume of 0.233 cm^3 g^{-1}. However, the average pore diameter calculated from the adsorption branch is 2.4 nm, with a pore volume of 0.223 cm^3 g^{-1}. The above difference is due to the sudden desorption in the isotherm around $P/P_0 = 0.45$ (Figure 10a) [51]. Careful analysis of the adsorption isotherm indicates a type-IV (H3) isotherm [52] for the Ti-MgMeOH catalyst.

Table 3.1: *Ethylene polymerization results of using Ti-MgMeOH catalyst.*

S.No	Support	Ti wt% (mmol)	Co-catalyst	Condition	PE Yield (g/g of catalyst)	PE Yield (g/mmol of Ti)	Mn (Mw) gmol^{-1}	MWD
1	MgMeOH	13 (0.19)	Me$_3$Al	75°C, 1atm	3247	1208.80	10490 (140569)	13.4
2	MgMeOH	13 (0.19)	Et$_3$Al	75°C, 1atm	1863	693.56	12746 (150410)	11.8
3	MgMeOH	13 (0.19)	iBu$_3$Al	75°C, 1atm	1230	457.9	13985 (135660)	9.7
4	MgMeOH	13 (0.19)	Me$_3$Al	75°C, 5atm	7245	3188.65	26723 (275339)	10.3
5	MgMeOH	13 (0.19)	Et$_3$Al	75°C, 5atm	4588	1707.83	28113 (254141)	9.04
6	MgMeOH	13 (0.19)	iBu$_3$Al	75°C, 5atm	3199	1190.93	17334 (154273)	8.9
7	MgEtOH[29]	11 (0.23)	Et$_3$Al	75°C, 5atm	1300	572	22173 (255010)	11.5
8	MgBzOH[30]	24 (0.51)	Et$_3$Al	75°C, 5atm	960	183	26111 (188000)	7.2
9	MgCyOH[36]	9 (0.19)	iBu$_3$Al	75°C, 5atm	3570	1918	45801 (297710)	6.5

Catalyst quantity = 0.1g; Al/Ti = 200, 50, 10 and 50 for MgMeOH, MgEtOH, MgBzOH and MgCyOH respectively.

It clearly shows the presence of predominant micropores along with mesopores in the Ti−MgMeOH catalytic system.

3.2.2.6 Ethylene Polymerization for MgMeOH

Ethylene polymerization reactions were carried out using the Ti−MgMeOH catalyst, and cocatalysts with three different alkyl chains, namely, methyl, ethyl, and isobutyl (R_3Al; R = CH_3, $-CH_2CH_3$, and $-CH_2CH(CH_3)_2$). For each cocatalyst, reactions were carried out at two different pressures and at 75 °C. Polymerization results are shown in Table 3.1. Average results were taken after carrying out three sets of polymerizations for each condition. (1) As expected, higher activity of the catalyst was observed for the reaction carried out at a higher ethylene pressure (5 atm) compared with the 1 atm reaction. (2) Among the reactions with different catalysts, entry **4** shows the best ethylene polymerization activity of Ti−MgMeOH catalyst, when Me_3Al was used as a cocatalyst at 5 atm. This activity is much higher compared with a commercial Ziegler−Natta catalyst (~6 times). (3) Indeed, at ambient pressure, polymerization at 75 °C with Ti−MgMeOH is greater than commercial catalyst activity at 5 atm pressure. Ti−MgMeOH activity is much higher than reported for the active catalyst derived from cyclohexanol.[36] (4) The higher activity of the Ti-MgMeOH− Me_3Al combination compared with the other cocatalyst combination could be due to narrow pores, which help the cocatalyst to interact with $TiCl_x$ species present inside the pores of the active catalyst. (5) The PE yield from Ti−MgMeOH catalyst is higher with Me_3Al; however, the MWD of PE is significantly higher with other co-catalysts. This could be due to the labile nature or higher reactivity of Me_3Al compared with other co-catalysts.

It is also to be emphasized that in addition to the porosity of the final catalyst, many other parameters seem to influence the catalytic activity and, hence, polyolefin yield. For example, Z−N catalyst derived from cyclohexanol adduct, entry **9,** shows a significantly higher porosity (BET surface area 236 m^2/g and 11.8 nm pore diameter [36] than that of

methanol adduct-derived Z–N catalyst. Indeed, the above observation highlights the necessity of porosity for better activity; however, this alone is not sufficient. Furthermore, a different porosity likely leads to different crystallographic planes and, hence, interaction between $TiCl_x$ and $MgCl_2$, which in turn influences the mode of interaction with the co-catalysts. [53] Another likely possibility is the over reduction of catalytically active Ti species; because of higher porosity, the cocatalyst can interact with the Ti species and reduces it to the undesirable Ti^{2+}. This type of electronic interaction would lead to a decrease in activity, despite the high surface area. In fact, a thorough study could lead to tuneable properties of the Z–N catalyst system for olefin oligomerization to polymerization.

3.2.3 Different stoichiometries of $MgCl_2.xCH_3OH$

As synthesized MgMeOH adduct has been dealcoholated under constant N_2 flow with heating under different temperatures for 1h ($55^{o}C$, $105^{o}C$, $155^{o}C$), the corresponding adducts have been named as MgMeOH-55, MgMeOH-105 and MgMeOH-155, respectively. Titanated active catalysts have been prepared from corresponding molecular adducts and named as Ti-MgMeOH-RT, Ti-MgMeOH-55, Ti-MgMeOH-105 and Ti-MgMeOH-155.

3.2.3.1 Powder X-ray diffraction

Figure 3.11 shows the powder XRD of anhydrous $MgCl_2.xCH_3OH$ adducts. XRD pattern of $MgCl_2.6CH_3OH$ adduct gives a high intensity peak at 2θ value of 11.9^{o} (001) (d=7.3238 Å) for the preferential oriented (00l) growth of MgMeOH crystallites in present azeotropic distillation preparation method [55]. When MgMeOH-RT adduct dealcoholated at different temperature such as 55 ^{o}C, 105 ^{o}C and 155 ^{o}C, the characteristic peak at 11.9^{o} (001) for single phase methanol adduct i.e., MgMeOH-RT ($MgCl_2.6CH_3OH$) has started to split and shifted toward low 2θ value as shown in the above figure. Splitting of the peak might be due to stoichiometries other than $MgCl_2.6CH_3OH$ is present in the system. MgMeOH-155 shows high intense peak around 11.5^{o}. Comparatively low intensity of MgMeOH-155 could be due

to high dealcoholation of methanol from $MgCl_2$ centre, obviously leads to less crystalline adduct.
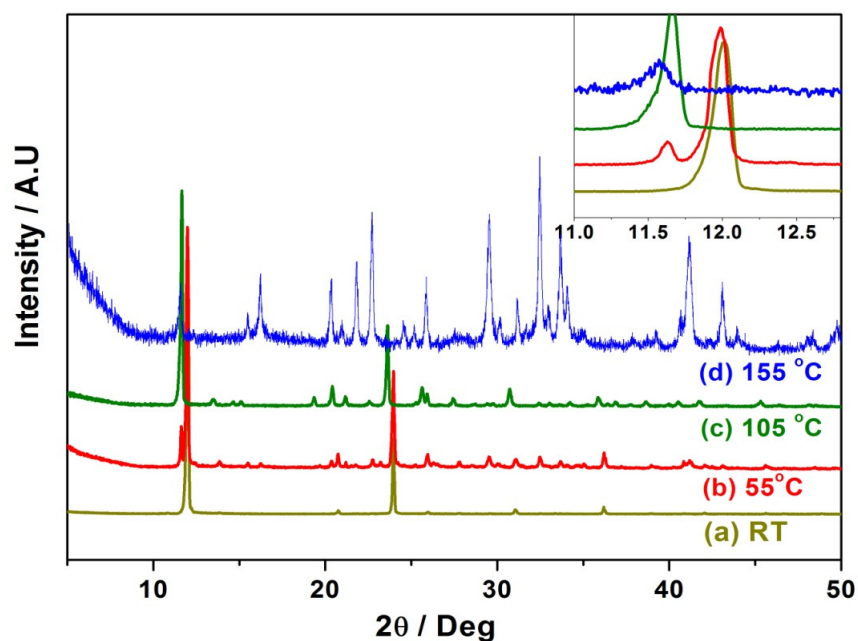
Figure 3.11: *Powder X-ray diffraction pattern of different stoichiometries of molecular adduct $MgCl_2.xCH_3OH$ synthesized at different temperature.*

3.2.3.2 Solid state NMR

Figure 3.12 shows the ^1H MAS NMR and ^{13}C CPMAS spectra of the MgMeOH adduct recorded at room temperature and after heating at different temperatures for 1 h under N_2 flow. As the heating temperature increases, the number of peaks observed in the ^{13}C CPMAS spectrum also increases as a result of loss of symmetry and also shows a downfield shift. The profile and the chemical shift of MgMeOH are significantly affected by heating at different temperatures because of the removal of methanol from the MgMeOH adduct. The complexity of the spectrum has increased due to the non-equivalence of CH_3OH molecules present around Mg^{2+} after the heating. As the temperature increases, the $MeOH/MgCl_2$ ratio starts to decrease as a result of the increasing extent of dealcoholation at higher temperature. Temperatures chosen were based on the observations made from TG−DTA data.

A closer look at these ^{13}C CPMAS data, without any background correction provides more insight to the nature of methanol molecules in the adduct after heating. On heating at 55

°C, the major signal found (~70%) still corresponds to the hexa adduct at 50.25 ppm. In addition, two additional weak signals of nearly equal intensity also appear at 51.01 and 51.90, indicting the presence of mixed phases. The intensity of the signals corresponding to the latter environment increased while the signal corresponding to the hexa adduct completely vanished on heating at 105 °C. At this stage, a new weak signal (10%) at 53.15 ppm also emerged, which became stronger at 155 °C. Yet another additional signal (~30%) was also noticed at this temperature. It is very evident from the observed multiplicities and intensities of the ^{13}C signals that the system exists as mixed phases and their populations vary with the thermal history. It is to be noted that downfield peaks are observed for lower coordination of
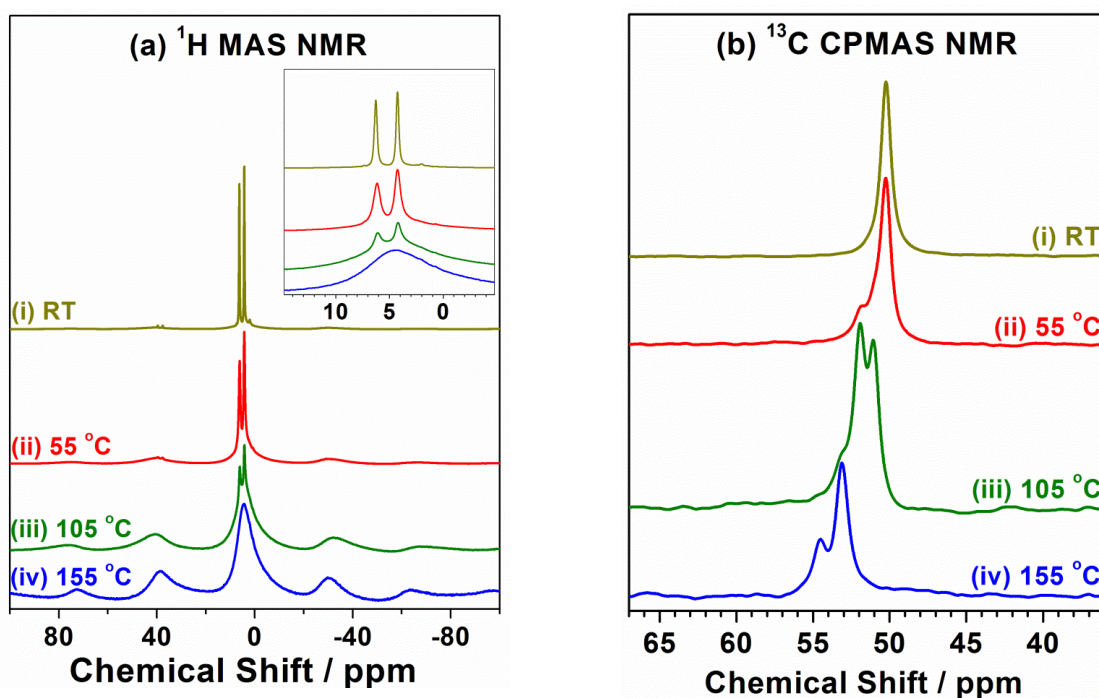
Figure 3.12: *(a) ^{1}H MAS and (b) ^{13}C CPMAS NMR spectra recorded at RT, after heat treatment of MgMeOH at different temperatures given on the traces.*

methanol around Mg^{2+} due to a stronger degree of association. Similar observations were also noticed for the MgEtOH [24]. The TG−DTA results indicated that the number of CH_3OH coordinating around Mg^{2+} decreases gradually to ~2 after heating at 155 °C, and hence, a

substantial change in structure and electronic structure is expected [54]. A detailed investigation is required for proper understanding of the various phases of adducts present during the process of dealcoholation.

The effects of loss of methanol from the adduct are further corroborated to the ^{1}H MAS NMR spectra (Figure 3.4a) collected after different extents of heating. The sharper features observed for the hexa-methanolate (MgMeOH) adduct broadens on an increase in the temperature after heating and becomes very broad in the sample heat-treated at 155 °C. Alcohol molecules that are relatively more mobile in $MgCl_2 \cdot 6CH_3OH$ will have a stronger association with the matrix in $MgCl_2 \cdot xCH_3OH$ when x tends to be less than 6. This increase in the strength of association is reflected as an increase in the ^{1}H line width, and for the sample heated at 155 °C, the molecular motions of methanol molecules in the adduct are arrested to a greater extent and, hence, exhibit very broad ^{1}H signal (tens of kilohertz), similar to the one associated with rigid molecules.

The compositions of various heat-treated MgMeOH adducts were measured by dissolving a known amounts of adduct in THF [24,30,31]. $MeOH/MgCl_2$ stoichiometry decreases from 6 for the parent adduct to 5.6, 2.9, and 1.3 after heat treatment at 55, 105, and 155 °C, respectively. It is to be noted that at a stoichiometry of 5.6, NMR results demonstrate the presence of two other phases along with the parent adduct and demonstrate a high sensitivity toward finding different compositions. A similar linear variation in the stoichiometry has been observed in TG−DTA results (Figure 3.2). The above stoichiometry measured changes are in good agreement with that of the results obtained in Figure 3.12, suggesting interaction between $MgCl_2$ and MeOH increases when the stoichiometry decreases. Similar findings were reported for $MgCl_2 \cdot 6EtOH$ adduct by Sozzani et al, [24] and it is worth exploring with detailed NMR measurements.

Schematic representation of the octahedral coordination of the Mg^{2+} sites with a number of methanol molecules (ligands). The sites are labelled as **A_n** (where $1 < n < 6$) depending on the number of ligands, a single isomer is represented even if more than one structural isomer is possible. From the XRD and solid state NMR studies, the above stoichiometries are present in the dealcoholated adducts at higher temperature. The point to be noted is, at particlar temperature dealcoholation it is highly possible to present as mixture of all of above stoichiometries. Quantitative NMR results giving only the average number of methanol ligands per Mg^{2+} sites.
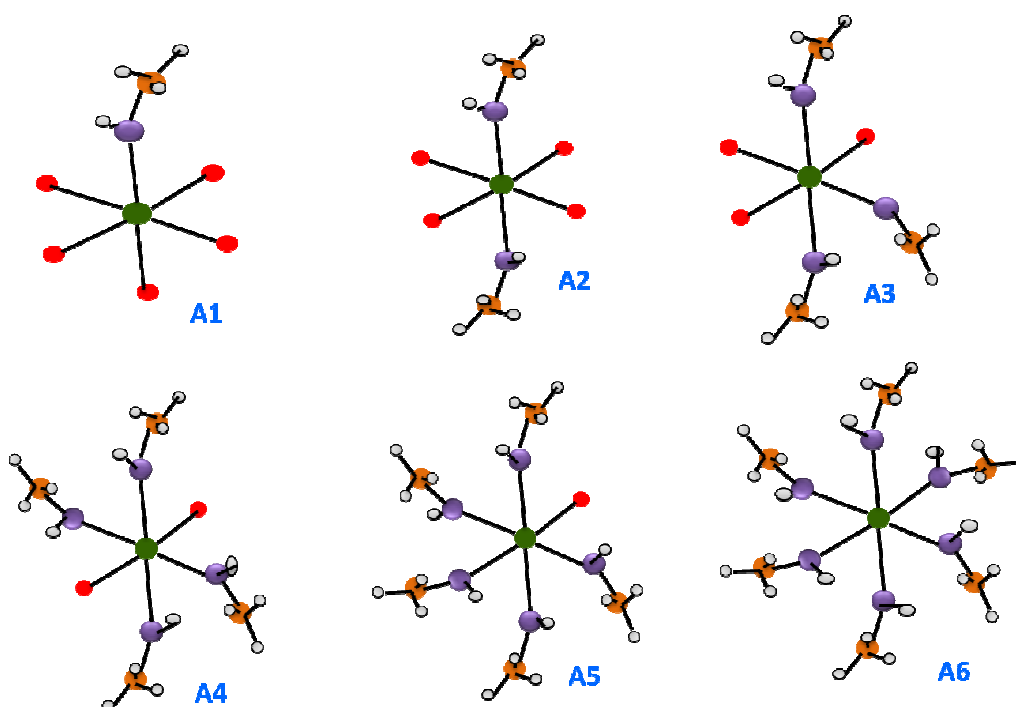
Figure 3.13: *Models for the different stoichiometries of MgCl₂.xCH₃OH molecular adduct.*

Table 3.2: *NMR Quantitative results for different ratios of molecular adduct.*

S. No	Adduct	Temperature (°C)	Stoichiometry (x)	Adduct composition
1	MgCl₂.xCH₃OH	RT	6	MgCl₂.6CH₃OH
2	MgCl₂.xCH₃OH-55	55	5.6	MgCl₂.5.6CH₃OH
3	MgCl₂.xCH₃OH-105	105	2.9	MgCl₂.2.9CH₃OH
4	MgCl₂.xCH₃OH-155	155	1.3	MgCl₂.1.3CH₃OH

3.2.3.3 ^{13}C CPMAS Solid state NMR of active catalyst

Solid state ^{13}C CP MAS spectra of all titanated catalyst have been shown in Figure 3.14. A peak at 128 ppm is due to the presence of chlorobenzene (Chlorobenzene has been used as a solvent for the active catalyst preparation) present in the pores of active catalyst. All the active catalysts show the peak for free methanol at 55 ppm. However, among all the active catalyst synthesized, MgMeOH-RT shows relatively higher amount of methanol from the comparison of the intensity of the peak. It could be related with the amount of methanol stoichiometry around Mg^{2+} centre. In MgMeOH-155, stoichiometry around Mg^{2+} is 1.33 and
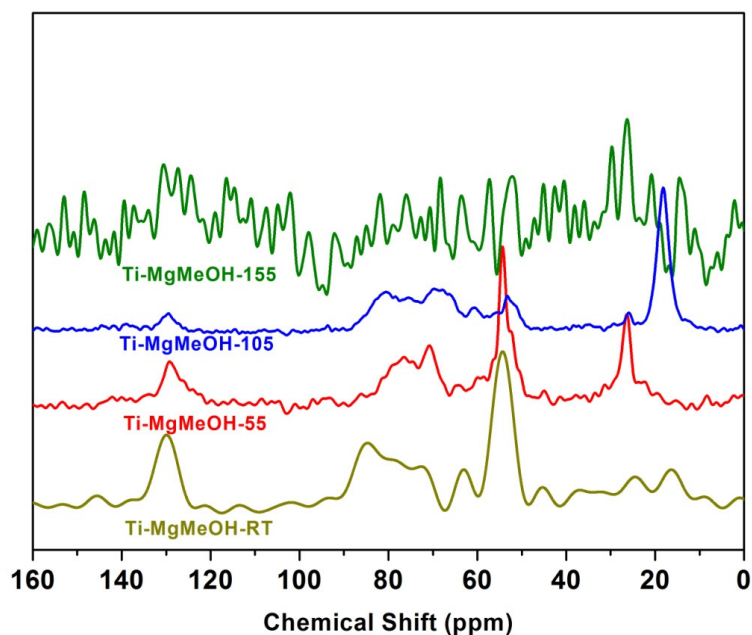
Figure 3.14: *^{13}C CP-MAS spectra of titanated catalyst synthesized from different stoichiometries of MgCl$_2$.xCH$_3$OH.*

obviously during the synthesis of active catalyst most of the alcohol molecules will be removed with the simultaneous titanation over MgCl$_2$ support. Hence MgMeOH-155 is the adduct containing least amount of free methanol molecules in the present system. Other than these two peaks, a few more peaks are observed at 84, 54, 30 and 20−15 ppm. As mentioned early there are chances for the formation of HCl and CH$_3$OH and many cascade reactions involving either or both HCl and CH$_3$OH. Peak at 20−15 ppm indicates the presence of

hexane molecules adsorbed inside pores of active catalyst. Peaks observed in the region 90−70 ppm are recognized to oxygenated species such as CH_3−O−CH_3, Cl−CH_2OH, or Cl−CH_2−O−CH_3 molecules formed during the above synthesis of active catalyst. Nonetheless, overall intensity of the peaks decrease as molecular adducts stoichiometry around Mg^{2+} is decreasing.

3.2.3.4 N_2 adsorption and desorption isotherm of active catalysts

N_2 adsorption and desorption analysis of all active catalysts is shown in Figure 3.15. All the titanated catalysts exhibit type-IV isotherm with H3 hysteresis and hence mesoporosity. This indicates all the titanated catalysts are having major contribution from mesopores. Pore size distribution suggests narrow pores (mesoporous) are present in all the titanated catalyst.
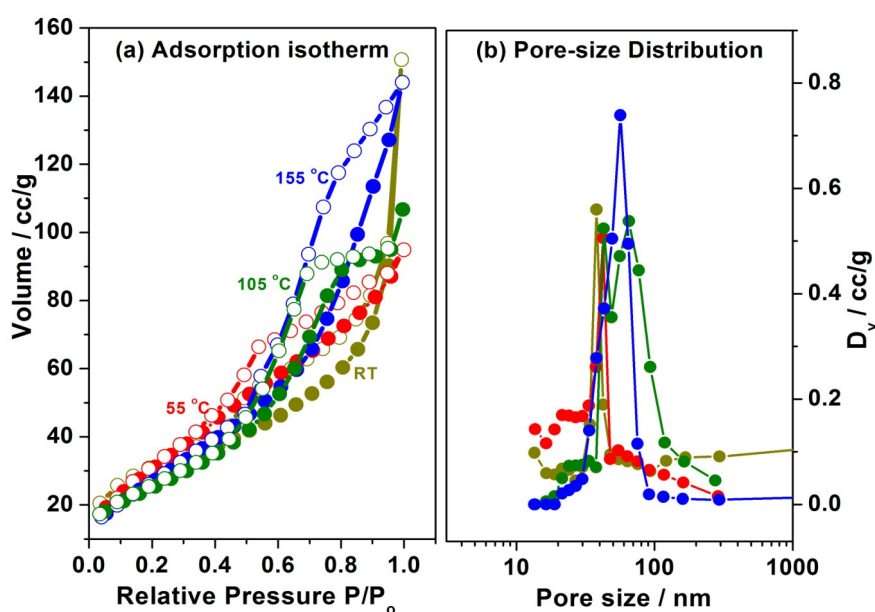
Figure 3.15: *N_2 adsorption isotherm and pore size distribution of active catalyst prepared from molecular adducts dealcoholated at different temperatures.*

BET surface area, pore volume and pore diameter values are given in Table 3.3. Among all the catalyst Ti-MgMeOH has highest surface area of 123 m^2/g and lowest surface area by Ti-MgMeOH-RT. From the Table 3, as the dealcoholation temperature for molecular adduct increases, or in other words as the stoichiometry decreases for molecular adduct, surface area

Table 3.3: *Textural characteristics of different stoichiometric molecular adducts derived titanated active catalyst.*

S.No	Active catalyst	Ti Wt%	Particle Morphology	Pore Volume (cc/g)	Pore diameter (Å)	Surface area (m^2/g)
1	Ti-MgMeOH-RT	13	Spherical	0.133	41	102
2	Ti-MgMeOH-55	9.5	Spherical	0.165	57	106
3	Ti-MgMeOH-105	4.9	Spherical	0.223	130	115
4	Ti-MgMeOH-155	6.8	Spherical	0.241	127	123

Table 3.4*: Ethylene polymerization results of using active catalyst derived from different stoichiometries of molecular adduct*

S.No	Support	Ti wt% (mmol)	Co-catalyst	Condition	PE Yield (g/g of catalyst)	PE Yield (g/mmol of Ti)	Mn (Mw) gmol^{-1}	MWD
1	Ti-MgMeOH-RT	13 (0.27)	Me$_3$Al	75°C, 5atm	7245	2683	26723 (275339)	13.4
2	Ti-MgMeOH-55	9.5 (0.197)	Me$_3$Al	75°C, 5atm	7690	3910	14775 (165480)	11.2
3	Ti-MgMeOH-105	4.9 (0.104)	Me$_3$Al	75°C, 5atm	8507	8180	19140 (185660)	9.7
4	Ti-MgMeOH-155	6.8 (0.144)	Me$_3$Al	75°C, 5atm	10343	7183	30727 (255039)	8.3

Catalyst quantity = 0.1g; Al/Ti = 200, 50, 10 and 50 for MgMeOH, MgEtOH, MgBzOH and MgCyOH respectively.

of the catalyst also increases. This could be due to highly complex mechanism involving dealcoholation in molecular adduct as well as titanium active catalyst synthesis hence breaking of crystallites of $MgCl_2$. The amount of titanium in the final active catalyst also varies with stoichiometry in the precursor. In general, titanation content is decreasing as the temperature for dealcoholation is increasing and found lowest with Ti-MgMeOH-105 active catalyst (Table 3.3.). All the active catalyst is exhibits spherical particle shape.

3.2.3.5 Ethylene Polymerization

Ethylene polymerization results from **Table 3.1.** suggests, the optimised condition for maximum activity of the Ti-MgMeOH-RT is ethylene polymerization at 75 ^{o}C and 5 atm pressure with Me_3Al as co-catalyst. So all the active catalysts from different precursor have been tested for ethylene polymerization with the above mentioned condition and the results are given in **Table 3.4.** Among the reaction results shown , the active catalyst containing lowest titanium content (4.9 wt %) showing best reactivity of 8180 PE g/mmol of Ti. The single phase adduct (MgMeOH-RT) derived active catalyst showing lowest activity of 2683.3 PE g/mmol of Ti with maximum titanium content of 13 wt%. In general reactivity of the catalyst follows the order with respect to the Ti content in the active catalyst and following the order of Ti-MgMeOH-105 > Ti-MgMeOH-155 > Ti-MgMeOH-55 > Ti-MgMeOH-RT. Though surface area of Ti-MgMeOH-155 (123 m^2/g) is higher than Ti-MgMeOH-105 (115 m^2/g), the latter catalyst shows higher productivity implies surface area is not the only criteria for the better activity of the heterogeneous Z-N catalyst. Molecular weight distribution of PE obtained by Ti-MgMeOH-155 catalyst shows lowest value of 8.3 indicates active sites are distributed in a better way than the other catalysts. Above all, the difference in the activity of the Z-N with respect to the precursor stoichiometry of $MgCl_2.xCH_3OH$ confirms the importance of the design of the *super active* catalyst by controlling the stoichiometry around Mg^{2+} centre.

3.3 Conclusion

Single phase MgMeOH adduct and its active catalyst Ti-MgMeOH were synthesized and subjected to detailed structural and spectroscopic investigations. The crystal structure of the MgMeOH adduct belongs to a rhombohedral symmetry with layered structure, whereas a highly disordered δ-$MgCl_2$ nano-crystalline structure has been observed for Ti-MgMeOH. Six methanol molecules are present in a magnetically equivalent environment around the Mg^{2+} in an octahedron environment. The textural properties of the active catalyst show the presence of a maximum of mesopores and a high surface area with an optimum amount of $TiCl_x$ species on the surface. The ethylene polymerization reaction shows 6 times better activity with Ti-MgMeOH compared to a commercial catalyst under comparable conditions. The higher activity of the Ti-MgMeOH catalyst with Me_3Al could be due to the easy accessibility of cocatalyst to the active Ti^{n+} species due to the mesoporous nature of the active catalyst.

MgMeOH-RT (MgMeOH) adduct have been dealcoholated at different temperature to alter the stoichiometry around Mg^{2+}. Variable temperature NMR experiments demonstrate the changing stoichiometry of the adduct and, induced, structural alterations. Active catalyst derived from the respective molecular adducts showing type-1V isotherm with H3 hysteresis. Titanium content present in the active catalyst varies with the stoichiometry around Mg^{2+}. Lowest titanium present in the active catalyst (Ti-MgMeOH-105) showing the best catalytic activity among all active catalysts. Structure-activity correlation indicates surface area is not the only factor for the better activity. Above studies concludes the importance of molecular adduct stoichiometry as an important factor in the design of better heterogeneous Z-N catalyst with tailored properties.

3.4 References

1. (a) Ziegler, K.; Holzkamp, E.; Breil, H.; Martin, H. *Angew. Chem.* **1955**, *67,* 541. (b) Ziegler, K.; Holzkamp, E.; Breil, H.; Martin, H. *Angew. Chem.* **1955,** *67,* 426

2. (a) Natta, G. *J PolymSci.***1955,** *16,* 143. (b) Natta, G.; Pino, P.; Corradini, P.; Danusso, F.; Mantica, E.; Mazzanti, G.; Moraglio, G. *J. Am. Chem. Soc.* **1955,** *77,* 1708.

3. (a) Kashiwa, N.; Fujimura, H.; Tokuzumi, Y. JP Patent 1031698. (b) Kashiwa, N. *Polym.J.* **1980,** *12,* 603. (c) Kashiwa, N.;J. Polym. Sci., Part A: Polym. Chem., **2004,** *42,* 1. (d) Kashiwa, N.; Yoshitake, *J. Makromol. Chem. Rapid Commun.* **1983,** *4,* 41.

4. Hock, C.W. *J Polym Sci.,Polym. Chem.* **1966,** *4,*3055.

5. Boor Jr, J. Ziegler-Natta Catalysts and Polymerization. Academic Press, New York, **1979**

6. Hutchinson, R. A. W. H Ray*, J Appl Polym Sci.***1991,** *43,* 1271.

7. Galli, P. *J Macromol Sci.-Phys B* **1996,** *35,* 427.

8. McKenna, T.F.; Soares, J.P.B. *Chem Eng Sci.* **2001,** *56,* 3931.

9. Cecchin, G.; Morini, G.; Pelliconi, A. *Macromol. Symp.* **2001,** *173,* 195

10. Auriemma, F.; De Rosa, C.*Chem Mater.***2007,***19,* 5803.

11. Busico, V.; Causa, M.; Cipullo, R.; Credendino, R.; Cutillo, F.; Friederichs, N.; Lamanna, R.; Segre, A.; Castellit, V. V. *J. Phys. Chem. C.***2008,** *112,* 1081.

12. Monaco, G.; Toto, M.; Guerra, G.; Corradini, P.; Cavallo, L. *Macromolecules* **2000,** *33,* 8953.

13. Boero, M.; Parrinello, M.; Terakura, K. *Surf. Sci.***1999,** *438,* 1

14. Seth, M.; Margl , P. M.; Ziegler, T. *Macromolecules* **2002,***35,* 7815.

15. Stukalov, D.V.; Zakharov, V.A. *J. Phys. Chem. C* **2009,***113,* 21376.

16. Di Noto, V.; Fregonese, D.; Marigo, A.; Bresadola, S. *Macromol. Chem. Phys* **1998,***199,* 633.

17. Mori, H.; Sawada, M.; Higuchi, T.; Hasebe, K.; Otsuka, N.; Terano, M. *Macromol. Rapid Commun.***1999,***20,* 245.

18. Kim, S. H.; Somorjai, G. A. *Proc. Natl. Acad. Sci.* USA **2006,** *103,* 15289.

19. Andoni, A.; Chadwick, J. C.; Milani, S.; Niemantsverdriet, H.; Thüne, P.C. *J. Catal.* **2007,***247,* 129

20. Potapov, A.G.; Bukatov, G. D.; Zakharov, V.A. *J. Mol. Catal. A: Chem.***2010,** *316,* 95.

21. Brambilla, L.; Zerbi, G.; Piemontesi, F.; Nascetti, S.; Morini, G. *J. Phys. Chem. C.***2010**, *114,* 11475.

22. Sobota, P. *Coord. Chem. Rev.,* **2004,** *248,* 1047.

23. Kim, S. H.; Somorjai, G. A. *J. Phys. Chem. B,* **2002,** *106,* 1386.

24. Sozzani, P.; Bracco, S.; Comotti, A.; Simonutti, R.; Camurati, I. *J. Am. Chem. Soc.*, **2003,** *125,* 12881.

25. Kim, S. H.; Craig, R.T.; Somorjai, G.A. *Langmuir,* **2000,** *16,* 9414.

26. Boero, M.; Parrinello, M.; Terakura, K. *J. Am. Chem. Soc.***1998,** *120*, 2746.

27. Bart, J. C. *J. Mater. Sci.,* **1995,** *30,* 2809.

28. Yang, C. B. ; Hsu, C. C. *Polym. Bull.*, **1993,** *30,* 52.

29. Thushara, K. S.; Mathew, R.; Ajithkumar, T. G.; Rajamohanan, P. R.; Bhaduri, S.; Gopinath, C. S.*J. Phys. Chem. C,* **2009,** *113,* 8556.

30. Gnanakumar, E. S.; Thushara, K. S.; Bhange, D. S.; Mathew, R.; Ajithkumar, T.G.; Rajamohanan, P.R.; Bhaduri, S.; Gopinath, C. S. *Dalton Trans.,* **2011,** *40,* 10936.

31. Thushara, K. S.; Gnanakumar, E. S.; Mathew, R.; Ajithkumar, T.G.; Rajamohanan, P.R.; Bhaduri, S.; Gopinath, C. S. *Dalton Trans.,* **2012**, *41,* 11311.

32. Jr. Moore, E. P.; In The Rebirth of Polypropylene: Supported Catalysts; Hanser Publishers: New York, **1998,** pp 45-71.

33. Albizzati, E.; Giannini, U.; Collina, G.; Noristi, L. In Polypropylene Handbook: Polymerization, Characterization, Properties, Applications; Moore, E. P. Jr., Ed.; Hanser Publishers: New York, **1996,** pp 11-111.

34. Forte, M. C.; Coutinho*,* F. M. B. *Eur. Polym. J*. **1996,***32,* 223.

35. Thushara, K. S.; Gnanakumar, E. S.; Mathew, R.; Jha, R. K.; Ajithkumar, T. G.; Rajamohanan, P. R.; Sarma, K.; Padmanabhan, S.; Bhaduri, S.; Gopinath, C. S. *J. Phys. Chem. C,* **2011,** *115,* 1952.

36. Gnanakumar, E. S.; Thushara, K. S.; Gowda, R. R.; Raman, S. K.; Ajithkumar, T. G.; Rajamohanan, P. R.; Chakraborty, D.; Gopinath, C. S. *J. Phys. Chem. C.* **2012,** 116, 24115.

37. Seenivasan, K.; Sommazzi, A.; Bonino, F.; Bordiga, S.; Groppo, E. *Chem. Eur. J.* **2011,** *17,* 8648.

38. Buscio, V.; Corradini, P.; Martino, L.; Proto, A.; Savino, V. *Makromol. Chem.* **1985,***186,* 1279.

39. Correa, A.; Piemontesi, F.; Morini, G.; Cavallo, L. *Macromolecules* **2007,***40,* 9181.

40. Sacchi, M. C.; Forlini, F.; Tritto, I.; Mendichi, R.; Zannoni, G. *Macromolecules* **1992,** *25,* 5914.

41. Valle, G.; Baruzzi, G.; Paganetto, G.; Depaoli, G.; Zannetti, R.; Marigo, R. *Inorg. Chim. Acta.,* **1989,***156,* 157.

42. Di Noto, V.; Bresadola, S.; Zannetti, R.; Viviani*,* M. *Z. Kristallogr.,***1993,** *204,* 263.

43. Magalhase, D. N. T.; Filho, O. D. C.; Coutinho, F. M. B. *Eur. Polym. J.* **1991,** *27,*827.

44. Malizia, F.; Fait, A.; Cruciani, G. *Chem. Eur. J.***2011,** *17,* 13892.

45. Xu, R.; Liu, D.; Wang, S.; Wang, N.; Mao, B. *J. Mol. Catal. A* **2007,** *263,* 86.

46. Ye, Z.-Y.; Wang, L.; Feng, L.-F.; Gu, X.-P.; Chen, H.-H.; Zhang, P. -Y.; Pan, J.; Jiang, S.; Feng, L.-X. *J. Polym. Sci., Part A: Polym. Chem.* **2002,** *40,* 3112.

47. Tewell, C. R.; Malizia, F.; Ager III, J. W.; Somorjai, G. A. *J. Phys.Chem. B* **2002**, *106,* 2946.

48. Balasubrahmanyam, K. *J. Chem. Phys.* **1966,** *44,* 3270.

49. Ronkko, H. L.; Knuutilla, H.; Denifl, P.; Leinonen, T.; Venalainen, T. *J. Mol. Catal. A: Chem.,* **2007**,*278,* 127

50. Huang, R.; Malizia, F.; Pennini, G.; Koning, C. E.; Chadwick, J.C. *Macromol. Rapid Commun.* **2008,** *29, 1732.*

51. Sing, K. S. W.; Everett, D. H.; Haul, R. A. W.; Moscou, L.;Pierotti, R. A.; Rouquerol, J.; Siemieniewska, T. Pure Appl. Chem. 1985, 57, 603.

52. Naik, B.; Parida, K. M.; Gopinath, C. S. *J. Phys. Chem. C* **2010,** *114,* 19473.

53. a) Reddy, A. S.; Gopinath, C. S.; Chilukuri, S. *J. Catal,* **2006,** *243*, 278. b) Velu, S.; Suzuki, K.; Vijayaraj, M.; Barman, S.; Gopinath, C. S., *Appl. Catal. B* **2005,** *55*, 287.

54. a) Sivaranjani, K.; Verma, A.; Gopinath, C. S. *Green Chem.* **2012**, 14, 461. b) Murugan, B.; Ramaswamy, A. V.; Srinivasa, D.; Gopinath, C. S.; Ramaswamy, V. *Chem. Mater.* **2005,** *17*, 3983.

55. Gnanakumar, E. S Gowda, R. R.; Srikanth,K; S. K.; Ajithkumar, T. G.; Rajamohanan, P. R.; Chakraborty, D.; Gopinath, C. S. *ACS Catal.* **2013**, *3,* 303

Chapter 4

Bulky MgCl$_2$.xROH Molecular Adducts and Its Influence in Polyethylene Production

Part A: $MgCl_2.6C_6H_{11}OH$

4.1 Introduction

Though several decades passed after the discovery of Z-N catalyst [1], heterogeneous $MgCl_2$ supported $TiCl_4$/alkylaluminium system still remains the irreplaceable catalyst for many industrial productions of polymers in spite of its multisite in nature [2]. These supported catalysts not only simplify the industrial process of polyolefin production but also can tune the property of polymers by simply controlling the morphology of the active catalysts [3]. Lewis bases such as alcohol, esters, ethers, etc., are important and indispensable components to activate $MgCl_2$ and to act as electron donor (ED) to increase the stereo specificity of propylene polymerization [4−6]. It is also to be underscored that the role of alcohol molecules present in the adduct is to make high surface area and porous support. Further, alcohol molecules do not have the role of an internal donor since all the alcohol molecules will be eventually removed at the final stages of Z−N catalyst preparation. However, very few crystal structures of intermediate and final compounds are available [4]. To date, many generations of heterogeneous Z−N catalytic systems have been reported based on the Lewis bases used [2, 7, 8]. For the design of new Z−N catalytic systems, development of new Lewis bases will be an important criterion. Most importantly, activation of $TiCl_4$/AlR_3 (R = Me, Et, etc.) by $MgCl_2$ support depends on the crystallographic structure of the support, which is similar to the role of ligands in the homogeneous catalyst [9].

Though technologically Z−N catalyst has matured to a sophisticated level, the molecular science behind the role of support and various key interactions of the active components in the heterogeneous Z−N catalyst is still unclear [10−16]. Partly it is due to the complex nature of active sites of $TiCl_x$ on $MgCl_2$ under polymerization conditions and the high sensitivity of catalyst components present in Z−N systems toward the atmosphere. Now it is a big challenge to techniques such as surface science, structural, spectroscopy, and

theoretical methods to determine the role of support for surface activation in supported $MgCl_2$ in Z−N catalyst [17−21]. Experimental and theoretical efforts have been taken to identify the key structural aspects of support and its influence in catalytic activity. Indeed, $MgCl_2$ surface exposing certain crystallographic planes, especially (110) lateral cuts of $MgCl_2$, are more active for polymerization [6, 11].

$MgCl_2 \cdot 6EtOH$ is shown as an active support, and it has been reported that the ratio between $EtOH/MgCl_2$ deeply affects the performance of Z−N catalytic system. Among many possible $MgCl_2 \cdot xROH$ supports, single crystal structure is reported only for two adducts, namely, $MgCl_2 \cdot 6EtOH$ (MgEtOH) and $MgCl_2 \cdot 6BzOH$ [22, 23]. Solid state NMR and crystal structure studies on MgEtOH support clearly indicate the presence of mixed phases of precursor $MgCl_2 \cdot xEtOH$ ($1 \leq x \geq 3$) present in the synthesized supports [24, 25]. Recently many alcohols having different alkyl chains have been used to prepare the well-defined molecular adduct and its polymerization activity for ethylene was studied [26, 27]. It is clear that the nature of alcohol present in the adduct changes many properties, like electronic, textural, and structural, and hence the final Z−N catalysts also show different activity. With different alcohol, it is possible to tune the polymerization activity, and our ultimate aim is to find a suitable molecular adduct for oligomerization of olefins to value-added petrochemicals. We believe it is possible, and systematic efforts are definitely required to achieve this.

In order to understand the complex system consisting of multicomponent, which are interacting with one another, it is essential to understand the physicochemical properties of each component and then allow them to interact together with increasing complexity [16]. The present chapter describes a synthesis procedure to make well-defined $MgCl_2$ based molecular adducts prepared using cyclohexyl, benzyl alcohol and 9-fluorenemethanol (9-FM). The above molecular adducts were named as MgCyOH, MgBzOH and Mg-9FM-EtOH and used as a support material to synthesize active Z−N catalyst after titanation. Structural

insights of molecular adducts and titanated catalysts have been examined through structural, spectroscopic and textural studies toward a better understanding of Z–N catalysis in polymerization reaction at molecular level. This report is a part of on-going efforts in our laboratory to synthesize new molecular adducts with different Lewis bases, exploiting them for polyolefin synthesis with an emphasis on understanding molecular level properties [26, 27].

4.2. RESULTS AND DISCUSSION

4.2.1. Characterization of Adduct

4.2.1.1. Powder X-ray Diffraction.
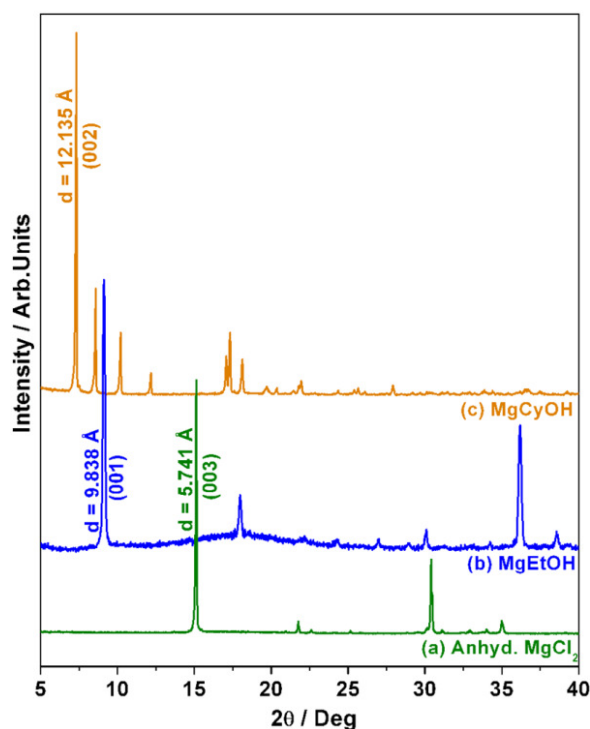
Figure 4.1: *Powder XRD pattern of (a) anhydrous MgCl₂, (b) MgEtOH adduct, and (c) MgCyOH adduct.*

Powder X-ray diffraction pattern (PXRD) of catalyst precursors MgCyOH and MgEtOH are shown and compared with that of anhydrous MgCl$_2$ in Figure 4.1. Anhydrous MgCl$_2$ exhibiting rhombohedral cubic close packing with strong diffraction patterns for (003), (004), and (110) planes at 2θ = 15.1°, 35°, and 50.4°, respectively. First eight intense

features were used for indexing of MgCyOH adduct (see crystallographic data in Table 4.1).

Indexing of

Table 4.1. Crystallographic data

Crystal system: Monoclinic

a = 17.53157 Å   b = 10.30281 Å   c = 14.47035 Å
α = 90.00000°   β= 99.32681°   γ = 90.00000°

Unit cell volume = 2579.15 Å^3
M(20) = 38;   M'(20) = 114
Total number of observed lines = 9

Number of calculated lines (up to the 20th observed d) = 105
Number of unindexed lines = 0

 0.001986 0.005600 0.002914 0.000780 0.000000 0.000000
 0.001986 0.005600 0.002914 0.000780 0.000000 0.000000
 0.001986 0.005600 0.002914 0.000780 0.000000 0.000000

 Number of single indexed lines = 7
 Total number of lines = 8
 a = 17.531054±0.009951 Å   α= 90.000000 ± 0.000000 deg
 b = 10.301604 ± 0.009267 Å   β = 99.327675 ± 0.020346 deg
 c = 14.471068 ± 0.009573 Å   γ = 90.000000 ± 0.000000 deg
 Unit cell volume = 2578.89 Å^3

h	K	l	SST_{obs}	SST_{cal}	δ	$2\theta_{obs}$	$2\theta_{cal}$	d_{obs}	$100 I/I_{max}$
0	0	1	0.002904	0.002914	0.000011	6.178	6.189	14.3058	1.627
1	0	1	0.004106	0.004120	0.000015	7.348	7,361	12.0308	100.00
0	1	0	0.005623	0.005600	0.000023	8.601	8.583	10.2801	40.170
1	0	1		0.005680		8.645			
2	0	0	0.007935	0.007943	0.000008	10.227	10.227	8.6539	15.127
1	1	1	0.011280	0.011280	0.000000	12.194	12.194	7.2583	6.130
2	1	2	0.022081	0.022082	0.000000	17.091	17.092	5.1878	12.317
2	0	2	0.022723	0.022720	0.000002	17.340	17.339	5.1141	14.949
3	0	2	0.024855	0.024851	0.000004	18.142	18.140	4.8898	12.660

Number of observed lines = 8
Number of calculated lines = 9

the diffraction patterns clearly indicates that the sample possesses monoclinic symmetry. A strong (002) diffraction peak appeared at 2θ =7.2° (d = 12.135 Å), which is higher than the d value of MgEtOH precursor (d = 9.838 Å). Higher value of d in MgCyOH is attributed to the bulkiness of cyclohexanol moiety in the adduct. Above high intense peak (002) for MgCyOH adduct clearly shows that the crystal growth occurs along the (00l) plane and similar to that of MgEtOH [26,28]. The unit cell parameters calculated are listed in the crystallographic data. A strong (002) diffraction feature observed below 2θ = 10° and with d = 12.135 Å clearly demonstrates that the MgCyOH adduct exhibits a layered structure because of interaction of cyclohexanol along z-axis around $MgCl_2$.

4.2.1.2. Thermal Analysis

Thermal analysis of MgCyOH adduct has been carried out in N_2 atmosphere at a heating rate of 10 deg/minute, and the results are shown in Figure 4.2. On the basis of the molecular formula $MgCl_2 \cdot 6CyOH$, expected weight loss (86.1%) matches well with that of the experimental weight loss (85.5%) within ±1% error. From the experimental weight loss, the ratio of cyclohexanol/$MgCl_2$ has been derived and confirmed to be six. The weight loss pattern obtained was not similar to MgEtOH adduct, i.e., stepwise weight loss [26] was not observed in MgCyOH. In TGA analysis, there is only one well defined transition that could be observed at 155 °C corresponding to a weight loss of three cyclohexanol. Further, DTA analysis also shows three peaks ≤154 °C, supporting the successive dealcoholation of cyclohexanol molecules. However, above 155 °C, systematic decomposition of CyOH molecules are not observed, rather a continuous weight loss was observed. This observation could be due to the different kind of dynamics of cyclohexanol around Mg^{2+}. Although the boiling point of cyclohexanol is 161 °C, weight loss that occurs below 161 °C indicates a possible weak interaction. Indeed, weight loss that occurs >161 °C hints toward a relatively stronger interaction. The above observations indicate that the nature of interaction of

cyclohexanol with MgCl$_2$ varies with composition and that all cyclohexanol molecules may not have the same interaction with MgCl$_2$. Absence of any weight loss >250 °C clearly indicates that only MgCl$_2$ remains present without any CyOH.
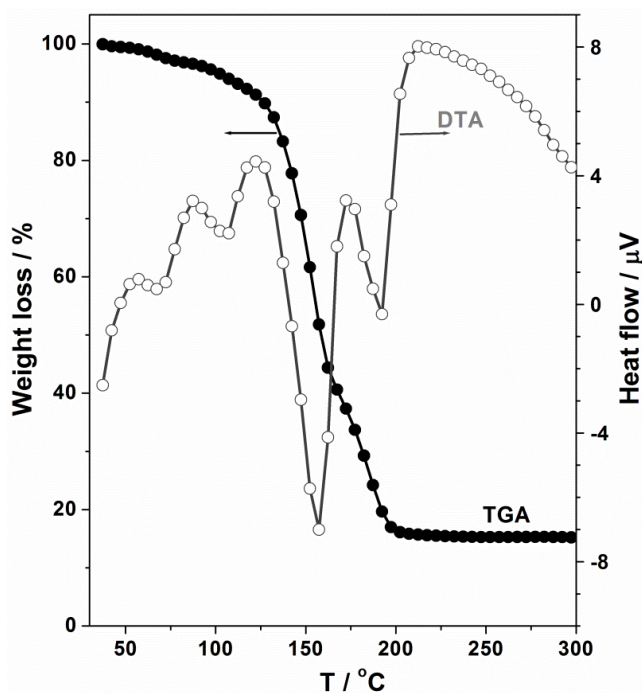
Figure 4.2: *TG-DTA analysis of MgCyOH adduct.*

4.2.1.3. Raman Analysis

Figure 4.3 shows the Raman spectra of MgCyOH, liquid cyclohexanol, and anhydrous MgCl$_2$. MgCl$_2$ belongs to the rhombohedral crystal system with layered structure having D$_{3d}$ space group. The A$_{1g}$ breathing mode of MgCl$_6$ octahedra appears as a high intense peak at 243 cm^{-1}. This is attributed to a distorted octahedron environment with Mg^{2+} coordinated to six chloride ions [26,27,29]. Raman spectrum of pure cyclohexanol shows a peak at 966 cm^{-1} for axial C−OH stretching vibration, and a peak at 1024 cm^{-1} is assigned for the equatorial C−OH stretching vibration [30]. Other than these peaks, pure cyclohexanol exhibits a broad and weak –OH phonon observed between 2850 and 3300 cm^{-1} due to strong intermolecular hydrogen bonding. In MgCyOH, some of the Raman features of neat cyclohexanol disappear,

and new features emerge due to the adduct formation between $MgCl_2$ and cyclcohexanol. Particularly, a new peak at 712 cm^{-1} in MgCyOH Raman spectrum emerges out. This peak in MgCyOH adduct is attributed to Mg^{2+} ion surrounded by six molecules of cyclohexanol in an octahedral ($Mg-O_6$) arrangement. However, the above feature appears at 685−690, 700, and
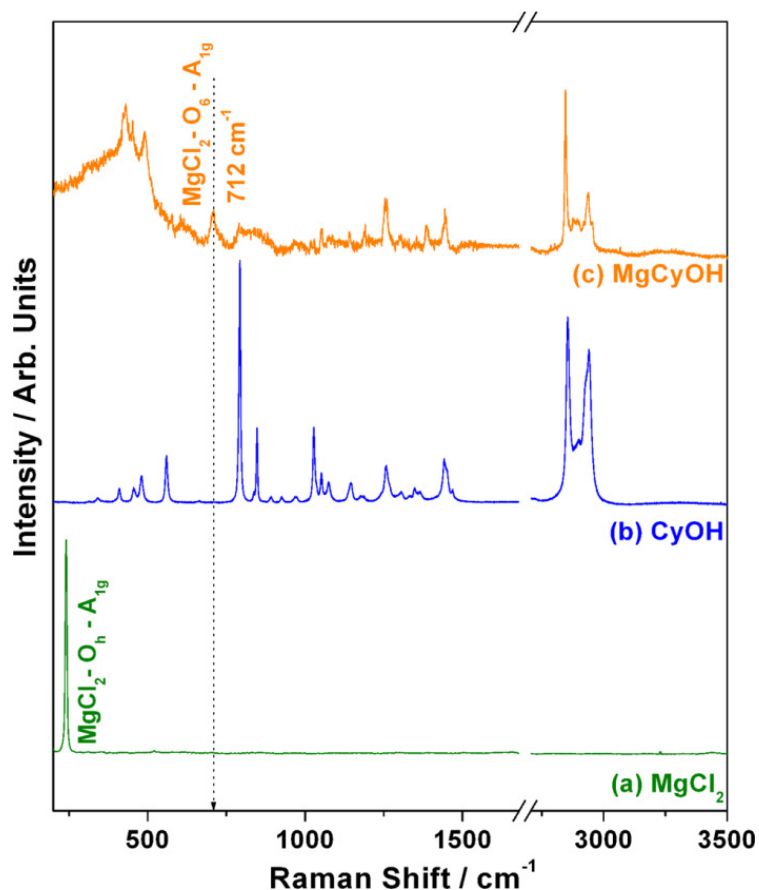
Figure 4.3: *Raman spectra of (a) anhydrous MgCl₂, (b) CyOH, and (c) MgCyOH.*

703 cm^{-1} for MgEtOH adduct, $MgCl_2 \cdot 5EtOH \cdot EtOOCPh$, and $MgCl_2 \cdot 6PhCH_2OH$, respectively [29,26,27a]. These observations underscore the sensitive nature of this peak for electronic and structural changes around Mg^{2+} ion in these adducts. A shift in the $Mg-O_6$ Raman active feature in MgCyOH could be due to the bulkiness of cyclohexanol moiety, which could distort the octahedral environment. Further, the above shift (to 712 cm^{-1}) suggests an overall stronger interaction between Mg^{2+} and cyclohexanol.

4.2.1.4. Solid State NMR
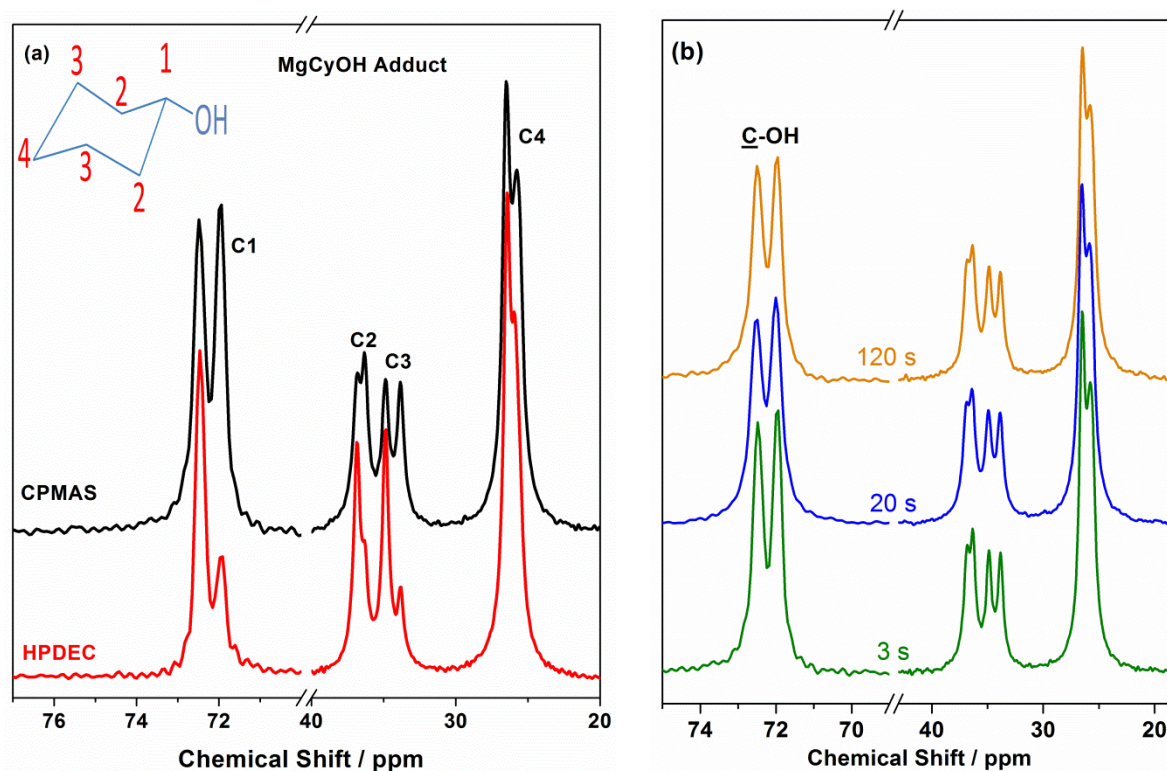
Figure 4.4: *(a) ^{13}C CPMAS 75.5 MHz and HPDEC NMR spectra recorded at D1 as 3 s. (b) ^{13}C CP-MAS NMR spectra of MgCyOH at different relaxation time.*
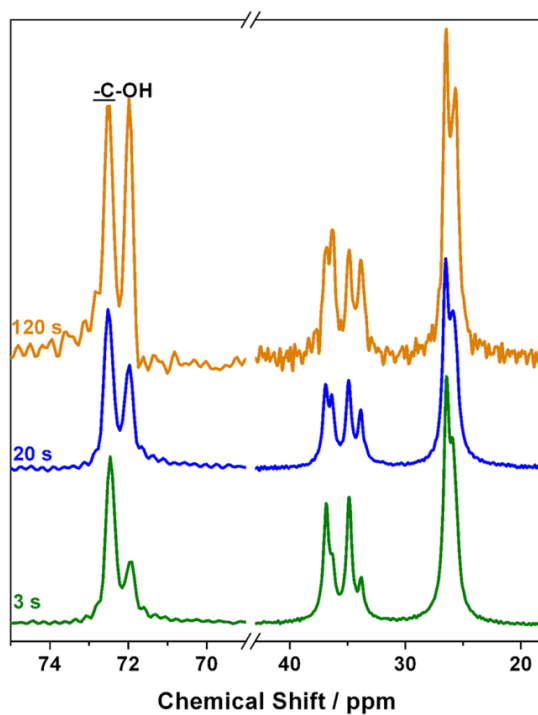
Figure 4.5: *^{13}C HPDEC NMR 75.5 MHz spectrum of MgCyOH adduct recorded at different D1 relaxation times.*

Figure 4.4a shows the ^{13}C CPMAS and HPDEC spectra of MgCyOH adduct recorded at 3 s of relaxation time (D1). ^{13}C CPMAS as well as HPDEC spectrum shows eight peaks with chemical shift values of 72.5, 71.9, 36.9, 36.4, 34.8, 33.9, 26.5, and 25.7 ppm. However, only four types of carbon signals are expected for cyclohexanol in the most favored chair configuration with −OH in equatorial position. Therefore, the observation of eight NMR peaks in MgCyOH adduct dictates the presence of two different types of cyclohexanol molecules. These peaks could be assigned as follows: C1 peaks at 72.5 and 71.9 ppm, C2 peaks at 36.9 and 36.4 ppm, C3 peaks at 34.8 and 33.9 ppm, and finally C4 peaks at 26.5 and 25.7 ppm. Absence of any extra peak in ^{13}C HPDEC clearly signifies that all the cyclohexanol molecules are strongly interacting with $MgCl_2$, in other words, there is no free cyclohexanol molecules in the adduct. However, intensity of the peaks in ^{13}C CPMAS and ^{13}C-HPDEC spectra were found to vary significantly. The intensities of one set of signals that are shielded were found to be weaker in the HPDEC spectrum. Because of the contact time dependency of intensities, the CPMAS spectrum shown in Figure 4.4b need not provide quantitative information. In order to quantify the sets of chemically different cyclohexanol (i.e., 3 + 3 or 2 + 4) among six cyclohexanol molecules around $MgCl_2$, ^{13}C-HPDEC spectra have been recorded at different relaxation delays (D1 at 3, 20, and 120 s), and the results are shown in Figure 4.5. The carbon resonances of one set of cyclohexanol was found to relax very slowly, especially C1, the carbon atom directly attached to −OH, which is coordinated to $MgCl_2$. Spectrum recorded at 120 s (fully relaxed) shows equal intensity for C−OH peaks. Hence, in MgCyOH adduct, cyclohexanol is most likely present in a 3 + 3 chemical environment, and one set of three cyclohexanol molecules experiences very restricted molecular motions, as qualitatively suggested by the longer spin−lattice relaxation time.

4.2.1.5. Surface Morphology

Scanning electron microscope images of MgCyOH adduct is shown in Figure 4.6. MgCyOH adduct has been taken with triblock copolymer to avoid (a) degradation due to the interaction with residual moisture and (b) to minimize agglomeration of particles. Particles are of spherical in shape in a size range of 10–20 μm in diameter. Closer view of the particles clearly shows that each particle consists of many smaller particles. Indeed, this type of inter-particle voids might contribute to the porosity of MgCyOH. This is further supported by surface area measurement, which will be discussed later. The surface of MgCyOH particles is not smoother in nature like MgEtOH particles [27].
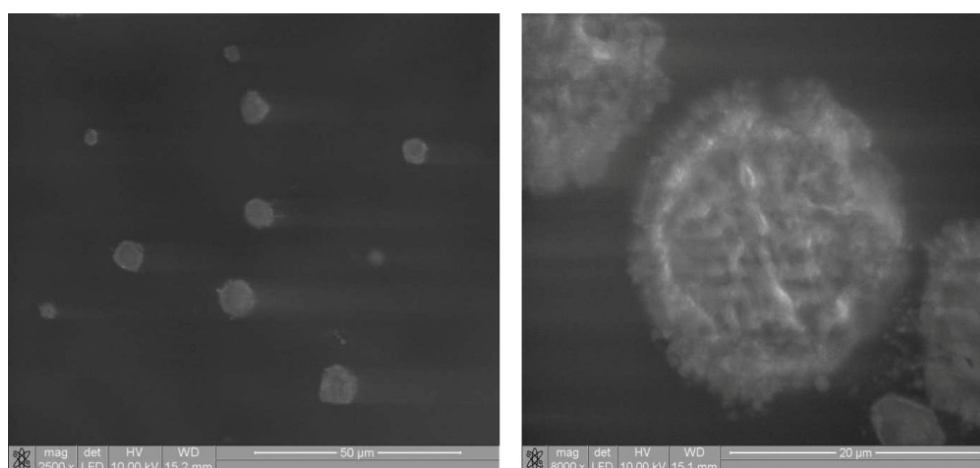
Figure 4.6: *SEM image of MgCyOH adduct at different magnification. Scale bar is 50 μm (left) and 20 μm (right).*

4.2.2. Characterization of Active Catalyst (Ti-MgCyOH)

4.2.2.1. Powder X-ray Diffraction

PXRD of Ti-MgCyOH catalyst is shown in Figure 4.7. Significantly broad and low intensity diffraction features are observed for titanated MgCyOH catalyst. This is in contrast to narrow and intense features observed for MgCyOH. This indicates that the active catalyst is less crystalline in nature. It is to be noted that, during the addition of $TiCl_4$ and subsequent washing, cyclohexanol molecules are removed and that $TiCl_3/TiCl_4$ is incorporated into the

lattice of $MgCl_2$. This severely decreases the crystallinity of $MgCl_2$. Removal of organic moiety during the incorporation of $TiCl_4$ could be the reason for less crystalline nature. Titanated $MgCl_2$ exhibits peaks at ~$2\theta = 17°$ for (003) and broad peaks around 26°, 32°, and 51°. Stacking of Cl−Mg−Cl triple layer is evidenced by the presence of a 17° peak [31,32].
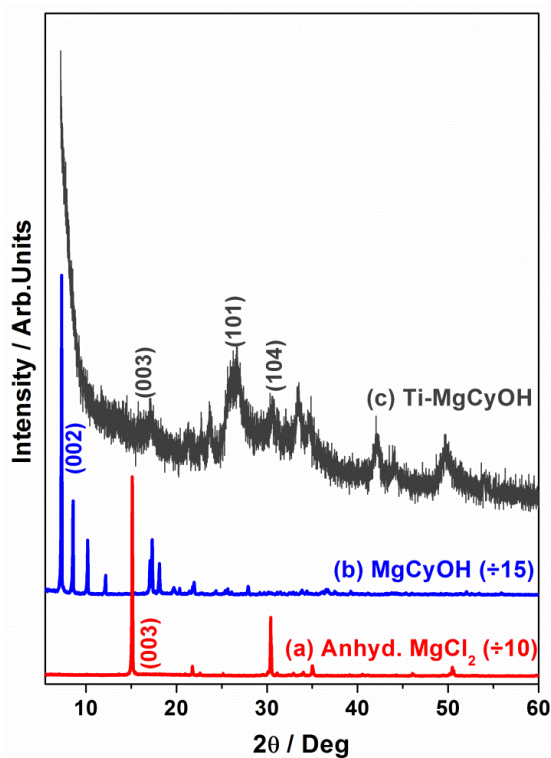
Figure 4.7: *Powder X-ray diffraction pattern of (a) anhydrous MgCl₂ (b) MgCyOH, and (c)Ti-MgCyOH catalyst.*

4.2.2.2 Solid State NMR

Figure 4.8a shows a solid state ^1H MAS NMR spectrum of Ti-MgCyOH catalyst. The peak at 7.5. ppm is attributed to the presence of residual chlorobenzene present inside the pores. Sharp peaks at 1.4 and 1.1 ppm (inset of Figure 4.8a) could be due to the trace amount of hexane, which was used for washing, present inside the pores. Figure 4.8b shows the comparison of the ^{13}C CPMAS spectrum of Ti- MgCyOH catalyst and MgCyOH adduct. A peak at 127.3 ppm in Ti-MgCyOH catalyst spectrum demonstrates the presence of chlorobenzene in the active catalyst. The presence of signals in the aliphatic region 20−25

ppm is likely to be associated with availability of physisorbed n-hexane on the pores of active catalyst. The absence of all cyclohexanol features in the active catalyst (Figure 4.8b) confirms that the cyclohexanol molecules are washed away during the active catalyst preparation.
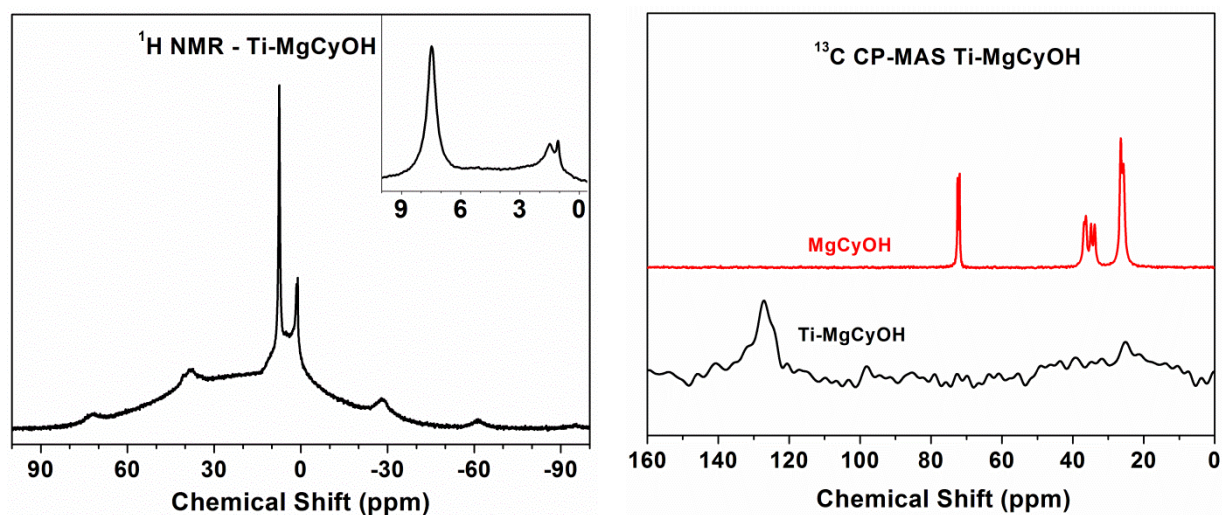
Figure 4.8. *(a) Solid state ^1H MAS NMR spectrum of Ti-MgCyOH and (b) ^{13}C CPMAS spectrum of the Ti-CyOH compared with MgCyOH.*

4.2.2.3 Thermal Analysis

Thermal analysis of Ti-MgCyOH has been carried out in N_2 atmosphere at a heating rate of 10deg/minute, and the results are shown in Figure 4.9. Compared to MgCyOH adduct, an entirely different TG-DTA pattern was observed for Ti-MgCyOH. About 35% weight loss has been observed in Ti-MgCyOH. This weight loss could be due to the presence of chlorobenzene residue deposited during the synthesis of active catalyst. Further, some amount of n-hexane that remains even after thorough washing of active titanated catalyst adds to the weight loss. In fact, the presence of the above two organic moieties were very clear from the solid state NMR spectrum (Figure 4.8).
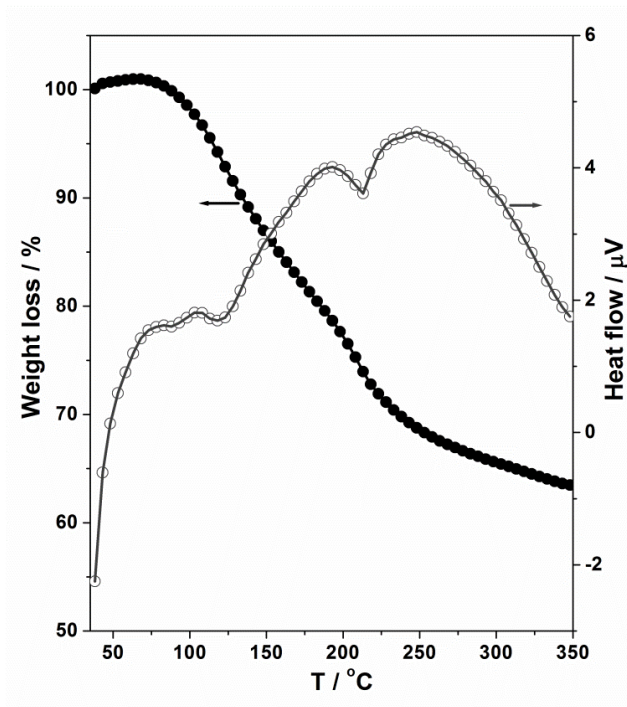
Figure 4.9: *TG-DTA analysis of Ti-MgCyOH.*

4.2.2.4. Scanning Electron Microscopy

.
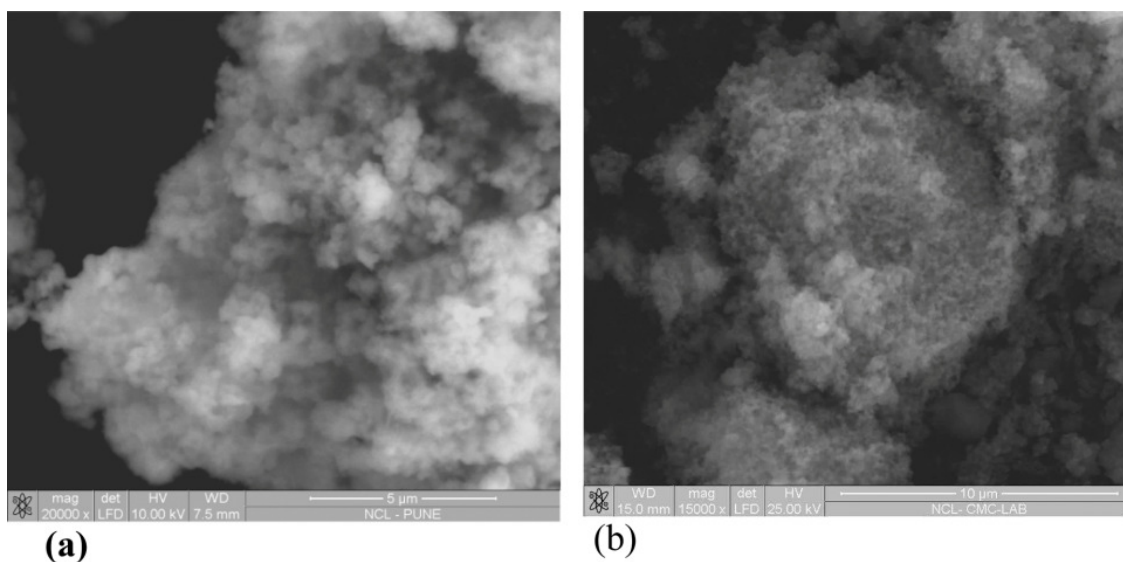
Figure 4.10: *SEM image of Ti-MgCyOH catalyst at different magnification. Scale bar is (a) 5 μm and (b) 10 μm. A single spherical particle is shown in the SEM image panel b.*

Scanning electron microscope images of Ti-MgCyOH are shown at different magnification in Figure 4.10. The porous nature of the active catalyst is clearly evident from

SEM images. A closer view (Figure 10a) shows that the active catalyst contains many sub-micrometres size particles composed together and that each particle exhibits a smooth surface. In addition, there are spherical particles present, which also lead to spherical-shaped polyethylene.

4.2.2.5. Textural Properties.
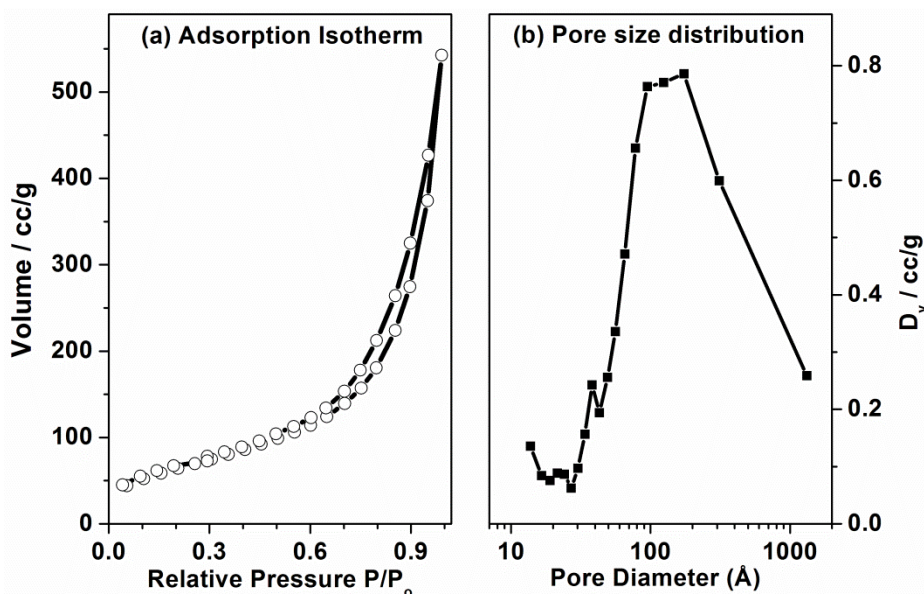
Figure 4.11: *(a) Adsorption isotherm and (b) pore size distribution of Ti-MgCyOH active catalyst.*

Table 4.2: *Textural Characteristics of Molecular Adducts and Titanated Catalyst.*

S.No	Material	Particle Morphology	Pore Volume cc/g	Pore Diameter nm	Surface area m^2/g
1	MgCyOH	Spherical	0.0184	0.59	12.3
2	Ti-MgCyOH	Spherical	0.839	11.8	236
3	MgEtOH	Spherical	NM[a]	NM[a]	1
4	Ti-MgEtOH	Spherical	0.085	3.9	55.4

[a]NM, not measurable

N_2 adsorption isotherm and pore size distribution of active catalyst is shown in Figure 4.11 and given in Table 4.2. BET surface area analysis active catalyst Ti- MgCyOH shows a surface area of 236 m^2/g, which is extremely high compared with earlier reported and

commercial (MgEtOH, 32 m^2/g) Z–N active catalysts [26,27]. High surface area could be due to the removal of bulky cyclohexanol during the active catalyst preparation. Ti-CyOH exhibits an average pore diameter of 12 nm and average pore volume of 0.84 cc/g. The adsorption isotherm of Ti-MgCyOH catalyst shows no adsorption saturation even at high relative pressure (P/P$_o$ = 1) indicating a Type-IV isotherm with H3 hysteresis loop [33,34]. It clearly indicates the contribution of macropores in the active catalyst. Pore size distribution analysis of active catalyst indicates that a major contribution from mesopores in a close pore diameter range of 8–20 nm occurs, and the rest arise from macro- and micropores together. It is very likely the above meso- and macropores allow easy diffusion of reactants as well as chain growth of polymer. Significantly high polymerization activity is related to high molecular weight; however, low molecular weight distribution is attributed to the above textural characteristics (entry 6 in Table 4.3).

4.2.3. Ethylene Polymerization.

Ti-MgCyOH catalyst has been screened for ethylene polymerization using three different co-catalysts without maximizing polymerization activity. Results presented in Table 4.3 are the average values taken after carrying out three sets of experiments. When pressure was increased from 1 to 5atm, the polymerization activity of all the active catalyst increased as expected. Analysis of activity data given in Table 4.3 leads to the following points: (a) Reasonable high activity was observed with any cocatalyst, even at atmospheric pressure of ethylene. However, the activity increases linearly with increasing size of alkyl group in cocatalyst from Me, Et, to isobutyl group. Molecular weight of polyethylene (PE) also increases with the above activity; however, MWD did not change significantly. (b) A very similar trend to that of point (a) is observed at 5atm pressure of ethylene, however, with much higher PE yield. MWD of PE produced at 5atm pressure is significantly narrow,

Table 4.3*: Activity results of catalysts for polymerization reactions*

No	Support	Ti wt% (mmol)	Cocatalyst	Condition	Productivity of PE (gg^{-1} of catalyst)	Productivity of PE ($gmmol^{-1}$ of Ti)	Mn (Mw) $gmol^{-1}$	MWD
1	MgCyOH	9 (0.19)	Me$_3$Al	75°C, 1atm	378	203	7105 (89539)	12.6
2	MgCyOH	9 (0.19)	Et$_3$Al	75°C, 1atm	945	507	9489 (105330)	11.1
3	MgCyOH	9 (0.19)	iBu$_3$Al	75°C, 1atm	1785	958	10603 (130420)	12.3
4	MgCyOH	9 (0.19)	Me$_3$Al	75°C, 5atm	1050	563	20130 (155001)	7.7
5	MgCyOH	9 (0.19)	Et$_3$Al	75°C, 5atm	2835	1521	23154 (159762)	6.9
6	MgCyOH	9 (0.19)	iBu$_3$Al	75°C, 5atm	3570	1918	45801 (297710)	6.5
7	MgEtOH[26]	11 (0.23)	Et$_3$Al	75°C, 5atm	1300	572	22173 (255010)	11.5
8	MgBzOH[27a]	24 (0.51)	Et$_3$Al	75°C, 5atm	960	183	26111 (188000)	7.2

Catalyst quantity = 0.1g; Al/Ti = 300 for MgCyOH support, Al/Ti = 50 for MgEtOH.and Al/Ti = 10. Dry hexane has been used as solvent.

compared to that prepared at atmospheric pressure. (c) Compared to standard MgEtOH, entry 3 exhibits higher activity and PE yield with i-Bu$_3$Al cocatalyst at atmospheric pressure. (d) Among the activity measurements, entry 6 gives the best polymerization activity and comparatively narrow MWD without any external donor. (e) Compared to the activity of titanated catalyst prepared from MgBzOH (MgCl$_2$·6PhCH$_2$OH) [27a], the present set of catalysts exhibits much higher activity even at atmospheric pressure. It is to be noted that high surface area was observed for present Ti- MgCyOH as well as Ti-MgBzOH; nonetheless, a large amount of high boiling PhCH$_2$Cl trapped in the pores of Ti-MgBzOH was attributed to lower polymerization activity [27a]. (f) High porosity and textural properties observed with Ti-MgCyOH and without any impurities, apart from solvents, is likely to be responsible for higher activity.

The difference in polymerization activity with different co-catalysts could be due to different active site formation [35]. Overall performance of Ti-MgCyOH was much better than the commercial Ti-MgEtOH catalyst in terms of activity and MWD. The possible reason could be due to the very high surface area (236 m^2/g) of Ti-MgCyOH and lesser content of active TiCl$_x$ species over the catalyst. We believe that, i-Bu$_3$Al cocatalyst integrates well with the Ti-MgCyOH catalyst structurally, due to the bigger size of the iso-butyl group, and leads to higher activity. However, more experiments are necessary to confirm the above aspects.

4.2.4. CONCLUSIONS

A novel adduct of MgCl$_2$ with bulky cyclohexanol (MgCyOH) has been synthesized. Structural insights of adduct have been revealed by various spectroscopic and morphological characterization methods. NMR and Raman data show the presence of six cyclohexanol molecules in an octahedral environment with magnetically non-equivalent CyOH molecules in a 1:1 ratio. Using this novel support, active Ziegler−Natta catalysts with very high surface area and evenly distributed titanium active species have been prepared. This final active

catalyst Ti-CyOH exhibits much better performance in terms of activity and polymer property compared to commercial Z−N catalyst. Multimodal porous nature of catalyst is apparently responsible for high activity. High activity observed with iso-butyl aluminium cocatalyst on Ti-MgCyOH suggests a possible structural integration, which would also make it electronically integrated. If this is true, higher and selective activity could be achieved with other polymerization reactions. Detailed structural and spectral studies are essential to understand the present catalyst system for better activity.

4.3. Results and Discussion

4.3.1. Characterization of MgBzOH adduct

4.3.1.1. Powder X-ray Diffraction

Figure 4.12 shows a comparison of the powder XRD patterns of the MgBzOH and MgEtOH adducts and anhydrous MgCl$_2$. Assignment of various features are possible due to the Rietveld refinement analysis, which will be discussed below. A rhombohedral cubic close packing structure is exhibited by anhydrous MgCl$_2$. It gives strong diffraction peaks for the
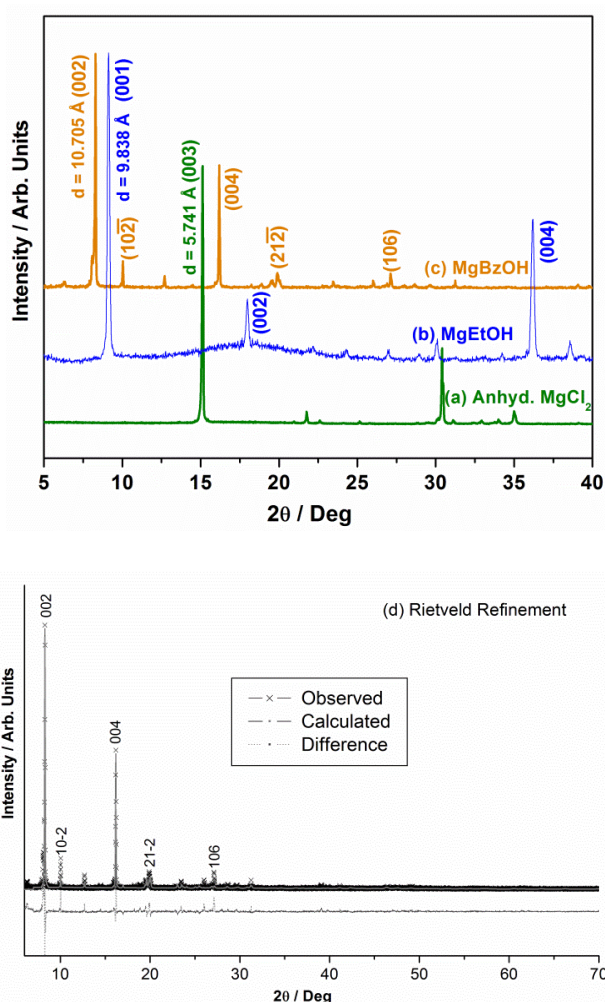
Figure 4.12: *Comparison of powder XRD pattern of (a) anhydrous MgCl$_2$ adduct (b) MgEtOH adduct (c) MgBzOH adduct. (d) Rietveld plot for MgBzOH adduct observed (crosses), calculated (dark grey line) and difference (grey) powder XRD patterns.*

(003), (004) and (110) planes at 2θ = 15.1º, 35º, and 50.4º, respectively [36]. The XRD pattern of the MgBzOH adduct shows a highly intense peak at 8.2º for the (002) plane with other reflections at 16.2º and 27.1º for the (004) and (106) reflections, respectively. The highly intense reflection for the (002) plane clearly shows the growth of the crystal in this preparation method occurs along (00l) planes. The XRD pattern of the MgBzOH adduct fits with the crystal structure belongs to monoclinic symmetry with the space group *P2₁/c*. Nonetheless, in comparison to the MgBzOH adduct, the XRD pattern of the MgEtOH adduct remains in a rhombohedral structure with a highly intense reflection at 9◦ (001) and other selected reflections at 2θ ~ 18º (002) and 2θ ~ 36º (004). A strong diffraction feature at 2θ < 10º for the MgBzOH adduct highlights the fact that the adduct exhibits a layered structure due to relatively weak interaction of the alcohol along the z-axis. Although the benzyl alcohol moiety is bulkier than ethanol, the MgBzOH adduct exhibits a d value of 10.705 Å for the (002) plane due to compact packing.

Figure 4.13*: Ball and stick model representation of crystal structure of MgBzOH adduct, viewed along the b-axis. Small dark grey, blue, red and green spheres represent C, Mg, O and Cl atoms, respectively*

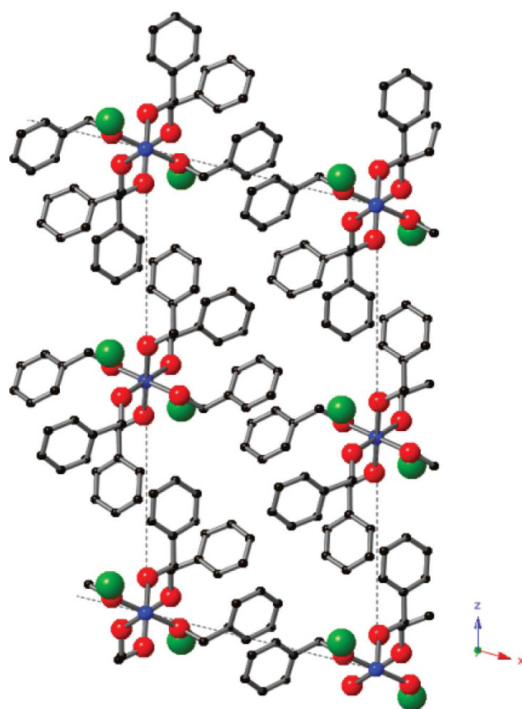Rietveld refinement of the MgBzOH structure with its powder XRD data, based on the atomic positions reported in the literature [22], gave high agreement factors and this may be due to the good quality of the X-ray diffraction data and a possible preferred orientation in the sample along the 00l direction. All of the diffraction features match well with the calculated XRD pattern. The final Rietveld plot is displayed in Figure 4.12d, providing a significant difference in the intensities of the 00l reflections. Figure 4.13 displays a schematic representation of a ball and stick model of the structure of the MgBzOH adduct generated from single crystal data reported in the literature (viewed along the y-axis) [22]. The above structure demonstrates the octahedral coordination of six –OH groups to Mg^{2+}.

4.3.1.2. Thermal Analysis

Figure 4.14 shows TG and DTA results for the MgBzOH adduct. However, TG analysis did not show any well-defined weight loss features, though a large weight loss was observed in the temperature range between 75 and 210 ∘C. The absence of a well-defined weight loss, unlike for MgEtOH and $MgCl_2.4(CH_3)_2CHOH$ adducts [14, 26] shows the absence of successive dissociation of benzyl alcohol from the MgBzOH adduct. The single broad weight loss feature observed for the MgBzOH adduct is likely to be due to the steric bulkiness of the benzyl alcohol molecule in adduct. Nevertheless, DTA shows some sharp features, mainly due to the endothermic desorption of the benzyl alcohol molecule from the MgBzOH adduct. The weight loss feature associated with desorption of the first benzyl alcohol molecule is broad between 75 and 130 ^{o}C and the DTA minimum was observed at 80 ^{o}C. The second weight loss is narrow between 130–150 ^{o}C and the DTA minimum observed at 140 ∘C. Dissociation of third molecule shows no distinct DTA feature. The fourth weight loss is sharp between 165 180 ^{o}C and the DTA minimum is observed at 175 ^{o}C. The fifth and final weight losses occurs with exothermic desorption at >180 ^{o}C and 210 ^{o}C, respectively. The expected total weight loss of the MgBzOH adducts matches well with the

experimental weight loss within ±1% error. The absence of any weight loss above 250 ^{o}C indicates the presence of only $MgCl_2$, after dissociation of all benzyl alcohol molecules. The benzyl alcohol/$MgCl_2$ ratio was found to be six, from the experimental weight loss corresponding to 87.2%.
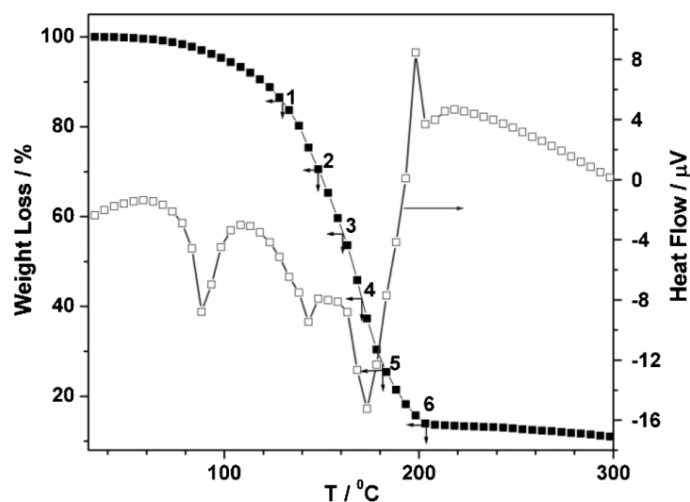
Figure 4.14: *TG-DTA analysis of MgBzOH adduct.*
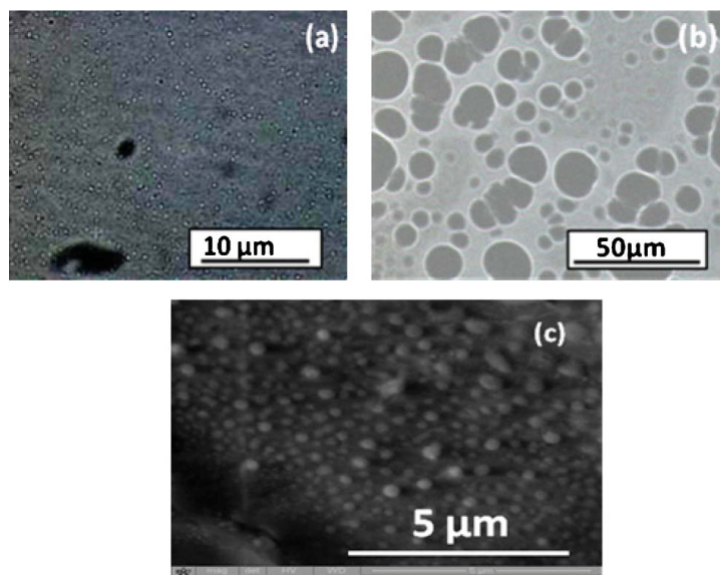
4.3.1.3. Surface Morphology

Figure 4.15: *(a and b) Optimal microscopy, and (c) SEM images of MgBzOH adduct.*
    The optical microscopy images of the MgBzOH adduct are presented in Figure 4.15. Figure 4.15a shows the adduct in a thin liquid layer of triblock copolymer solution and Figure 4.15b is in anhydrous hexane solution. In triblock copolymer solution the adducts were

homogeneously dispersed. All particles are spherical in shape and homogeneously distributed without agglomeration. However, in the case of anhydrous hexane solution the particles are agglomerated and a large distribution of particle size is evident (Figure 4.15b). Due to this, the particles are larger in size, and predominantly spherical in shape. Figure 4.15c shows an SEM image of the MgBzOH adduct. The SEM image reveals the particles are spherical in shape; however, the particle size is not uniform. The size of the particles (0.5 µm) is much smaller than in MgEtOH adducts [26] (20 µm, results not shown). The images show the surface of the adduct is smooth in nature.

4.3.1.4. Raman Analysis

Figure 4.16 shows the Raman spectra of the MgBzOH adduct, with (liquid) benzyl alcohol and anhydrous $MgCl_2$. Crystalline $MgCl_2$ belongs to a layered rhombohedral Structure with D_{3d} space group. The Raman spectrum of anhydrous $MgCl_2$ shows a highly intense peak at 243 cm^{-1} due to the A_{1g} breathing mode of the $MgCl_6$ octahedra in the lattice [29]. This indicates Mg^{2+} is in a distorted octahedral configuration coordinated to six chlorine anions. The Raman spectrum of neat benzyl alcohol shows a very strong Raman band at 1002 cm^{-1} from the phenyl ring breathing mode and a peak at 1027 cm^{-1} from the in-plane C–H bending mode [37]. However, the above features of $MgCl_2$ and neat benzyl alcohol disappear in the Raman spectrum of the adduct and a new peak appears at 703 cm^{-1} for the MgBzOH adduct. This peak is attributed to the symmetric breathing mode of the Mg–O bond formed due to the interaction of Mg^{2+} with alcoholic oxygen atoms. This peak underscores the fact thatMg^{2+} is in an octahedral environment, and surrounded by six benzyl alcohol moieties forming a MgO_6 octahedron. It is to be noted that the above symmetric breathing mode of Mg–O appears at 690 cm^{-1} for the MgEtOH adduct [29]. The shift observed to higher frequency for MgBzOH indicates a significant change in the electronic environment around

Mg^{2+} ion in the case of the MgBzOH adduct, and stronger binding between Mg and O especially is reflected in the Raman spectrum.
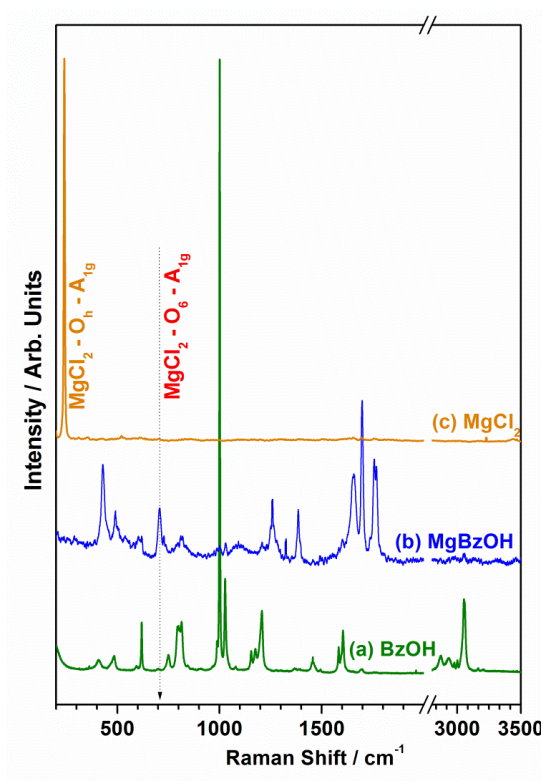
Figure 4.16: *Raman spectrum of (a) benzyl alcohol, (b) MgBzOH adduct, and (c) anhydrous MgCl₂.*

4.3.1.5. Solid State NMR

The MgBzOH adduct prepared has been characterized by solid state ^{13}C CP-MAS NMR. The ^{13}C CP-MAS spectrum of the MgBzOH adduct is given in Figure 4.17 and shows peaks in the region 63 to 67 ppm for $-CH_2OH$ and aromatic peaks between 125 and 140 ppm. Three equally intense peaks were observed for $-CH_2OH$. It clearly indicates that there are three magnetically non-equivalent methylene ($-CH_2OH$) carbons present around the Mg^{2+} ion. The structure of the MgBzOH adduct is similar to that of the MgEtOH adduct where six coordination sites are occupied by benzyl alcohol molecules around an octahedral Mg2+ ion [23,24]. Three different $-CH_2OH$ signals can be attributed to the fact that each pair of alcohols on the x, y and z-axis are likely to have a slightly different arrangement in the crystal

structure. Indeed three different Mg–O bond lengths (2.094, 2.071, 2.078 Å) with O–Mg– O angles of 90.8 to 92.2^o are reported in ref. 22. Two chloride ions are present out of the octahedral coordination sphere in this ionic structure attached through H-bonding with the oxygen of the alcohol. Some of the aromatic carbons that experience the effect of Mg coordination, i.e. the one closer to Mg, also show multiplicities in the MgBzOH adduct. This is clearly visible for the C1 carbon (140 to 134 ppm) and probably also for the C2 (ortho) carbons (127–121 ppm). The other carbons are expected to be less affected by the coordination.
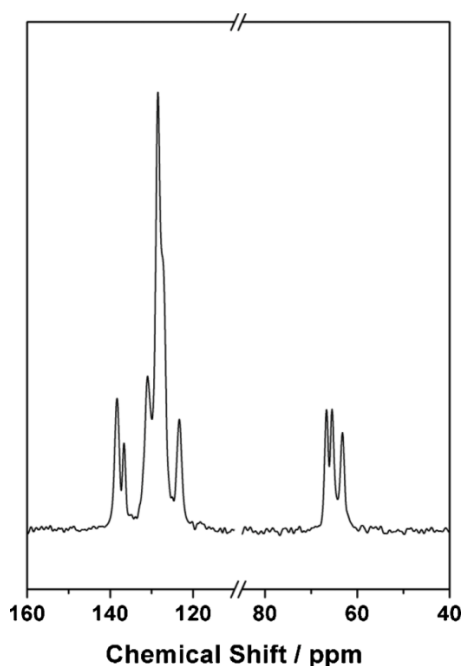
Figure 4.17: *75.5 MHz ^{13}C CP-MAS NMR spectrum of MgBzOH adduct.*

4.3.2. Characterization of Titanated Adduct

4.3.2.1. Powder X-ray Diffraction

Figure. 4.18 shows the powder XRD pattern of the Ti-MgBzOH catalyst and it is compared with that of the pure MgBzOH adduct. A broad peak between 14–21° (003), broad asymmetric halo peaks at 26 and 32° and another peak around 50° were found. This type of XRD pattern has been reported earlier for a titanated catalyst and it corresponds to the

structurally disordered δ-MgCl$_2$ crystal structure [31]. A relatively intense and broad peak at

~18◦ is related to the stacking of Cl–Mg–Cl triple layers along the crystallographic direction.

Two other peaks are related to stacking faults in the Mg–Cl–Mg triple layers [32]. The highly

crystalline natures of the virgin MgBzOH adduct changes into a poorly crystalline Ti-

MgBzOH material. This is due to the removal of most of the benzyl alcohol organic moieties

during the titanated catalyst preparation and the growth of MgCl$_2$ crystallites is restricted by

the active TiCl$_4$ incorporation into the lattice.
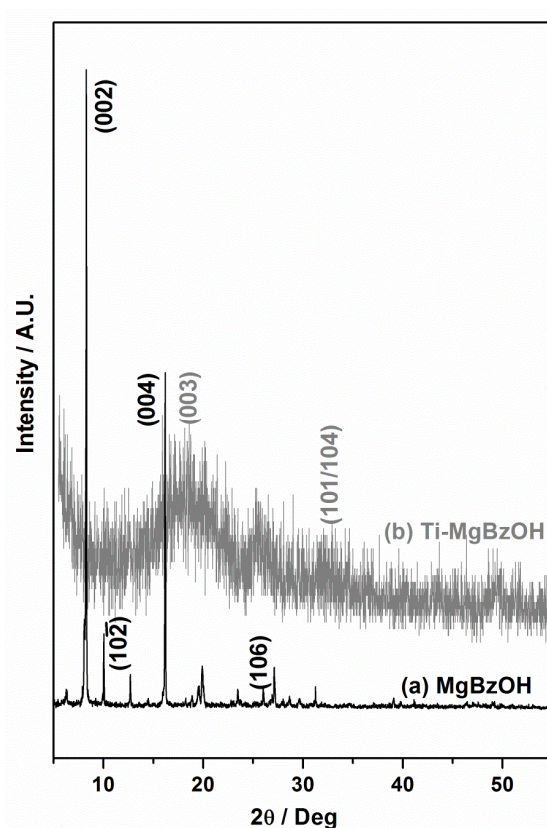
Figure 4.18: *XRD pattern of Ti- MgBzOH catalyst compared with MgBzOH adduct.*

4.3.2.2 Thermal Analysis

Figure 4.19 shows thermal analysis of Ti- MgBzOH catalyst. There is a significant

difference in the TG-DTA results of Ti- MgBzOH catalyst compared to MgBzOH adduct.

There is no significant weight loss below 100°C indicating no loss of any species from Ti-

MgBzOH catalyst. The weight loss associated with Ti- MgBzOH catalyst > 100 ^{o}C might be

due to desorption of chlorobenzene (boiling point 131°C) and benzyl chloride (boiling point 179°C). Chlorobenzene is used as the solvent in the titanation step and small amounts of benzyl chloride is a side product in the reaction between TiCl$_4$ and benzyl alcohol. Small amounts of these relatively higher boiling solvents probably remain trapped in the pores. This result is supported further by NMR of Ti- MgBzOH catalyst.
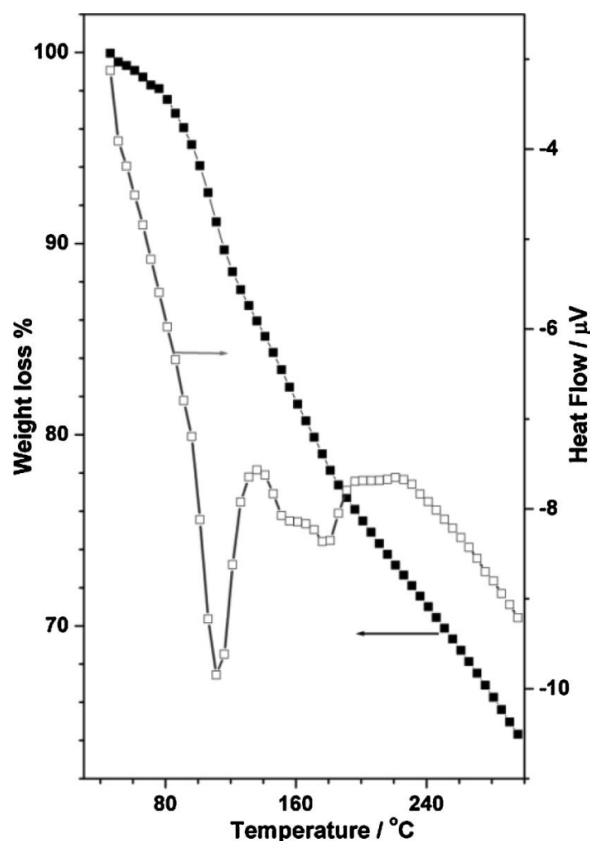
Figure 4.19: *Thermal analysis of Ti- MgBzOH catalyst.*

4.3.2.3. Scanning Electron Microscopy

Figure 4.20 shows SEM images of Ti- MgBzOH catalyst. Highly porous nature of titanated adduct is clearly visible in these pictures. SEM pictures clearly shows that all the particles are of spherical in shape with a narrow particle size distribution. Higher magnification of the particles shows the surface of the particles is smoother in nature.
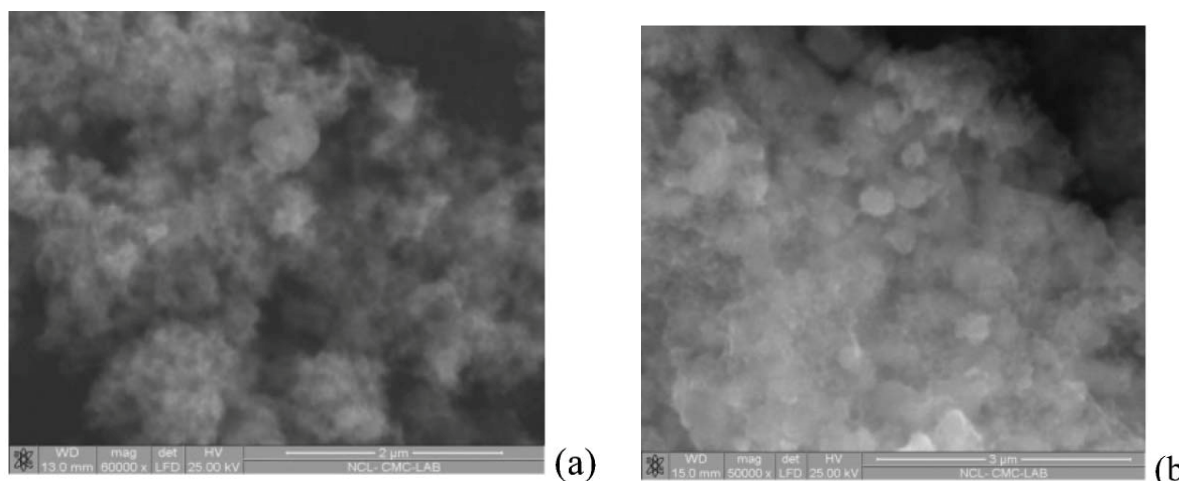
Figure 4.20: *SEM images of Ti- MgBzOH catalyst*

4.3.2.4. Textural Properties
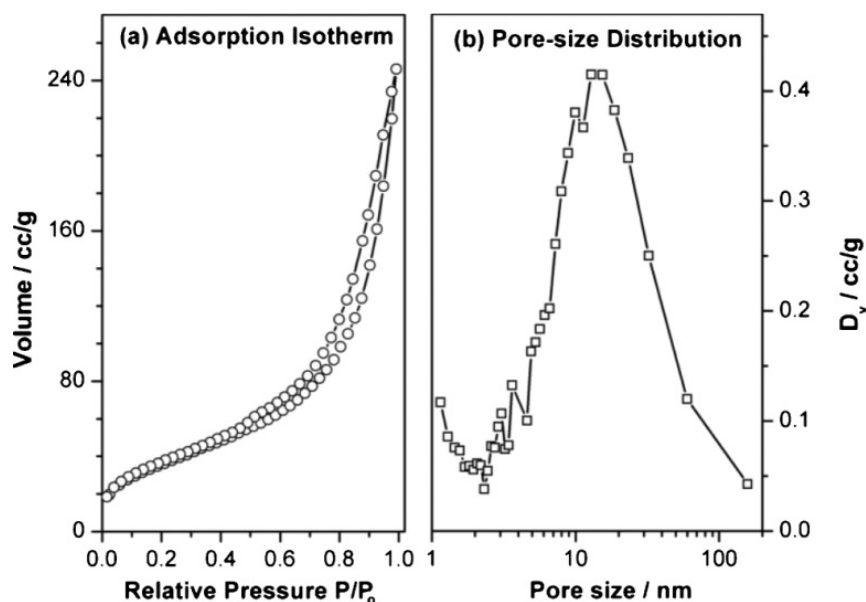
Figure 4.21*: (a) Adsorption isotherm, and (b) pore size distribution curve of Ti- MgBzOH adduct.*

BET method was used to determine the surface area of the Ti-MgBzOH catalysts from nitrogen adsorption–desorption isotherms (Figure 4.21). The Ti-MgBzOH catalyst surface area was found to be 123 m^2 g^{-1} and it is higher than that of the Ti-MgEtOH catalyst (32 m^2 g^{-1}). This is due to the removal of most of the bulky benzyl molecules from the MgBzOH adduct that leads to bigger pores. It is noteworthy that the average pore diameter of Ti- MgBzOH catalyst is found to be 12.3 nm (Figure 4.21b) with a pore volume of 0.381 cm^3

g^{-1}. These values are significantly higher than the values reported for commercial polyolefin catalysts [14, 24, 26, 38].

4.3.2.5 Solid State NMR
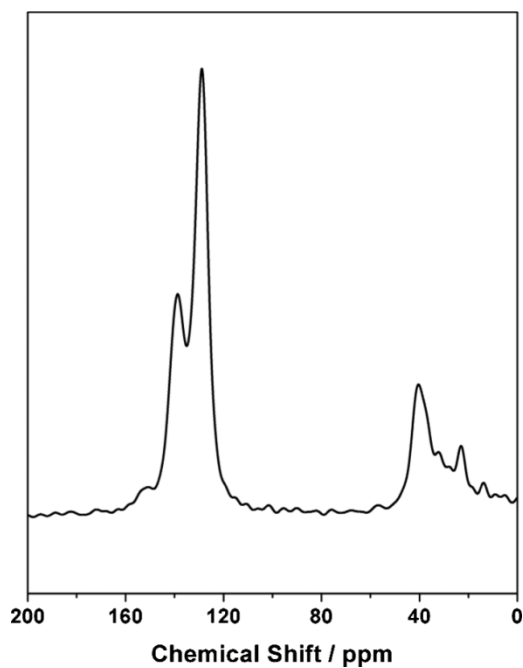
Figure 4.22: ^{13}C *CP-MAS spectra of Ti- MgBzOH.*

Figure 4.22 shows the solid state ^{13}C CP-MAS spectrum of the Ti-MgBzOH catalyst. The ^{13}C CP-MAS spectrum shows the presence of aromatic peaks around 120 to 150 ppm and a peak around 40 ppm. The absence of peaks around 60 to 65 ppm clearly indicates the absence of benzyl alcohol on the MgCl$_2$ surface. Peaks at ~40 ppm in the ^{13}C CPMAS are probably due to the CH$_2$–Cl carbon of benzyl chloride, a side product expected from the reaction between benzyl alcohol and TiCl$_4$. This benzyl chloride formed seemed to be strongly associated with the Ti-MgBzOH catalyst.

4.3.3. Ethylene polymerization

The activity of the Ti- MgBzOH catalyst has been tested for ethylene polymerization activity without any effort to maximize the productivity of polyethylene by optimizing the

reaction conditions. In a typical polymerization, 0.5 L of dry hexane was added to the reactor at 75 $^{\circ}$C, followed by alkyl aluminium (methyl, ethyl, isobutyl alkyl aluminium) and the catalyst was introduced into the reactor under a stream of dry N_2 and then evacuated. Ethylene (5 bar) was then fed at a constant pressure. Polymerization was carried out for 1 h at 75 $^{\circ}$C. For the polymerization reaction alkyl aluminium has been added as a co-catalyst. The activity of the Ti-MgBzOH catalyst under identical conditions is compared with that of the MgEtOH-Ti catalyst in Table 4.4. Activity data reported in Table 4.3 is the average of data collected from three different batches of catalysts. Among three different co-catalyst used, Et_3Al combination gave best activity for Ti-MgBzOH catalyst. The polyethylene yield from the Ti-MgBzOH catalyst is marginally lower than that of the Ti-MgEtOH catalyst. Though the surface area of the Ti-MgBzOH catalyst was much higher than that of the Ti-MgEtOH catalyst, the activity was lower implying that factors other than surface area influence the activity of the catalyst. The large surface area of the Ti-MgBzOH catalyst leads to a very high impregnation of Ti on the $MgCl_2$ surface, however, the polymerization results indicate that the number of active sites on the surface with relatively long life time is slightly less in Ti MgBzOH than in Ti-MgEtOH A plausible explanation for this is discussed later on (Section 4.3.5). The activity results suggest a very large amount of Ti species also leads to a decrease in the activity. The optimum surface area with a lower amount of Ti fixation leads to higher polyolefin activity. The molecular weight (Mw) and molecular weight distribution (MWD) are critical for polymer processing as they are important factors in determining the mechanical and rheological properties of polymers. GPC profile results obtained from polyethylene produced by the Ti-BzOH and Ti-MgEtOH catalysts are shown in Table 1. Polyethylene from Ti-MgBzOH shows a MWD of 7.2. However, polyethylene from Ti-MgEtOH shows a MWD of 11.5. It is likely that the different Ti-content, as well as the origin of the $MgCl_2$ support from different molecular adducts leads to significantly different results.

Table 4.4: *Activity results of the Ti-MgBzOH catalysts for polyethylene production.*

S.No	Support	Ti wt% (mmol)	Co-catalyst	Condition	PE Yield (g/g of catalyst)	PE Yield (g/mmol of Ti)	Mn (Mw) gmol^{-1}	MWD
1	MgBzOH	17 (0.51)	Me$_3$Al	75°C, 5atm	378	74.1	18689(147650)	7.9
2	MgBzOH	17 (0.51)	Et$_3$Al	75°C, 5atm	960	189	26111 (188000)	7.2
3	MgBzOH	17 (0.51)	iBu$_3$Al	75°C, 5atm	689	135.1	21955 (210769)	9.6
7	MgEtOH[14]	11 (0.23)	Et$_3$Al	75°C, 5atm	1300	572	22173 (255010)	11.5

Catalyst quantity = 0.1g; Al/Ti = 10 and 50 for MgBzOH and MgEtOH respectively; Dry hexane has been used as a solvent

4.3.4. Polymer morphology
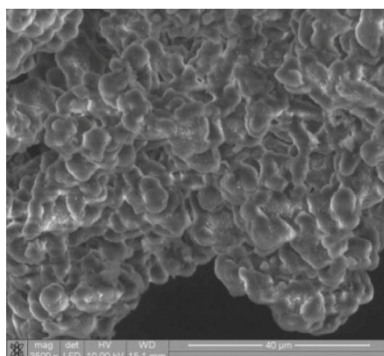
Figure 4.23*: SEM image of polyethylene synthesized using the Ti-MgBzOH catalyst.*

Figure 4.23 shows an SEM image of polyethylene synthesized using the Ti-BzOH catalyst. The surface morphology of the polymer exhibits a spherical shape and replicates the catalyst particle morphology [39–41]. A few particles are agglomerated and not spherical in shape. This is due to the conditions that have been applied for the polymerization reaction which leads to cracks on the catalyst surface. However, a careful analysis of many images of the polymer suggests a relatively low polydispersity of polyethylene. Indeed this is in agreement with the low MWD values obtained for the polyethylene produced using the Ti-MgBzOH catalyst (Table 4.3).

4.3.5 Origin of activity

The detailed preparation, characterization by structural, spectroscopic and microscopic analytical methods and the evaluation of the titanated adducts for ethylene polymerization presented here provide some new information, especially on the molecular level properties and electronic structure of the molecular adducts and corresponding Ziegler catalysts. Although there is already some similar information available in the literature [42,43], it is derived from the analysis of polymer products and hence in an indirect manner. A few points are worth highlighting regarding the influence on catalytic activity. (a) The structure and spectral properties of the MgBzOH adduct and Ti-BzOH catalyst have been sufficiently demonstrated by XRD, NMR, and Raman spectroscopy. (b) Significant changes

in the Raman spectra of MgBzOH and MgEtOH have been observed, indicating a stronger interaction between Mg and O in MgBzOH than MgEtOH. (c) A marginally lower polymerization activity is observed with Ti-MgBzOH compared to Ti-MgEtOH in spite of a higher surface area. Ti-MgBzOH in spite of its high titanium content shows a lower specific activity towards polymerization. In Ziegler catalysts, partial reduction of the catalytically active $Ti^{4+/3+}$ to Ti^{2+} in a side reaction with TEAL is known to be one of the main catalyst deactivation pathways. In our earlier publication we presented evidence indicating that $PhCO_2Et$, a so called internal electron donor, makes the catalyst more resistant towards quick deactivation by co-ordination to the Ti^{4+} center. In the present case the larger pores probably make the catalytically active $Ti^{4+/3+}$ sites more accessible to TEAL resulting in over-reduction and deactivation. Further benzyl chloride trapped in the pores might also be blocking some of the active sites. It is known that a higher surface area generally increases the activity of catalysts. However, low polymerization activity observed with Ti-BzOH , in spite of better textural properties, underscoring the origin of decreased activity is not due to textural properties. Hence from the above discussion and our earlier work on different catalytic systems [44], it is clear that the origin of lower catalytic activity in the present Ti-MgBzOH case, compared to the Ti-MgEtOH catalyst, could be attributed to the lower specific activity of Ti which is probably due to the result of relatively rapid deactivation of the active sites due to over reduction by TEAL.

4.3.6. Conclusion

A new single phase supportingmaterial for Z–N catalysts with an aromatic alcohol (benzyl alcohol) adduct of $MgCl_2$ has been successfully synthesized and characterized by variety of analytical and spectroscopic characterization methods. Notably a stronger interaction between the Mg and O atoms of the OH groups of $PhCH_2OH$ is observed in structural studies and Raman spectra. The titanated MgBzOH catalyst has been characterized

by variety of techniques. Polymerization activity results suggest the surface area of the catalyst is not an important criterion governing the polymerization activity. A significantly high Ti content on the final catalyst surface indicates a strong interaction between the support and Ti, which reduces the specific activity of Ti towards polymerization

Part C: MgCl$_2$-9FM-EtOH

4.4 Results and Discussion

4.4.1 Characterization of MgCl$_2$-9FM-EtOH Adduct

4.4.1.1. Powder X-ray Diffraction
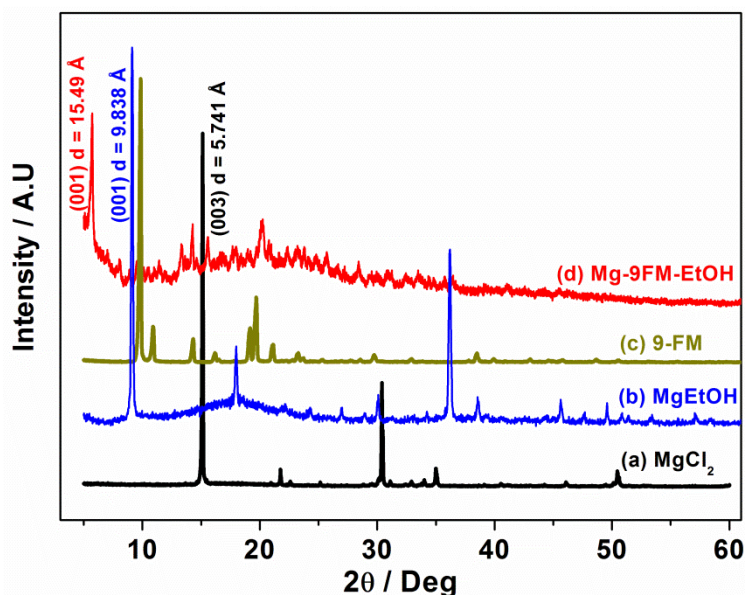
Figure 4.24: *Comparison of powder XRD pattern of (a) anhydrous MgCl$_2$ (b) MgEtOH adduct (c) 9FM and (d) Mg-9FM-EtOH.*

Figure 4.24 shows the comparison of powder XRD of pure MgCl$_2$, MgEtOH, 9FM and Mg-9FM-EtOH. Rhombohedral cubic close packing structure exhibited by anhydrous MgCl$_2$ and it gives a strong diffraction peaks for (003), (004) and (110) planes at 2θ 15.1^o, 35°, and 50.4^o, respectively. XRD pattern of MgEtOH shows a high intensity and characteristic (001) reflection at $2\theta = 9^o$; rather, Mg-9FM-EtOH shows high intensity peak reflection at $2\theta = 5.7^o$. High intense reflection for (001) plane clearly shows the growth of crystal, in azeotropic distillation preparation method, occurs along (00z) planes [26, 28]. Among all XRD patterns, Mg-9FM-EtOH shows significantly different pattern having high intensity peak around 2θ of 5.7^o with d value of 15.49 Å. However, MgEtOH molecular adduct and anhydrous MgCl$_2$ exhibits d value of 9.838 Å and 5.741, respectively, for high intense (00l) peak. Higher d

value for Mg-9FM-EtOH compared with MgEtOH and $MgCl_2$ could be due to bulkiness of 9-FM as Lewis base. Since 9FM is relatively bulkier than ethanol molecule, the distance between Cl-Mg-Cl triple layer increases when Lewis base interacts with Mg^{2+}. Hence, Mg-9FM-EtOH exhibits higher d-value among other adducts. Indeed the 9FM molecule size is 8.76 Å x 7.3 Å, which is much bigger than EtOH molecules.

4.4.1.2 Thermal Analysis
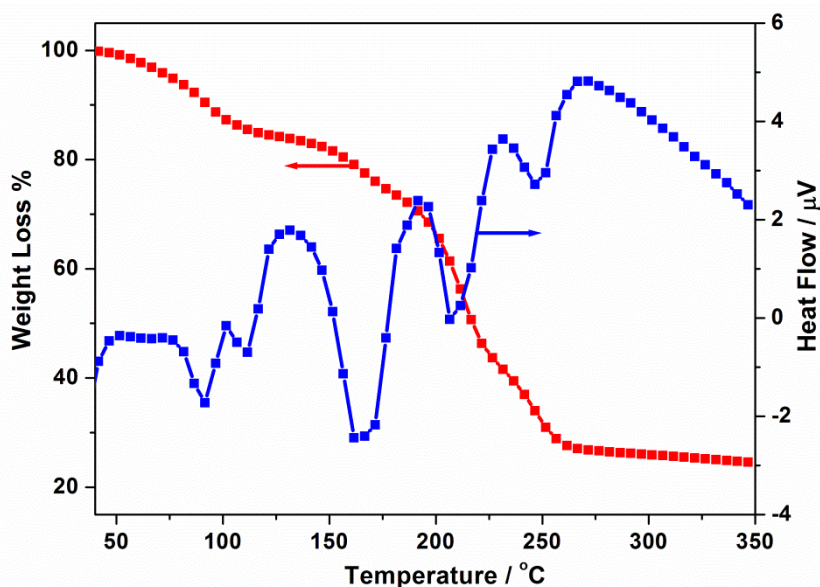
Figure 4.25: *TG-DTA analysis of Mg-9FM-EtOH adduct.*

Figure 4.25 shows the thermogravimetry and differential thermal analysis of Mg-9FM-EtOH adduct. Temperature of the sample was ramped from ambient to 350 °C at 5 °C/min under flow of dry nitrogen (99.999%) at 40 mL/min. Well defined weight loss features were observed in thermal analysis is attributed to successive loss of ethanol as well as 9FM molecules from the molecular adduct. Similarly well defined DTA curve also confirms the successive dealcoholation process is occurs with Mg-9FM-EtOH adduct. Because of the complex nature of the molecular adduct i.e., two different Lewis bases (EtOH and 9FM) have been used, it is difficult to find the dealcoholation temperature of each entities present in the molecular adduct. From the TG-DTA analysis of MgEtOH adduct, it is

expected that EtOH molecule might dissociate from the adduct first due to its lower boiling point compared to 9FM. It is also expected that from the smaller weight loss between RT and ~170 ^{o}C is attributed to loss of EtOH and 9FM dissociation might occur between 150 ^{o}C and 250 ^{o}C. Stoichiometry of the molecular adduct containing 9FM and EtOH was also determined separately by liquid state NMR [24] using a known quantity of the adduct in 1 mL of deutrated acetonitrile containing known amount of a reference compound, methanol. The mole fraction of 9FM and EtOH is estimated from the ^{1}H integrals and used for the calculation of absolute amount of 9FM and EtOH in the adduct, *vide infra* and found the stoichiometry of $MgCl_2$-$(9FM)_{1.1}$-$(EtOH)_{1.23}$.The expected total weight loss of the above stoichiometry found by NMR for $MgCl_2$-9FM-EtOH adduct matches well with the experimental weight loss within ±1% error. Absence of any weight loss above 250 ^{o}C indicates the presence of only $MgCl_2$, after dissociation of all the alcohol molecules.

4.4.1.3 Solid state NMR
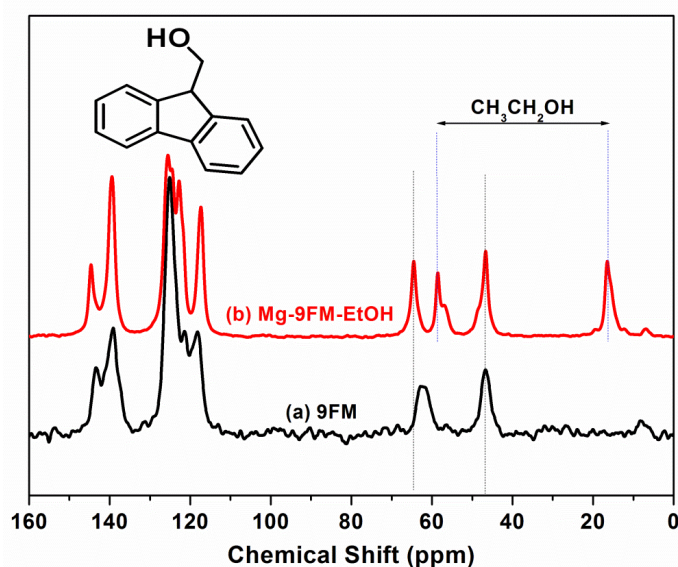
Figure 4.26: *75.5 MHz ^{13}C CP-MAS NMR spectrum of (a) 9-FM and (b) Mg-9FM-EtOH.*

Figure 4.26 shows ^{13}C CPMAS solid state NMR spectrum of pure 9-FM and Mg-9FM-EtOH. Pure 9-FM gives –$\underline{C}H_2$-OH peak at 62.3 ppm, =$\underline{C}H$- (five membered) peak at

46.9 ppm and aromatic peaks between 118 to 144 ppm. Ethanol moieties present in Mg-9FM-EtOH gives the peak at 16.3 and 58.5 for $\underline{C}H_3$- and $-\underline{C}H_2$-OH, respectively. 9FM moieties present in Mg-9FM-EtOH gives the peaks at 46.8, 64.5 and between 117 to 145 for $=\underline{C}H$- (five membered), $-\underline{C}H_2$-OH and aromatic peaks, respectively. A closer look at the $-\underline{C}H_2$-OH peak of 9-FM present in Mg-9FM-EtOH adduct, it is clear that the peak has been shifted to down field compared with pure 9-FM i.e, 64.5 ppm in Mg-9FM-EtOH compared with 62.3 ppm in pure 9-FM. This downfield shift of 2.2 ppm clearly demonstrates the coordination of $-\underline{C}H_2$-OH of 9-FM with $MgCl_2$. In other way, it confirms the formation of molecular adduct of 9-FM with $MgCl_2$.

4.4.1.4 Scanning Electron Microscope
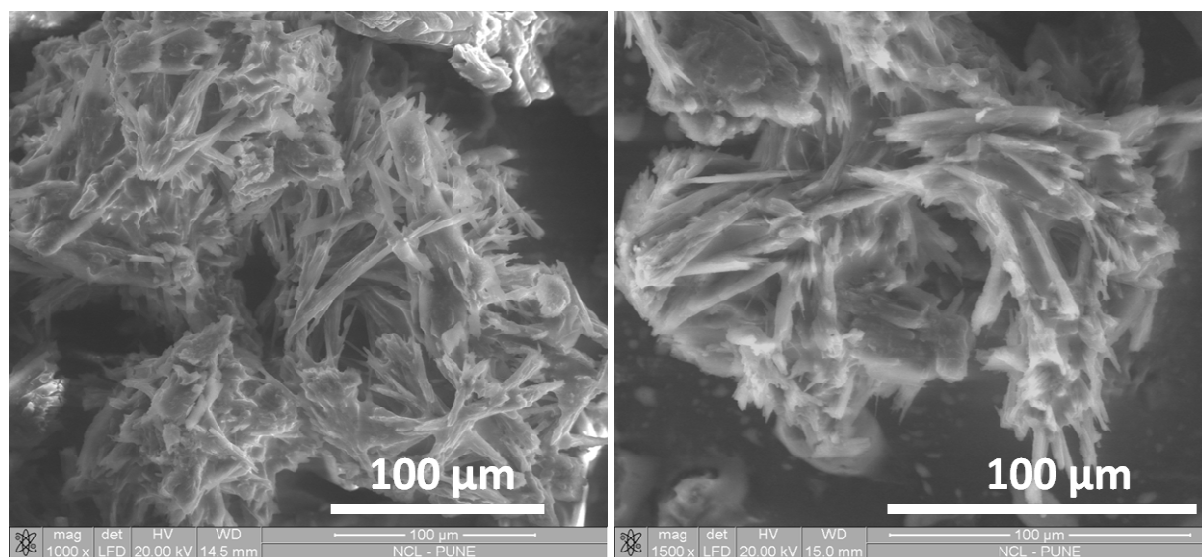
Figure 4.27: *SEM images of Mg-9FM-EtOH.*

SEM images of Mg-9FM-EtOH molecular adduct is shown in Figure 4.27. Needle like morphology was observed in this present case unlike spherical and rod shape morphologies in MgEtOH, MgMeOH and MgiBOH [26, 27]. The length of needle is approximately about 100 μm. Needle shape morphology indicates the growth of particle is unidirectional in nature. However, most of the needles were agglomerated. An increase in the

molecular size from EtOH to 9-FM alters the interaction differently with $MgCl_2$ and leads to a different morphology of adduct and catalyst.

4.4.2 Characterization of active catalyst

4.4 2.1 Synthesis of active catalyst

2.8 g of Mg-9FM-EtOH adduct was taken with 22 mL of chlorobenzene and stirred for 1 h at 110 °C. Subsequently, 22 mL of $TiCl_4$ has been added over a period of 10 min and stirred further for 1 h. Resulting solid product was washed with two 100 ml portions of $TiCl_4$. Finally, the solid catalyst was filtered and washed several times with dry hexane at 60 °C until all the physisorbed Ti-species was removed. Then, **Ti-9FM-EtOH-1** catalyst obtained has been dried under vacuum and stored in dry N_2 atmosphere. Amount of titanium content in the active catalyst was found to be 12.5 wt % (0.264 mmol).

In order to see the influence of 9FM on the polymerization activity, we have synthesized the active catalyst without washing step i.e., by simply having 9FM as internal donor on active catalyst. For comparison we have taken same amount of titanium (as found in **Ti-9FM-EtOH-1**) in this present active catalyst. Required quantity of Mg-9FM-EtOH has been taken in dry hydrocarbon solution then 12.5 % of titanium precursor ($TiCl_4$) has been added and stirred for 48 hours. Finally **Ti-9FM-EtOH-2** catalyst has been dried under vacuum and stored in dry N_2 atmosphere. Although we presume that $TiCl_4$ is incorporated in a similar way in the above catalysts, we cannot rule out the difference in the nature of $TiCl_x$ species on both the above catalysts.

4.4.2.2 Solid state NMR of active catalyst

Figure 4.28 shows the ^{13}C CPMAS NMR of active catalyst derived from Mg-9FM-EtOH. **Ti-9FM-EtOH-1** catalyst shows peak at 25.1, 44.7, 77.5 ppm and broad peak around 129 ppm. Aromatic peak around 129 ppm could be due to the presence of chlorobenzene

which has been used as a solvent for the synthesis of active catalyst as well as could be due to the contribution from 9FM moieties present in the active catalyst. Peak around 25.8 ppm confirms the presence of aliphatic hydrocarbon i.e., hexane used during the washing step in the synthesis of active catalyst. Peaks at 77.5 ppm and small broad peak around 44.7 could be due to ether or other organic moieties formed during the titanated and others harsh condition involved in the synthesis of active catalyst. In **Ti-9FM-EtOH-2** catalyst, peak at 49.5 and 68.1 ppm confirms the presence of 9-FM moieties in active catalyst. –CH_2OH feature at 68.1 ppm is shifted down field compared to 9FM and Mg-9FM-EtOH, possibly indicating a stronger interaction. Peak at 25 ppm confirms the presence of hexane used in the synthesis. Peaks between 120 to 144 ppm also evidenced the presence of 9-FM moieties in the active catalyst. Overall solid state NMR characterization confirms **Ti-9FM-EtOH-2** catalyst having 9-FM moieties as such as a integral part of active catalyst.
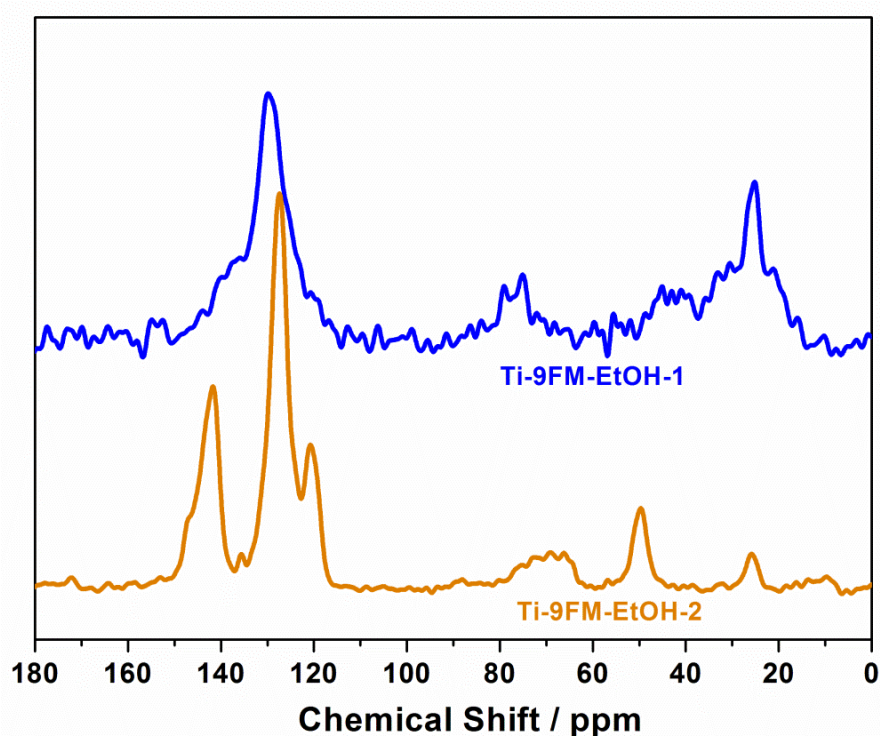
Figure 4.28: *^{13}C CPMAS NMR spectra of the titanated active catalyst.*

4.4.2.3 Thermal analysis
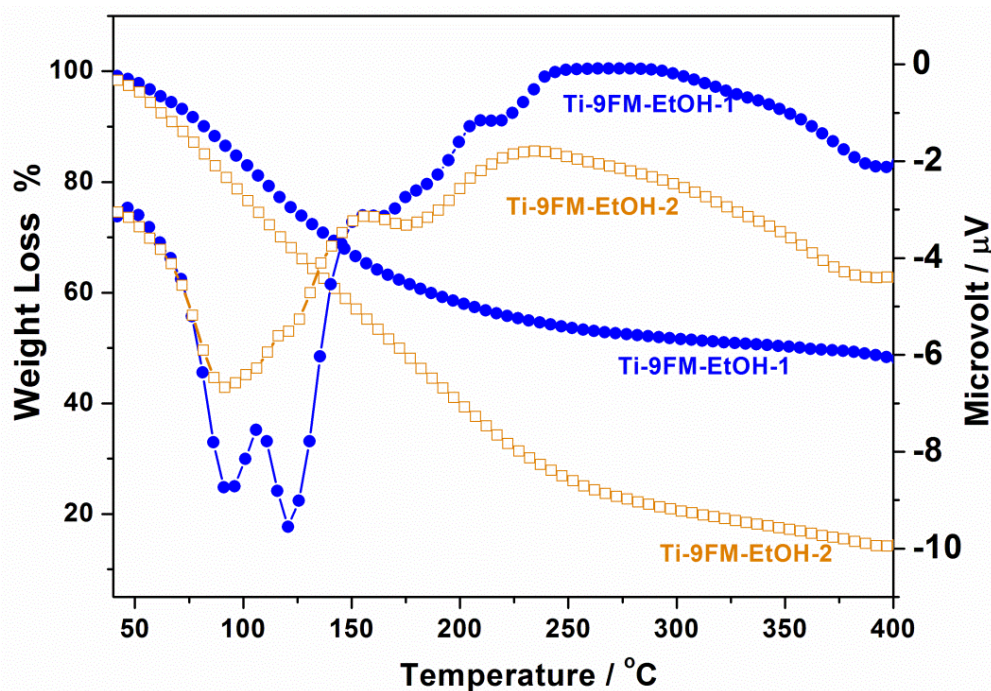
Figure 4.29: *TG-DTA analysis of active catalyst.*

TG and DTA analysis of the titanated active catalysts are shown in Figure 4.29. Among two active catalysts synthesized, significant difference in the weight loss has been observed. Catalyst prepared by conventional synthesis (**Ti-9FM-EtOH-1**) shows the weight loss of 48% compared to the weight loss of 74% for catalyst prepared by simple stirring (**Ti-9FM-EtOH-2**). Lower weight loss associated with **Ti-9FM-EtOH-1** could be due the presence of lesser organic residues. During the synthesis of active catalyst in conventional synthesis, most of the organic residues will be removed in the hexane washing step. However, in the case of **Ti-9FM-EtOH-2**, 74% weight loss indicates the presence of more organic residues in the active catalyst. Infact presence of 9-FM moieties in **Ti-9FM-EtOH-2** was evidenced by ^{13}C solid state NMR in figure 4.28. However, in the case of **Ti-9FM-EtOH-1**, catalyst contains other hydrocarbon, such as chlorobenzene and other organic residues and 9-FM moieties is unlikely to be present

4.4.2.4 Scanning Electron Microscopy
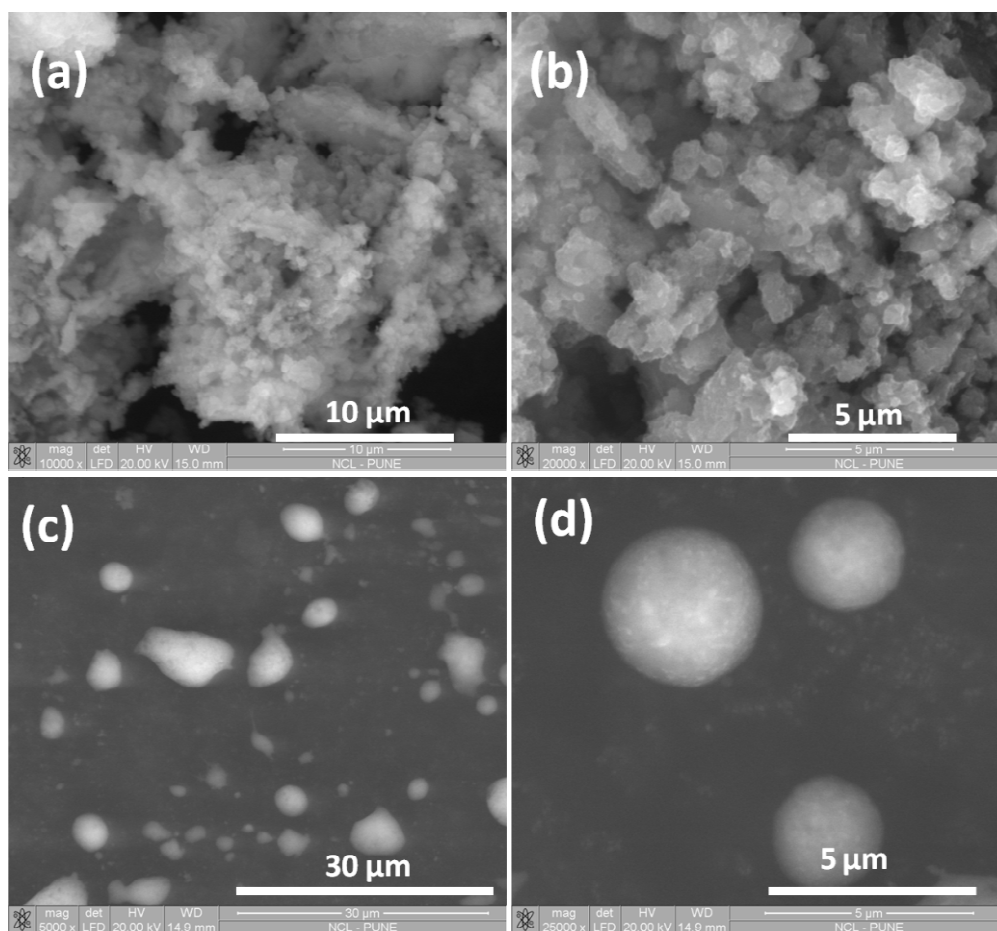
Figure 4.30: *SEM images active catalysts. (a) and (b) for **Ti-9FM-EtOH-1** and (c) and (d) for **Ti-9FM-EtOH-2**.*

Figure 4.30 shows the SEM images of the active catalyst. The images were recorded after the sonication of dispersed active catalyst in triblock copolymer and toluene solution to avoid any agglomeration and to resist the atmospheric degradation due to the air-sensitive nature of the catalyst. SEM images clearly show high porous nature of **Ti-9FM-EtOH-1**. Particle size of the active catalyst was observed below ~1 μm. **Ti-9FM-EtOH-2** catalyst exhibits spherical morphology with smooth surface. Size of the particles was measured to be between 2-5 μm. Harsh condition employed in the synthesis of **Ti-9FM-EtOH-1** could be the reason for the smaller particle size compared with **Ti-9FM-EtOH-2**.

4.4.2.5 Textural Properties

N$_2$ adsorption isotherm and pore size distribution of active catalyst is shown in Figure 4.31. Figure I and Figure II represent the isotherm and pore size distributions obtained from **Ti-9FM-EtOH-1** and **Ti-9FM-EtOH-2** catalyst, respectively. BET method was employed to calculate the surface area of active catalysts. **Ti-9FM-EtOH-1** catalyst shows a surface area of 410 m^2/g which is far higher than many commercial and other reported catalysts.

(I) Ti-9FM-EtOH-1   (II) Ti-9FM-EtOH-2
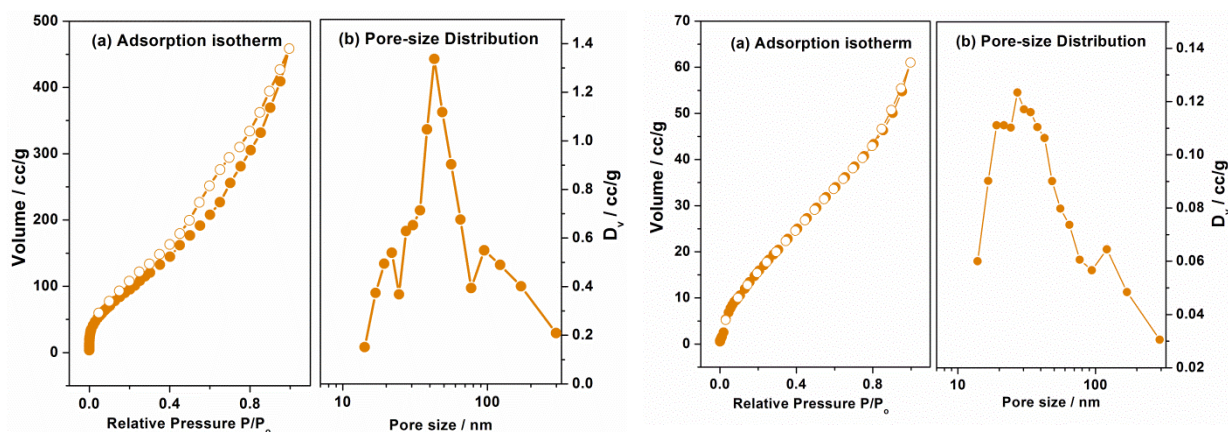
Figure 4.31*: (I) **Ti-9FM-EtOH-1** catalyst (a) Adsorption isotherm and (b) pore size distribution and (II) **Ti-9FM-EtOH-2** catalyst (a) adsorption isotherm and (b) pore size distribution*

The average pore diameter was calculated and found to be 69.2 nm with the pore volume of 0.711 cc/g. However, **Ti-9FM-EtOH-2** exhibits a surface area of 75.1 m^2/g and pore size distribution of 50.3 nm with the pore volume of 0.0946 cc/g. High surface area of **Ti-9FM-EtOH-1**compared with **Ti-9FM-EtOH-2** could be due to the removal of bulkier organic residue during the washing step in the synthesis of active catalyst. Former active catalyst shows type-IV with H3 isotherm and latter active catalyst shows type-II isotherm. **Ti-9FM-EtOH-2** catalyst having less contribution from type-III and more contribution from type-II. Macropore contribution in the active catalysts is evidenced by type-II isotherm. Infact pore

size distribution curve also shows the contribution of macropores in both active catalysts. Macropore contribution could be associated with the removal of bulky 9-FM that was present in the molecular adducts.

4.4.3. Ethylene Polymerization

Ethylene polymerization reactions have been carried out for the two active catalysts derived from Mg-9FM-EtOH. Co-catalysts with three different alkyl chains; namely, methyl, ethyl, and isobutyl (R_3Al; $R = CH_3$, $-CH_2CH_3$, and $-CH_2CH(CH_3)_2$) have been used to activate the catalytic active sites present in the catalysts. For each cocatalyst, reactions were carried out at 5 atm pressure and 75 ^{o}C. Average results were taken after carrying out three sets of polymerizations for each condition. Activity results are shown in Table 4.5. (1) Overall polymerization activity of **Ti-9FM-EtOH-1** catalyst is higher than **Ti-9FM-EtOH-2**. (2) Among the ethylene polymerization reactions, entry 3 shows best activity of Ti-9FM-EtOH-1 when iBu$_3$Al was used as co-catalyst. This activity is ~4.5 times higher than the commercial Z-N catalyst (entry **7**). (3) Overall MWD of polymer obtained by using **Ti-9FM-EtOH-1** was better than **Ti-9FM-EtOH-2** and entry 6 shows the lowest MWD of polyethylene among all the polymers obtained. Overall higher activity of **Ti-9FM-EtOH-1** catalyst could be due to the higher surface area (410 m^2/g) compared with **Ti-9FM-EtOH-2** (surface area of 75 m^2/g). The highest polymerization activity for the combination of **Ti-9FM-EtOH-1** with iBu$_3$Al could be due the porous nature associated with active catalyst and macropores (69.2 nm) found in it is likely to contribute to the activity. This bigger pore and comparatively lower lability of iBu$_3$Al (compared with other alkyl aluminium used) might have influenced the reduction of TiCl$_x$ species in the pores of the active catalyst to Ti^{3+} and thereby lead to the highest activity. Overall lower MWD of PE for **Ti-9FM-EtOH-2** catalyst

Table 4.5: *Activity results of catalysts for polymerization reactions.*

No	Catalyst	Ti wt% (mmol)	Cocatalyst	Condition	Productivity of PE (gg^{-1} of catalyst)	Productivity of PE (gmmol^{-1} of Ti)	Mn (Mw) gmol^{-1}	MWD
1	Ti-9FM-EtOH-1	12.5 (0.264)	Me$_3$Al	75°C, 5atm	2685	1017.0	17196 (166809)	9.7
2	Ti-9FM-EtOH-1	12.5 (0.264)	Et$_3$Al	75°C, 5atm	4841	1833.7	14451 (154631	10.7
3	Ti-9FM-EtOH-1	12.5 (0.264)	iBu$_3$Al	75°C, 5atm	5813	2201	237681 (237681)	12.3
4	Ti-9FM-EtOH-2	12.5 (0.264)	Me$_3$Al	75°C, 5atm	1870	26051	26723 (187570)	7.2
5	Ti-9FM-EtOH-2	12.5 (0.264)	Et$_3$Al	75°C, 5atm	3303	1251.5	20057 (150430)	7.5
6	Ti-9FM-EtOH-2	12.5 (0.264)	iBu$_3$Al	75°C, 5atm	2356	892.4	33696 (215660)	6.4
7	Ti-MgEtOH[26]	11 (0.23)	Et$_3$Al	75°C, 5atm	1300	572	22173 (255010)	11.5

derived could be due the influence of 9-FM as internal donor present in the active catalyst. Presence of higher amount of 9-FM in **Ti-9FM-EtOH-2** is evident from NMR and TGA. Lowest MWD of **Ti-9FM-EtOH-2** with iBu$_3$Al could be again due lower lability as well as the presence of 9-FM internal donor in the surface of catalyst

4.4.4. Conclusion

Mg-9FM-EtOH molecular adduct has been synthesized and subjected to detailed spectroscopic and structural investigations. In order to see the effect of 9-FM molecule as an internal donor, active catalyst have been synthesized by conventional and merely fixing TiCl$_4$ over the support; both the above catalysts were subjected to detailed investigations. The textural properties of the active catalysts shows higher surface area for conventional synthesized catalyst than the other one. Ethylene polymerization reactions were carried with different co-catalyst and shows iBu$_3$Al as best cocatalyst for the above supported Z-N catalytic system. Polymerization activity results suggests conventionally synthesized catalyst exhibit ~4.5 times better activity than commercial Z-N catalyst, and still better than merely TiCl$_4$ fixed over the Mg-9FM-EtOH support. However, the latter catalytic system shows lowest MWD of PE obtained confirms the role of 9-FM as internal donor in the catalytic system. Detailed studies confirm the less lability of iBu$_3$Al and contribution of macropores are the reason for the conventionally synthesized catalyst to give higher polymerization activity.

4.5 Reference:

1. (a) Ziegler, K.; Gellert, H. G.; Zosel, K.; Lehmkuhl, W.; Pfohl, W. Angew. Chem 1955, 76, 424. (b) Ziegler, K.; Holzkamp, E.; Breil, H.; Martin, H. *Angew Chem.* **1955,** *67*, 541. (c) Natta, G. *J Polym Sci*. **1955,** *16,* 143. (d) Kashiwa, N.; Fujimura, H.; Tokuzumi, Y. JP Patent 1031698 (application in Japan on Aug 1, 1968). (d) Kashiwa, N. *Polym. J*. **1980,** *12,* 603. (e) Kashiwa, N.; Yoshitake, J. *Makromol Chem*

Rapid Commun. **1982,** *3,* 211. (f) Kashiwa, N.; Yoshitake, J. *Markromol Chem Rapid Commun*. **1983,** *4,* 41.

2. (a) Albizzati, E.; Cecchin, G.; Chadwick, J. C.; Collina, G.; Giannini, U,; Morini, G.; Noristi L. In Polypropylene Handbook Pasquini, N. Ed.; Hanser: Munich, Germany, 2005; pp 11. (b) Cecchin, G.; Morini, G.; Pelliconi, A. *Macromol Symp.* **2001,** *173,* 196.

3. Albizzati, E.; Galimberti, M. *Catal. Today.* **1998,** *41*, 159.

4. Sobota, P.; Płuziński, T.; Utko, J.; Lis, T. *Inorg. Chem.* **1989,** *28,* 2217.

5. (a) Yang, C. B.; Hsu, C. C. *Polym. Bull.* **1993,** *30,* 529. (b) Liu, B.; Nitta, T.; Nakatani, H.; Terano, M. *Macromol. Chem. Phys.* **2003,** *204*, 395.

6. Vanka, K.; Singh, G.; Iyer, D.; Gupta, V. K. *J. Phys. Chem. C* **2010,** *114,* 15771.

7. Soga, K.; Shiono, T. *Prog. Polym. Sci.* **1997,** *22,* 1503.

8. Arzoumanidis, G. G.; Karayannis, N. M. *CHEMTECH*. **1993,** *23,* 43.

9. Haung, R.; Malizia, F.; Pennini, G.; Koning, C. E.; Chadwick, J. C. *Macromol. Rapid Commun.* **2008,** 29.

10. Kim, S. H.; Somorjai, G. A. *J. Phys. Chem. B* **2002,** *106,* 1386.

11. Sobota, P. *Coord. Chem. Rev.* **2004,** *248,* 1047.

12. Andoni, A.; Chadwick, J. C.; Milani, S.; Niemantsverdriet, J. W.;Thüne, P. *J. Catal.* **2007,** *247,* 129.

13. Busico, V.; Causa, M.; Cipullo, R.; Credendino, R.; Cutillo, F.; Lamanna, R.; Segre, A.; Castelli, V. V. A. *J. Phys. Chem. C* **2008,** *112,* 1081.

14. Thushara, K. S.; Mathew, R.; Ajithkumar, T. G.; Rajamohanan, P. R.; Bhaduri, S.; Gopinath, C. S. *J. Phys. Chem. C* **2009,** *113,* 8556.

15. Lee, M. Y.; Scott, S. L. *Chem.Eur. J.* **2011,** *17,* 4632.

1. (a) Seenivasan, K.; Sommazzi, A.; Bonino, F.; Bordiga, S.; Groppo, E. *Chem.Eur. J.* **2011,** *17,* 8648. (b) Groppo, E.; Seenivasan, K.;Barzan, C. *Catal. Sci. Technol.,* **2013,** *3*, 858.

16. (a) Magni, E.; Somorjai, G. A. *Surf. Sci.* **1996,** *345,* 1. (b) Kim, S. H.; Craig, R. T.; Somorjai, G. A. *Langmuir* **2000,** *16,* 9414.

17. Mori, H.; Hasebe, K.; Terano, M. *Macromol. Chem. Phys.* **1998,***199,* 2709.

18. Kim, S. H.; Craig, R. T.; Somorjai, G. A. *Langmuir* **2000,** *16,* 9414.

19. Boero, M.; Parrinello, M.; Terakura, K. *J. Am. Chem. Soc.* **1998,***120,* 2746.

20. Puhakka, E.; Pakkanen, T. T.; Pakkanen, T. A. *J. Phys. Chem. A* **1997,** *101,* 6063.

21. Noto, V. D.; Bresadola, S.; Zannetti, R.; Viviani, M. *Z. Kristallogr.* **1993,** *204,* 263.

22. Valle, G.; Baruzzi, G.; Paganetto, G.; Depaoli, G.; Zannetti, R.; Marigo, R. *Inorg. Chim. Acta* **1989,** *156,* 157.

23. Sozzani, P.; Bracco, S.; Comotti, A.; Simonutti, R.; Camurati, I. *J. Am. Chem. Soc.* **2003,** *125,* 12881.

24. Malizia, F.; Fait, A.; Cruciani, G. *Chem. Eur. J.* **2011,** *17,* 13892.

25. Thushara, K. S.; Gnanakumar, E. S.; Mathew, R.; Jha, R. K.; Ajithkumar, T. G.; Rajamohanan, P. R.; Sarma, K.; Padmanabhan, S.; Bhaduri, S.; Gopinath, C. S. *J. Phys. Chem. C* **2011,** *115,* 1952.

26. (a) Gnanakumar, E. S.; Thushara, K. S.; Bhange, D. S.; Mathew, R.; Ajithkumar, T. G.; Rajamohanan, P. R.; Bhaduri, S.; Gopinath, C. S. *Dalton Trans. 2011,* **40,** 10936. (b) Thushara, K. S.; Gnanakumar, E. S.; Mathew, R.; Ajithkumar, T. G.; Rajamohanan, P. R.; Bhaduri, S.; Gopinath, C. S. *Dalton Trans.* **2012,** *41,* 11311. (c) Gnanakumar, E. S.; Thushara, K. S.; Gowda, R. R.; Raman, S. K.; Ajithkumar, T. G.; Rajamohanan, P. R.; Chakraborty, D.; Gopinath, C. S. *J. Phys. Chem. C*. **2012,** *116,* 24115. (d) Gnanakumar, E. S Gowda, R. R.; Srikanth,K; S. K.; Ajithkumar, T. G.; Rajamohanan, P. R.; Chakraborty, D.; Gopinath, C. S. *ACS Catal.* **2013,** *3,* 303.

27. Noto, V. D.; Zannetti, R.; Viviani, M.; Marega, C.; Marigo, A.; Bresadola, S. *Makromol. Chem.* **1992,** *193,* 1653.

28. Tewell, C. R.; Malizia, F.; Ager, J. W., III; Somorjai, G. A. *J. Phys. Chem. B* **2002,** *106,* 2946.

29. Neelakantan, P. *Proc. Ind. Acad. Sci.* **1963,** *57,* 94.

30. Auriemma., F.; De Rosa, C. *Chem. Mater*. **2007,** *19,* 5803.

31. Ronkko, H. L.; Knuutilla, H.; Denifl, P.; Leinonen, T.; Venalainen, T. *J. Mol. Catal. A: Chem.* **2007,** *278,* 127.

32. (a) Sreeja, V.; Smitha, T. S.; Nand, D.; Ajit Kumar, T. G.; Joy, P. A. *J. Phys. Chem. C* **2008,** *112,* 14737. (b) Mathew, T.; Sivaranjani, K.; Gnanakumar, E. S.; Yamada, Y.; Kobayashi, T.; Gopinath, C. S. *J. Mater. Chem.* **2012,** *22,* 13484.

33. (a) Basu, S.; Mapa, M.; Gopinath, C. S.; Doble, M.; Bhaduri, S.; Lahiri, G. K. *J. Catal.* **2006,** *239,* 154. (b) Kulkarni, D. G.; Vadivel Murugan, A.; Viswanath, A. K.; Gopinath, C. S. *J. Nanosci. Nanotechnol.* **2009,** *9,* 371. (c) Waghmode, S. B.; Vetrivel, R.; Hegde, S. G.; Gopinath, C. S.; Sivasanker, S. *J. Phys. Chem. B* **2003,** *107,* 8517.

34. Sobota, P.; Szafert, S. *Dalton Trans*. **2001,** 1379

35. Bart, J. C. *J. Mater. Sci.,* **1995,** *30,* 2809.

36. Evans, J. C. *Spectrochim. Acta,* **1961,** *17,* 129.

37. Bhaduri, S.; Gupta, V. K.U.S. Patent 6841633, **2005,** and references therein.

38. Xu, R.; Liu, D.; Wang, S.; Mao, R. *Macromol. Chem. Phys.,* **2006,** *207,* 779

39. Jamjah, R.; Zohuri, G. H.; Vaezi, J.; Ahmadio, S. Nekomanesh, M.; Pouryari, M. *J. Appl. Polym. Sci.,* **2006,** *101,* 3830.

40. Dil, E. J.; Pourmahdian, S.; Vatankhah, M.; Taromi, F. A. *Polym. Bull.,* **2010,** *64,* 445.

41. Andoni, A.; Chadwick, J. C. ; Niemantsverdriet, J.W.; Th¨une, P. C. *J. Catal.,* **2008,** *257,* 81.

42. Busico, V.; Corradini, P.; De Martino, L.; Proto, A.; Savino, V.; Albizzati, E. *Makromol. Chem.,* **1985,** *186,* 1279.

43. (a) Gholap, S.; Badiger, M. V.; Gopinath, C. S. *J. Phys. Chem. B,* **2005,** *109,* 13941; (b) Mathew, T.; Shylesh, S.; Devassy, B. M.; Satyanarayana, C. V. V.; Rao, B. S; Gopinath, C. S. *Appl. Catal., A,* **2004,** *273,* 35; (c) Velu, S. ; Suzuki, K.; Gopinath, C. S.; Hattori, T. ; Yoshida, H. *Phys. Chem. Chem. Phys.,* **2002,** *4,* 1990; (d) Mathew, T. ; Tope, B. B.; Shiju, N. R.; Hegde, S. G.; Rao B. S.; Gopinath, C. S. *Phys. Chem. Chem. Phys.,* **2002,** *4,* 4260. (e) Shiju, N. R. ; Anilkumar, M.; Mirajkar, S. P.; Gopinath, C. S.; Satyanarayana, C. V. ; Rao, B. S. *J. Catal.,* **2005,** *230,* 484.

Chapter 5

Ether and Bifunctional Molecular Adduct of MgCl$_2$ and Its Structural Studies

Part A:MgCl$_2$.xTHF (x = 1.5, 2 and 4)

5.1 Introduction

Latest generation of MgCl$_2$/TiCl$_4$ Z-N catalyst have the advantage of using lowest amount of titanium and alkyl aluminium compound with very good control in polymer morphology and thereby tune the properties of polymer [1, 2]. Added to the benefit, current heterogeneous Z-N catalytic system reached its high mileage by excellent polymerization performance which allows economic and versatile advantages in commercial industrial processes [2, 3]. Unfortunately, the above catalytic systems are multisite in nature, in spite of its major production role in polymer industries [4-9]. Third component i.e., Lewis base is indispensable to improve the activity and stereoselectivity as well. Lewis base can be added in the catalyst preparation (internal donor) or during the polymerization (external donor). Combining both internal-external donor pair can increase the activity and stereoselectivity of the catalytic system and also fine tune the polymer properties [10-13].

Although heterogeneous Z-N catalyst in the industrial production of polyolefin crossed more than 60 years jubilant journey and there are thousands of research investigations on this catalytic system, many aspects of understanding at molecular level of the above catalytic systems are remaining unclear [3, 8, 14-17]. Complex nature of the multi component system made the system to become more complicated to understand thoroughly. Many interactions like MgCl$_2$-TiCl$_4$, TiCl$_4$-Lewis base and MgCl$_2$-Lewis base can affect the performance of and composition of the heterogeneous Z-N catalyst [4, 5]. Different crystallographic planes exposed on MgCl$_2$ surface containing TiCl$_4$ influences polymerization activity of the catalyst. Many models have been proposed to explain the role of Lewis base on the stereospecificity in polymerization activity such as poisoning of aspecific sites and chemical and steric modification over the isospecific sites to control the

alkene insertion. However, the precise mechanism by which the Lewis base operating in heterogeneous Z-N catalysis is still unclear [18, 19].

Most commonly used Lewis base in the industrial heterogeneous Z-N catalyst is alcohol and ether, specifically EtOH and THF, respectively [3,20-22]. Addition of the above mentioned Lewis base coordinate with $MgCl_2$ and modifies (a) electronic structure of the support (b) enhances the poor solubility of the support, (c) alters the molecular structure and thereby influence polymerization activity of the catalyst [7]. Many reports have been published with the detailed studies of Z-N catalytic system using EtOH as Lewis base especially the structure of $MgCl_2.xEtOH$. However, till today detailed studies on different stoichiometries of $MgCl_2.xTHF$ molecular adduct and its polymerization activity has not been reported so far.

After the report of $[Mg_2(\mu-Cl)_3(THF)_6][TiCl_5(THF)]$ structure between the THF adduct and $TiCl_4$ by Sobota et al., on 1984 [23], researchers found these adducts derived from THF are not merely a support, but Cl^- donor and is a highly reactive species [22]. It is reported in literature that, THF forms adduct with $MgCl_2$ in three different stoichiometries namely $MgCl_2.1.5THF$, $MgCl_2.2THF$ and $MgCl_2.4THF$ [23-29]. Few of the stoichiometries of THF adduct namely $MgCl_2.1.5THF$ and $MgCl_2.2THF$ have been used extensively by many industries [23-29]. Although these heterogeneous supports have practical applications, they have not been studied sufficiently. Much information in the literature is available on binary system $TiCl_4-THF$ and ternary system $TiCl_4-THF-MgCl_2$ [16, 23, 30]. Nonetheless, $MgCl_2$-THF system has not been well studied till now. The present chapter has been divided into **Part A** and **Part B. Part A** deals with synthesis and detailed structural study of different stoichiometries of $MgCl_2.xTHF$ molecular adducts and its application in ethylene polymerization using different Ti/Mg ratios.

As a result of many efforts to improve the efficiency of the catalytic system, recent generation of heterogeneous Z-N catalysts contain multidentate Lewis base, such as diethers or diesters as donors [31, 32]. Typical bidendate ligand binds much stronger to the surface of the support than Ti active sites. Many reports have been published by Sobota et al., on alkoxy ligand as bidendate ligand to form complex with magnesium and titanium. These complexes exhibit better polymerization activity that the earlier generation Z-N catalysts [7, 33-36]. Keeping above literature in mind, tetrafurfuryl alcohol (THFA) as a Lewis base has been used to form molecular adduct with MgCl$_2$. Detailed structural studies of the above molecular adduct and the influence of Ti/Mg ratio on ethylene polymerization activity is dealt in **Part B**.

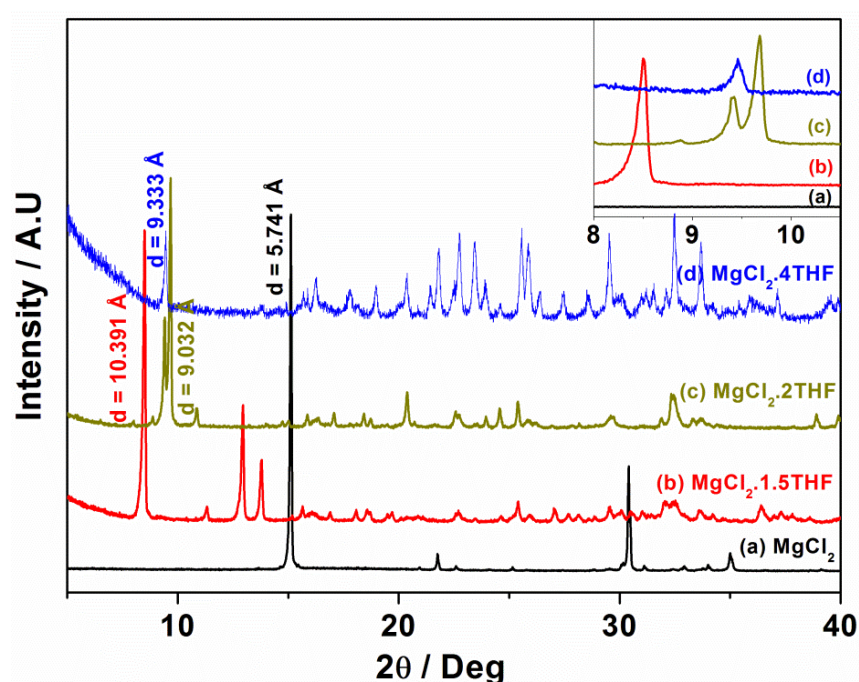## 5.2. Results and Discussion

5.2.1 Powder X-ray diffraction

Figure 5.1. Powder XRD pattern of (a) anhydrous MgCl$_2$, (b) MgCl$_2$.1.5THF, (c) MgCl$_2$.2THF and (d) MgCl$_2$.4THF adduct.

Synthesis details of MgCl$_2$.xTHF have been given in detail in sectoin 2.1.1.7, Chapter-2. PXRD pattern of MgCl$_2$ and different stoichiometries of THF adduct of MgCl$_2$ is shown in Figure 5.1. Three different stoichiometries of MgCl$_2$.xTHF adduct shows many number of diffraction peaks clearly indicates the structure with low symmetry [26, 16, 22]. Although the structure of MgCl$_2$.4THF and MgCl$_2$.2THF is reported in the literature, PXRD aspects of adducts was not discussed in detail about the structure of the molecular adducts. PXRD of molecular adducts differ in the magnitude of the diffraction angle as well as the intensities of the lines. These diffractions are entirely different from anhydrous MgCl$_2$ diffraction pattern. All the three MgCl$_2$.xTHF molecular adducts shows d (001) value higher than d (003), value of MgCl$_2$ confirm the adduct formation of ether molecule with MgCl$_2$. Due the adduct formation, the distance between the -Cl-Mg-Cl- triple layer has been increased and hence (001) interplanar d-values are higher than MgCl$_2$. The above points prove the chemical individuality of the molecular adducts synthesized.

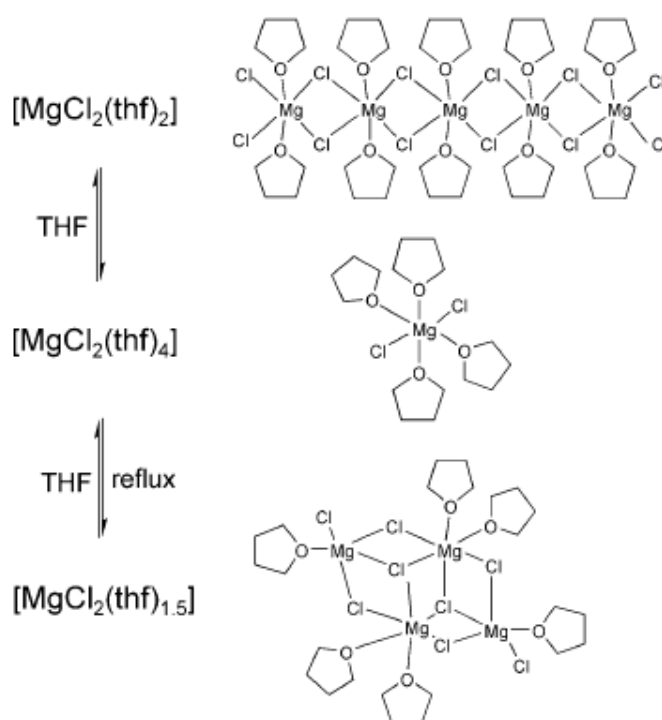**Figure 5.2.** Equilibrium between THF and MgCl$_2$ with different molecular structures [22].
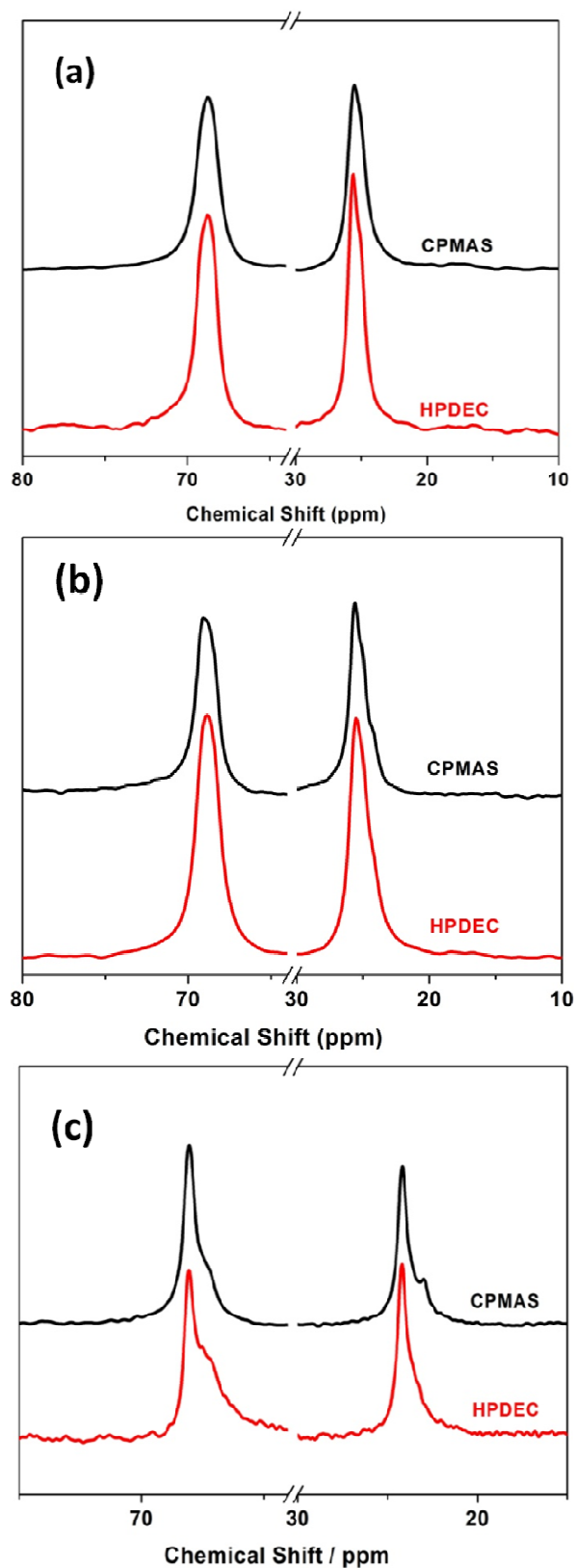
5.2.2 Solid state NMR

Figure 5.3. ^{13}C *CPMAS 75.5 MHz and HPDEC NMR spectra of (a) MgCl$_2$.4THF, (b) MgCl$_2$.2THF and (c) MgCl$_2$.1.5THF adducts.*

Sobota et al., studied the influence of coordination ability of THF and the adduct formation with $MgCl_2$. There is equilibrium present between different molecular adducts formed during the reaction. In this equilibrium linear structure of $MgCl_2.2THF$ adduct is in equilibrium with $MgCl_2.1.5THF$ and $MgCl_2.4THF$. Commonly used industrial heterogeneous Z-N catalysts are derived from $MgCl_2.1.5THF$ and $MgCl_2.2THF$ adducts as a active support. Figure 5.2 show the equilibrium between the different structures of $MgCl_2.xTHF$ molecular adducts [22].

Figure 5.3 shows the ^{13}C CP MAS and HPDEC solid state NMR spectra of $MgCl_2.xTHF$ adducts. $MgCl_2.4THF$ and $MgCl_2.2THF$ molecular adducts shows two peaks at 68.7 and 25.5 ppm in ^{13}C CPMAS and HPDEC solid state NMR spectra (Figure 5.3 (a) and (b)). Pure THF molecule also shows only two signals in ^{13}C NMR spectra. Therefore, the above observation suggests the presence of single type of THF molecule both molecular adducts. The peaks could be assigned to –$\underline{C}H_2$- attached with oxygen is at 68.7 and –$\underline{C}H_2$- attached with carbon is at 25.5 ppm. Absence of any extra peak in ^{13}C HPDEC signifies that all the THF molecules are strongly interacts with $MgCl_2$; in other words, there is no free THF molecules present in the adduct. Above observation of ^{13}C NMR spectrum demonstrates that THF molecules present in $MgCl_2.2THF$ and $MgCl_2.4THF$ are magnetically equivalent in the molecular adducts. Proposed structures of $MgCl_2.2THF$ and $MgCl_2.4THF$ molecular adducts shown in Figure 5.2 are well supported by the above NMR data. Figure 5.3 (c) shows the ^{13}C CP MAS and HPDEC spectra of $MgCl_2.1.5THF$ molecular adduct. ^{13}C CP MAS spectrum shows four peaks at 68.1, 67.3, 24.2 and 22.9 ppm. Four peaks of $MgCl_2.1.5THF$ adduct indicates two sets of magnetically non-equivalent THF molecules are present. Infact, HPDEC also confirms the absence of extra peak thereby ruling out the free THF molecules in $MgCl_2.1.5THF$ adduct structure. Proposed model structure (Figure 5.2) indicates two kinds of

THF molecules within it. NMR studies confirms the fact that, synthesized molecular adduct exhibit the same structure of the proposed molecular adduct structure.

5.2.3 Thermal Analysis
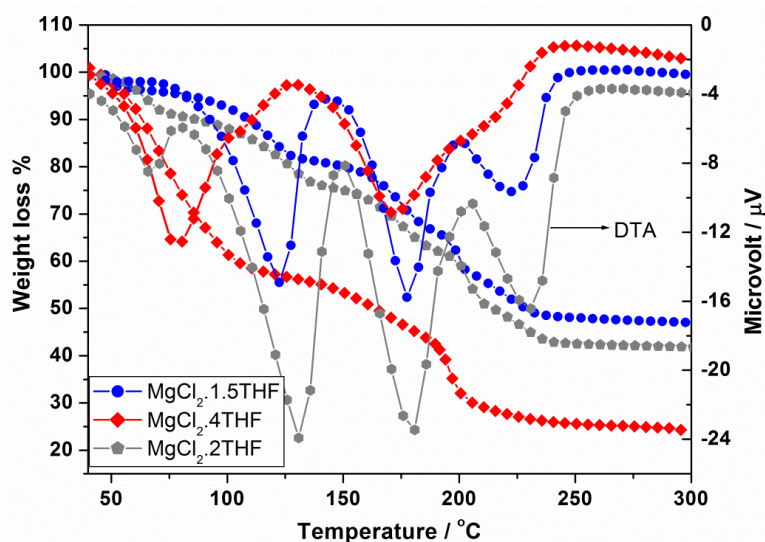
Figure 5.4: *Thermal analysis of MgCl2.xTHF adduct (x = 1.5, 2, 4)*

TG-DTA analysis of $MgCl_2.xTHF$ adduct is shown in Figure 5.4. All adducts show well defined stepwise weight loss indicates the successive removal of THF molecules from the molecular adduct like MgEtOH and MgMeOH adduct [37]. $MgCl_2.1.5THF$ adduct showing the weight loss of 47.3%, $MgCl_2.2THF$ adduct is 41.6% and $MgCl_2.4THF$ adduct having the weight loss of 25.1% in TGA analysis. $MgCl_2.4THF$ adduct showing two stepwise weight loss might be due to two successive desorption of THF molecule from the adduct. Since four molecules are present in the similar environment with trans position only two stepwise weight loss is observed. Similarly, $MgCl_2.2THF$ adduct also showing two step weight loss in TGA profile indicates two THF molecules are present in trans position similar to the former adduct. But in the case of $MgCl_2.1.5THF$ adduct, three stepwise desorption observed. This could be due to complex bridged structure present in the molecular structure. Due to the complex structure, during the desorption complex dynamic change of THF molecue around Mg^{2+} might have present and thereby leads to three successive desorption of

THF molecule. Experimental and theoretical comparison of weight loss observed for the molecular adduct is well matching within ±1 error. The above thermal analysis confirmed that individual molecular adduct of $MgCl_2.xTHF$ (x = 1.5, 2 and 4) have been synthesized.
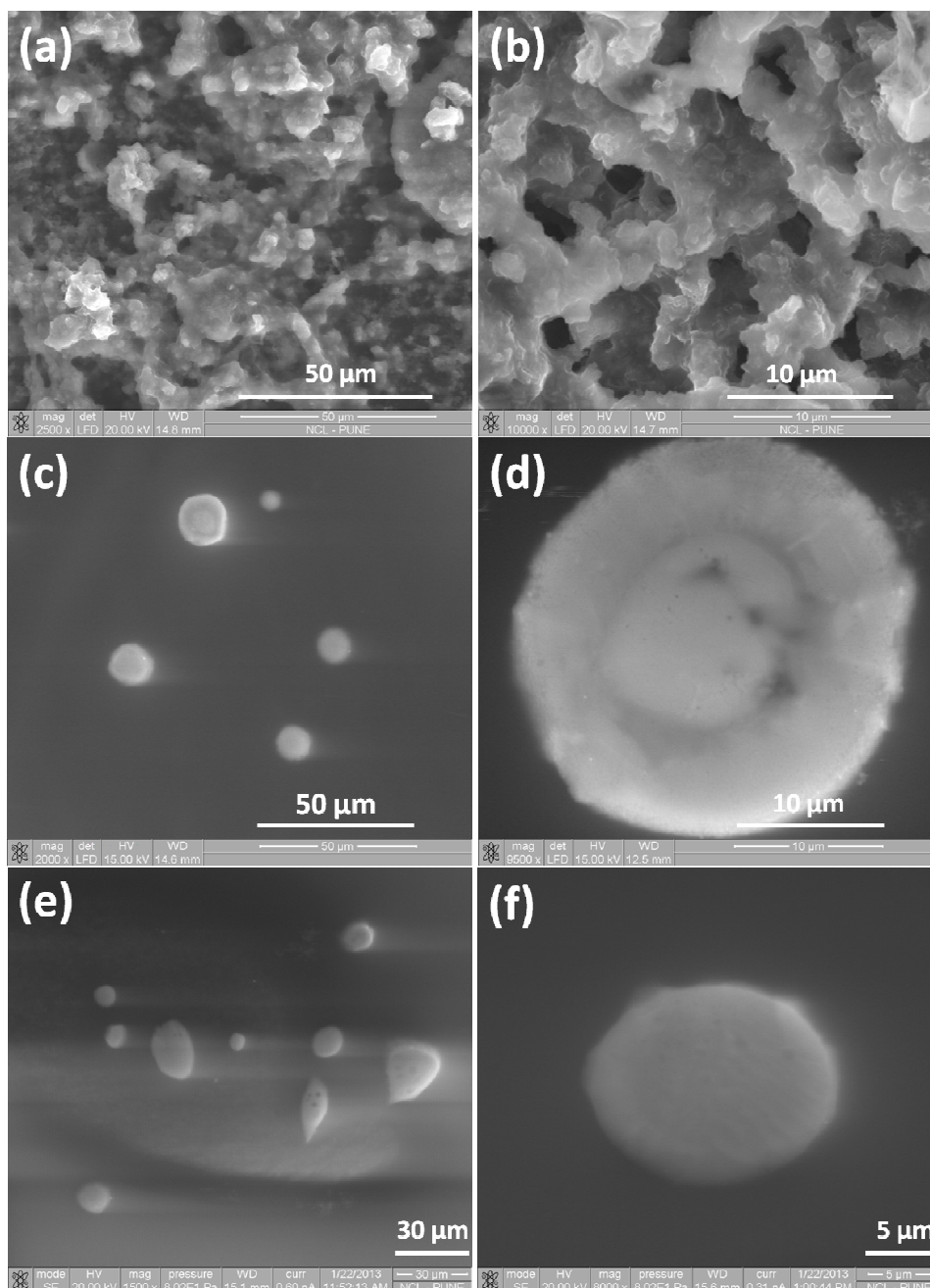
5.2.4 Scanning Electron Microscopy

Figure 5.5: *SEM images of (a) and (b) $MgCl_2.1.5THF$, (c) and (d) $MgCl_2.2THF$, (e) and (f) $MgCl_2.4THF$ adduct.*

Figure 5.5 shows SEM images of $MgCl_2.xTHF$ molecular adducts. Like other molecular adducts, SEM images have been recorded using tri-blockcopolymer solution. It evidence from the above figure, that the morphology and particle size of the molecular adduct is highly dependent on the stoichiometry of the molecular adduct. $MgCl_2.1.5THF$ adduct shows (Figure 5.5 (a) and (b)) porous morphology with agglomerated spherical particles. Sizes of the particles are in few tens of μm in range. $MgCl_2.2THF$ adduct (Figure 5.5 (c) and (d)) exhibits spherical shape with a good inner circle boundary like core shell morphology. Sizes of the particles are 20-30μm. The surface of the particles is slightly porous in nature with associated roughness. Nonetheless, in the case of $MgCl_2.4THF$ adduct, the shape of the particles are not spherical. The size of the particles is 10-50μm in the range. And the surface of the particles is smoother in nature. Overall, the morphology of the molecular adduct is varies with the stoichiometry of the molecular adduct synthesized.

5.2.5 Ethylene Polymerization

The synthesized molecular adduct $MgCl_2.xTHF$ have been titanated with $TiCl_4$ to four different Mg/Ti ratio. Ethylene polymerization reactions have been carried out using Et_3Al as cocatalyst and the activity data is reported in Table 5.1. Results shown is the average of data collected from three different batches of catalysts in three activity measurements. Activity of the catalysts varies with the stoichiometry of the molecular adducts used. Ratios of Mg/Ti also have a great influence on ethylene polymerization in the particular stoichiometry of the molecular adduct. Figure 5.6 shows the PE production results of the active catalysts as a function of Ti-content dependence. Among three stoichiometries of the molecular adduct, $MgCl_2.1.5THF$ support gives the highest activity (**entry 3**) of 6.68 kg of PE with titanium content of 10%. Highest Ti% containing catalyst yields lower production of PE in all different stoichiometries of molecular adducts. In Ziegler catalysts, partial reduction of the catalytically active $Ti^{4+/3+}$ to Ti^{2+} in a side reaction with TEAL is known to be one of the

main catalyst deactivation pathways. With higher Ti% catalyst, more exposure of active species leads to over reduction of $Ti^{4+/3+}$ which could leads to the lowering of polymerization activity. Overall, $MgCl_2.4THF$ support derived catalysts shows lower PE production, even with different Mg/Ti ratios, which restrict the use of the above molecular adduct in the industrial production of PE. From the polymerization results, $MgCl_2.1.5THF$ and $MgCl_2.2THF$ molecular adducts are desirable candidate for better polymerization activity using optimum (10%) Ti content.
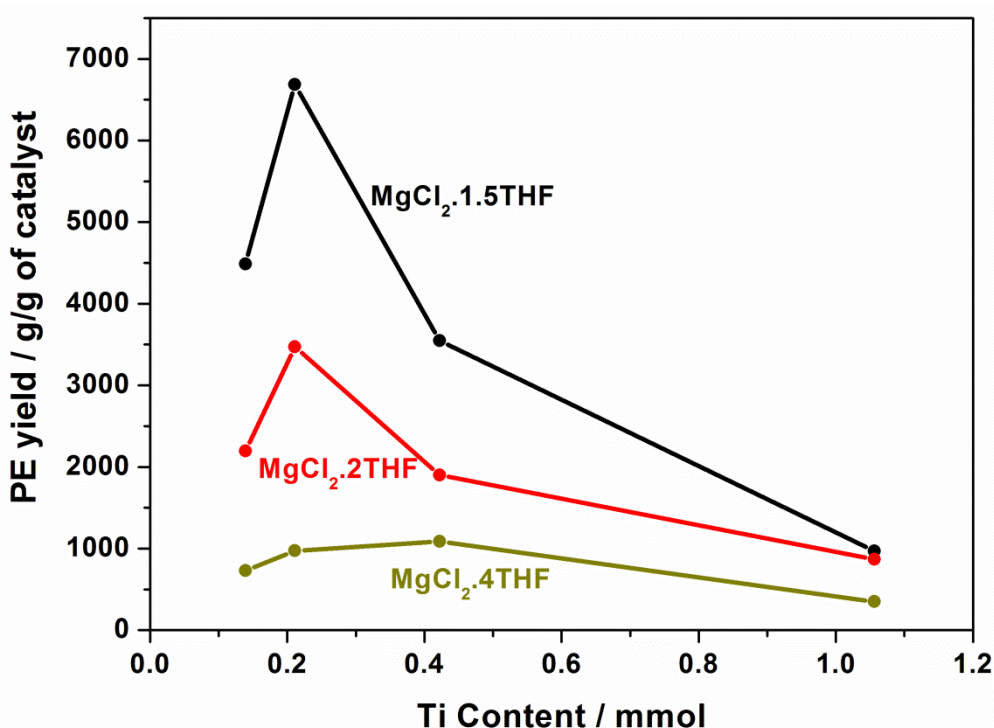
Figure 5.6*: Ti-content dependence of ethylene polymerization activity results of active catalysts derived using MgCl$_2$.xTHF molecular adducts.*

Ti content less than 10% (6.6%) leads to lower PE yield with any $MgCl_2.xTHF$ composition, indicates the necessity of Ti-content around 10-11%. Nonetheless, even with 6.6 % Ti content, $MgCl_2.1.5THF$ shows higher activity than the other two adduct compositions. It is also to be noted that the best MWD is achieved with 10% Ti content with $MgCl_2.1.5THF$. I

Table 5.1: *Ethylene polymerization results using active catalysts derived from MgCl$_2$.xTHF support.*

S.No	Support	Mg/Ti	Ti% (mmol)	Surface area m^2/g	PE Yield g/g of catalyst	Mw gmol^{-1}	MWD
1	MgCl$_2$.1.5THF	2/1	50 (1.056)	78	970	159903	7.9
2	MgCl$_2$.1.5THF	5/1	20 (0.422)	67	3548	210382	8.7
3	MgCl$_2$.1.5THF	10/1	10 (0.211)	69	6686	239872	5.9
4	MgCl$_2$.1.5THF	15/1	6.6 (0.139)	58	4489	287902	8.7
5	MgCl$_2$.2THF	2/1	50 (1.056)	47	870	120879	10.4
6	MgCl$_2$.2THF	5/1	20 (0.422)	67	1902	145003	11.7
7	MgCl$_2$.2THF	10/1	10 (0.211)	54	3473	135980	12.6
8	MgCl$_2$.2THF	15/1	6.6 (0.139)	49	2197	246083	8.9
9	MgCl$_2$.4THF	2/1	50 (1.056)	28	350	240087	15.4
10	MgCl$_2$.4THF	5/1	20 (0.422)	43	1087	178600	13.5
11	MgCl$_2$.4THF	10/1	10 (0.211)	35	973	150850	16.4
12	MgCl$_2$.4THF	15/1	6.6 (0.139)	49	729	132076	13.7

Catalyst quantity=0.1g; Al/Ti=200; Hexane = 500 ml; Temperature = 75°C; Pressure = 5 atm

is speculated that this particular composition may have the right combination of Ti and Et$_3$Al with maximum Ti^{3+}/Ti^{2+} content.

5.2.6 Conclusion

Three different stoichiometries of MgCl$_2$.xTHF (x = 1.5, 2, 4) molecular adducts have been synthesized by simple procedure using different ratios of MgCl$_2$ and THF. Synthesized molecular adduct have been characterized using different physico-chemical characterization methods. Solid state NMR demonstrates the structure of the each molecular adduct is the same as that of proposed structure using different metal precursor. Thermal analysis data also supports the stoichiometry. Morphology of the adduct is varies with the stoichiometry of the molecular adduct. Ethylene polymerization reactions have been measured using different Mg/Ti ratios with all three different stoichiometry of the molecular adducts. MgCl$_2$.1.5THF molecular adduct derived active catalyst shows better activity compared to other stoichiometries of the molecular adducts. Activity results suggests the ethylene polymerization activity highly depend on the stoichiometry of the molecular adduct as supporting material and the Mg/Ti ratio of the active catalyst.

Part B: MgCl₂.2THFA

5.3. Results and Discussion

5.3.1 Powder X-ray diffraction
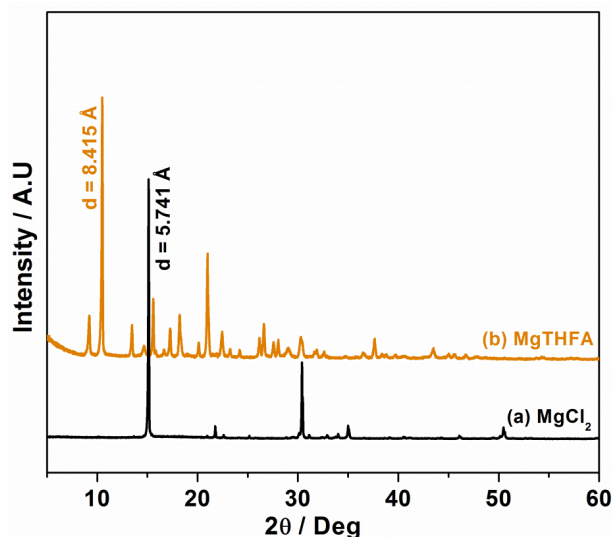
Figure 5.7: *Powder XRD pattern of (a) anhydrous MgCl₂, and (b) MgTHFA adduct.*

Powder X-ray diffraction pattern (PXRD) of catalyst precursor or MgTHFA molecular adduct is shown and compared with that of anhydrous $MgCl_2$ in Figure 5.7. Anhydrous $MgCl_2$ exhibiting rhombohedral cubic close packing with strong diffraction patterns for (003), (004), and (110) planes at $2\theta = 15.1°$, $35°$, and $50.4°$, respectively [37]. A strong diffraction peak appeared at $2\theta = 10.3°$ (d = 8.415 Å), which is higher than the d value $MgCl_2$ (d=5.741 Å). Higher value of d indicates the distance between the successive -Cl-Mg-Cl- layer is increased due to the adduct formation with Lewis base. The highly intense reflection of the feature at $2\theta = 10.3°$ and $20.6°$ clearly shows the growth of the crystal, in these present preparation method, occurs along (*00l*) planes. A strong diffraction feature at low 2θ for the MgTHFA adduct highlights the fact that the adduct exhibits a layered structure due to relatively weak interaction of the Lewis base along the *z*-axis. Though THFA molecules is bulkier than ethanol, smaller d value of MgTHFA (8.415 Å) compared to

MgEtOH (9.838 Å) indicates the interaction of Lewis base is likely to be a non-conventional manner (bi-coordination) [38].

5.3.2 Thermal Analysis
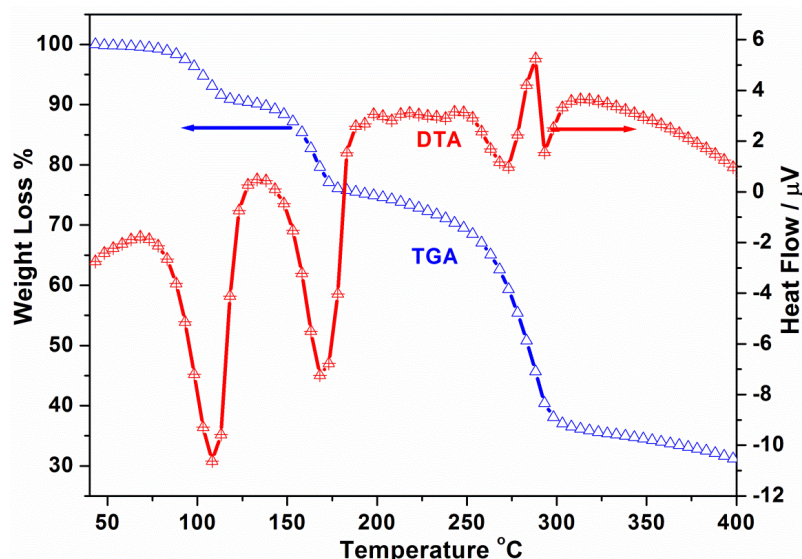
Figure 5.8: *Thermal analysis of MgTHFA adduct*

TG-DTA analysis of MgTHFA adduct is shown in Figure 5.8. Like usual molecular adducts with simple alcohols reported [37, 38], TG analysis shows step wise weight loss between 80 ^{o}C to 300 ^{o}C. TG analysis shows three distinct weight loss features. However, in DTA analysis, four endothermic peaks for the desorption of THFA molecules were observed. All reported $MgCl_2$ based molecular adduct systems shows weight loss only upto 250 ^{o}C; However, in MgTHFA case, the weight loss is observed upto 300 ^{o}C could be due to strong binding of Lewis base with Mg^{2+}. Since the Lewis base THFA molecule, consists both functional group (-OH and ether) interaction would be likely to be bi-coordinated. The absence of any weight loss above 300 ^{o}C indicates the presence of only $MgCl_2$, after dissociation of all THFA molecules. The THFA/$MgCl_2$ ratio was found to be two, from the experimental weight loss corresponding to 64.2%. Distinct features observed in TG-DTA could be due to the bifunctionalites associated with THFA molecule. Because of bifunctional group, the binding and hence desorption of molecules would be different, which leads to

three weight loss with TG and four features in DTA analysis. It is also to be noted that first two DTA features below 200 ^{o}C is strongly endothermic and the latter two DTA features are mild exothermic in nature. This also indicates a strong binding between THFA and $MgCl_2$ leads to the above latter features. Stoichiometry of the molecular adduct containing THFA also determined separately by liquid state NMR using a weighed amount of the [3] adduct in 1 mL of deuterated water containing known amount of a reference compound, methanol. The mole fraction of THFA is estimated from the ^{1}H integrals and used for the calculation of absolute amount of THFA in the adduct and found the stoichiometry is very close to $MgCl_2 \cdot 2THFA$.

5.3.3 Raman Analysis

Figure 5.9 shows the Raman spectra of MgTHFA, liquid THFA, and anhydrous $MgCl_2$. $MgCl_2$ belongs to the rhombohedral crystal system with layered structure with D_{3d} space group. The A_{1g} breathing mode of $MgCl_6$ octahedra appears as a high intense peak at 243 cm^{-1}. This is attributed to a distorted octahedron environment with Mg^{2+} coordinated to six chloride ions [39, 40]. Liquid THFA shows a strong peak for C−O stretching at 1010 cm^{-1}, a medium peak for the −CH$_3$ bending mode at 1445 cm^{-1}, a −C−H symmetric stretching peak at 2832 cm^{-1}, and a −C−H antisymmetric peak at 2941 cm^{-1} (not shown in Figure 5.9). Peak around 1245 cm^{-1} is due to CH$_2$ twist and δ(COH) modes. The adduct, MgTHFA, shows an extra peak at 708 cm^{-1}, in addition to the features observed for neat THFA. This specific Raman mode indicates the formation of Mg−O bond between $MgCl_2$ and THFA to form a MgO_6 octahedron [37, 38]. It is speculated that THFA interacts more strongly with $MgCl_2$ in bi-coordination from alcohol and ether functional group.
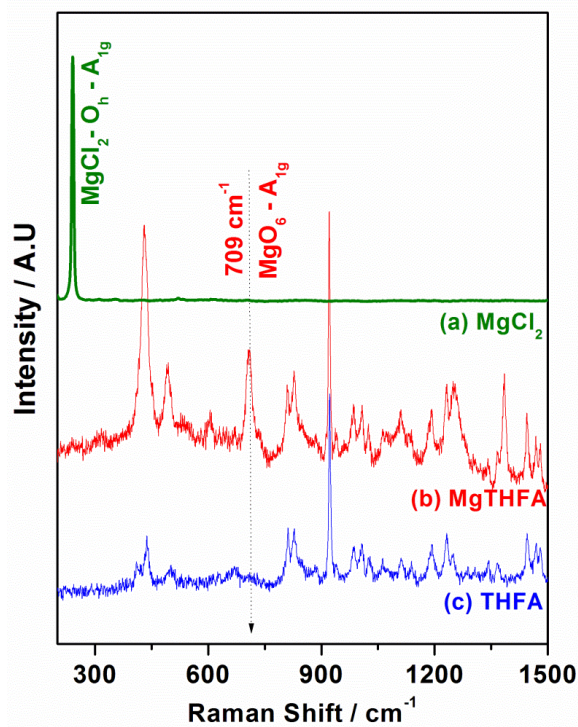
Figure 5.9*: Raman spectra of (a) MgCl₂, (b) MgTHFA and (c) liquid THFA.*

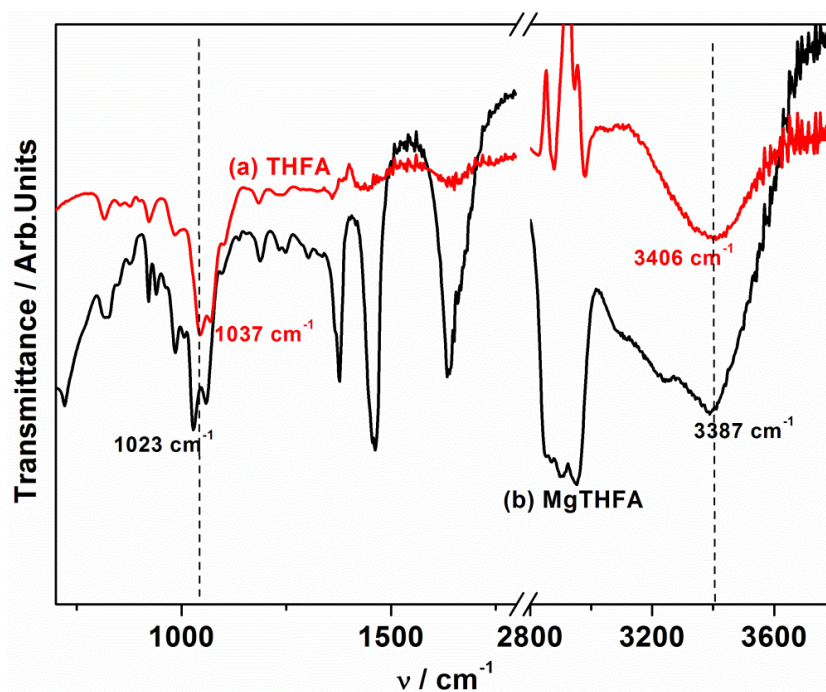### 5.3.4 Infrared spectroscopy analysis

Figure 5.9*: IR spectra of (a) THFA and (b) MgTHFA adduct.*

IR spectra of THFA and MgTHFA adduct are given in Figure 5.9. THFA molecule shows a peak at 3406 cm^{-1} due to O-H stretching. High intense peaks observed at 2980- 2900

cm^{-1} and 1500-1300 cm^{-1} for all samples are due to C-H stretching of nujol. Peak around 2900 cm^{-1} also arise from aliphatic C-H stretching of THFA. A peak at 1037 cm^{-1} is due to C-O stretching frequency. Similarly, MgTHFA adduct having the peaks at 3387 cm^{-1} (O-H stretching), 2950 cm^{-1} (aliphatic C-H stretching), 1023 cm^{-1} (C-O stretching) frequencies. From the above IR frequencies we could observe the lower shift frequencies for O-H (23 cm^{-1}) stretching and C-O (14 cm^{-1}) stretching vibrations with MgTHFA adduct. This observation demonstrates that the O-H and C-O-C group is strongly coordinated to MgCl$_2$. So when we used bifuctional Lewis base for the formation of molecular adduct, both functionalites are co-ordinating with Mg^{2+} centre.

5.3.5 Solid state NMR

Figure 5.10 shows ^{13}C CPMAS and HPDEC spectrum of MgTHFA adduct. Five types of carbon signals are expected for THFA molecule. However, ^{13}C CPMAS as well as HPDEC spectrum shows ten peaks with chemical shift values of 78.9, 77.9, 69.7, 68.1, 61.3, 60.8, 25.6, 24.5, 23.8 and 23.3 ppm. Therefore, the observation of ten NMR peaks in MgTHFA adduct demonstrates the presence of easily two different types of THFA molecules. These peaks could be assigned as follows: C2 peaks at 78.9 and 77.9 ppm, C5 peaks at 69.7 and 68.1 ppm, C1 peaks at 61.3 and 60.8 ppm, C4 peaks at 25.6 and 24.5 ppm, and finally 23.8 and 23.3. Absence of any extra peak in ^{13}C HPDEC clearly signifies that all the THFA molecules are strongly interacts with MgCl$_2$; in other words, there is no free THFA molecules in the adduct. However, intensity of the peaks in ^{13}C CPMAS and ^{13}C-HPDEC spectra were found to vary significantly. The intensities of one set of signals that are shielded were found to be weaker in the HPDEC spectrum. Due to the contact time dependency of intensities, the CPMAS spectrum need not provide quantitative information. Overall, from the NMR spectra two magnetically non-equivalent molecules were found to bind with MgCl$_2$ form the molecular adduct.
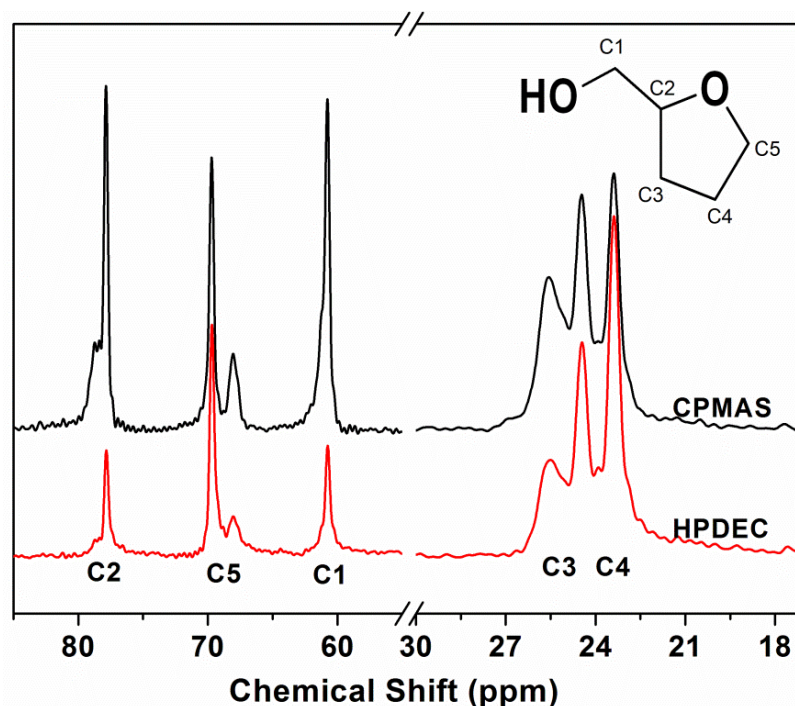
Figure 5.10: *¹³C CPMAS 75.5 MHz and HPDEC NMR spectra.*

5.3.6 SEM images
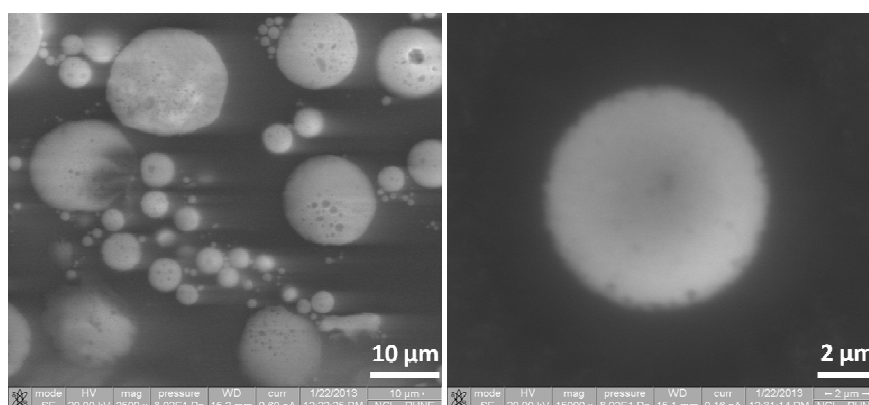
Figure 5.11: *SEM images of MgTHFA adduct.*

SEM images of MgTHFA adduct is shown in Figure 5.11. SEM images have been recorded in tri- block copolymer solution to avoid the degradation by the interaction with atmosphere. MgTHFA adduct particles are perfectly spherical in shape with size variation in the range of 5 μm to 30 µm. Closer look at the surface of the particles clearly confirms the pores present in the surface of the particle. In fact the surface of the particles is not smooth in

,

Table 5.2: *Ethylene polymerization results using active catalysts derived from MgCl$_2$.2THFA support.*

S.No	Support	Mg/Ti	Ti% (mmol)	Surface area m^2/g	PE Yield g/g of catalyst	Mw gmol^{-1}	MWD
1	MgCl$_2$.2THFA	2/1	50 (1.056)	13	1578	159980	7.2
2	MgCl$_2$.2THFA	5/1	20 (0.422)	7	2470	178900	6.4
3	MgCl$_2$.2THFA	10/1	10 (0.211)	15	3293	147056	5.3
4	MgCl$_2$.2THFA	15/1	6.6 (0.139)	17	1908	163738	6.7

nature. Porous nature of the surface would be an advantage for titanation of the molecular adduct.

5.3.7. Ethylene Polymerization

MgTHFA molecular adduct has been used as a support to prepare active Z-N catalyst with four different Mg/Ti ratio. Ethylene polymerization reactions have been conducted using Et_3Al as cocatalyst at 75 ^oC and 5 atm. Activity results of Z-N catalyst derived using MgTHFA adduct is shown in Table 5.2. Activity of the catalyst varies with different Mg/Ti ratio of the active catalyst. Among four different Mg/Ti ratios, active catalyst containing 10% Ti gives the highest yield of 3.3 kg of PE/g of catalyst. Lowest activity of the catalyst is found with 6.6% Ti containing catalyst. Even lowest MWD (5.3) of PE synthesized is obtained with 10%Ti containing catalyst. Overall, MWD of the PE obtained using the active catalyst derived from MgTHFA showing comparatively narrow MWD than other heterogeneous Z-N catalyst. Though the surface area of the active catalyst derived is much smaller than other reported heterogeneous catalyst, the activity of the catalyst is higher than commercial Z-N catalyst derived from MgEtOH. The above observations clearly confirm the bifunctionalites present with THFA molecular. This electron donor might be showing better control over the active sites present in the active catalyst, thereby leads to better control of MWD of the polymer obtained.

5.3.8. Conclusion

Single phase MgTHFA molecular adduct has been synthesized and subjected to series of thorough structural, spectroscopic and morphological studies. TGA and IR studies confirm the presence of two THFA molecule present in the molecular adduct and it coordinate with Mg^{2+} in bi-coordinated way. Raman data shows the presence of octahedral environment around Mg^{2+}. Ethylene polymerization results indicate the activity of the

prepared Z-N catalyst varies with titanium content presence. Though the surface area of the active catalyst is very less, synthesized Z-N catalyst shows better activity than commercial catalyst derived from MgEtOH supporting material. PE obtained using the MgTHFA derived catalyst shows lower MWD compared to other catalysts derived from different molecular adducts. This confirms the MgTHFA support exhibits better control over the active sites that leads to lower MWD of PE obtained.

5.4 Reference

1. Albizzati, E.; Giannini, U.; Collina, G.; Noristi, L.; Resconi, L. Catalysts and Polymerizations. In Polypropylene Handbook; Moore, E. P., Jr., Ed.; Hanser-Gardner Publications: Cincinnati, OH, 1996; Chapter 2, p11.
2. Kashiwa, N. *J. Polym. Sci., Part A: Polym. Chem.*, **2004,** *42,* 1
3. Sozzani, P.; Bracco, S.; Comotti, A.; Simonutti, R.; Camurati, I. *J. Am. Chem. Soc.* **2003**, *125,* 12881.
4. Cavallo, L.;Del Piero,S.; Duce´re´, J.M.; Fedele, R.; Melchior, A.; Morini, G.; Piemontesi, F.; Tolazzi, M. *J. Phys. Chem. C.,* **2007,** *111,* 4412.
5. Correa, A.;Piemontesi, F.; Morini, G.; Cavallo, L. Macromolecules **2007,** *40,* 9181.
6. Vanka, K.; Singh, G.; Iyer, D.; Gupta, V. K. *J. Phys. Chem. C.* **2010,** *114,* 15771.
7. Sobota, P. *Coord. Chem. Rev.* **2004,** *248,* 1047.
8. Busico, V.; Causa, M.; Cipullo, R.; Credendino, R.; Cutillo, F.; Friederichs, N.; Lamanna, R.; Segre, A.; Castellit, V. V. *J. Phys. Chem. C.* **2008,** *112,* 1081.
9. Kim, S. H.; Somorjai, G. A. *J. Phys. Chem. B* **2002,** *106,* 1386
10. Barbe´, P. C.; Cecchin, G.; Noristi, L. *Adv. Polym. Sci.* **1987,** 81,
11. Parodi, S.; Nocci, R.; Giannini, U.; Barbe´, P. C.; Scata, U. (Montedison S.p.A.). Eur. Pat. EP0045977, 1982.1.
12. Liu, T.; Nitta, T.; Nakatani, H.; Terano, M. *Macromol. Chem. Phys.* **2003,** *204,* 2412.
13. Liu, T.; Nitta, T.; Nakatani, H.; Terano, M. *Macromol. Chem. Phys.* **2003,** *204,* 395.
14. Andoni, A.; Chadwick, J. C.; Milani, S.; Niemantsverdriet, J. W.;Thüne, P. *J. Catal.* **2007,** *247,* 129.
15. Lee, M. Y.; Scott, S. L. *Chem. Eur. J.* **2011,** *17,* 4632.

16. Seenivasan, K.; Sommazzi, A.; Bonino, F.; Bordiga, S.; Groppo, E. *Chem. Eur. J.* **2011,** *17,* 8648.

17. Groppo, E.; Seenivasan, K.;Barzan, C. *Catal. Sci. Technol.,* **2013,** *3*, 858.

18. (a) Boero, M.; Parrinello, M.; Weiss, H.; Hu¨ffer, S. *J. Phys. Chem. A* **2001,** *105,* 5096. (b) Seth, M.; Margl, P. M.; Ziegler, T. *Macromolecules* **2002,** *35,* 7815. (c) Monaco, G.; Toto, M.; Guerra, G.; Corradini, P.; Cavallo, L. *Macromolecules* **2000,** *33,* 8953.

19. (a) Pino, P.; Rotzinger, B.; von Achenbach, E.; Keii, T.; Soga, K. In Catalytic Polymerization of Olefins, Proceedings of the International Symposium on Future Aspects of Olefin Polymerization, Tokyo, Japan, July 4-6, 1985; Keii, T., Soga, K., Eds.; Elsevier: Kodansha, Tokyo, 1986. (b) Cavallo, L.; Guerra, G.; Corradini, P. *J. Am. Chem. Soc.* **1998,** *120,* 2428. (c) Boero, M.; Parrinello, M.; Terakura, K. *J. Am. Chem. Soc.* **1998,** *120,* 2746. (d) Boero, M.; Parrinello, M.; Hu¨ffer, S.; Weiss, H. *J. Am. Chem. Soc.* **2000,** *122,* 501. Seth, M.; Ziegler, T. *Macromolecules* **2004,** *37,* 9191.

20. Thushara, K. S.; Gnanakumar, E. S.; Mathew, R.; Jha, R. K.; Ajithkumar, T. G.; Rajamohanan, P. R.; Sarma, K.; Padmanabhan, S.; Bhaduri, S.; Gopinath, C. S. *J. Phys. Chem. C* **2011,** *115,* 1952.4.

21. Valle, G.; Baruzzi, G.; Paganetto, G.; Depaoli, G.; Zannetti, R.; Marigo, R. *Inorg. Chim. Acta* **1989,** *156,* 157.

22. Sobota, P. *Chem. Eur. J*. **2003,** *9,* 4855.

23. Sobota, P.; Utko, J.; Lis, T. *J. Chem. Soc. Dalton Trans.* **1984,** 2077.

24. P. Sobota, Polyhedron 1992, 7, 715.

25. Mauret, P.; Alphonse, P. *J. Organomet. Chem.,* **1984,** *276*, 249.

26. Handlfr, K.; Holeckek, L.; Benes, L. *Collection Czechoslovak Chem. Commun.* **1985,** *50,* 2422.

27. Sarma, R.; Ramirez, F.; McKeever, B.; Chaw, Y. F.; Marecek, J.F.; Nierman, D.; McCaffrey, T. M. *J. Am. Chem. Soc.* **1977**, *99,* 5289.

28. Gordon D., Wallbridge M. G. H. *Inorg. Chirn. Acta.* **1984,** *88,* 15

29. Handlif K., Holecek J., Bocek V., Fiala Z., Gheorghiu M.: *Czech. Appl. PV* 2549-84.

30. Hamiltonr, P. M.; McBeth, R.; Bekebredea, W.; Sisler, H. **1953**, *75,* 2881.

31. Albizzati, E.; Giannini, U.; Morini, G.; Galimberti, G.; Barino, L.; Scordamaglia, R. *Makromol. Chem., Macromol. Symp.* **1995,** *89, 73.*

32. Morini, G.; Balbontin, G.; Gulevich, Y. V.; Vitale, G. (Basell Poliolefine Italia). Patent WO0230998, 2002.

33. Sobota, P.; Utko, J.;Brusilovets, A. I.;Jerzykiewicz, L. B. *J. Organomet. Chem.,* **1998,** *553,*379.

34. Sobota, p.; Utko, j.; Szafert, s.; Szczegot, K. *J. Chem. Soc., Dalton Trans.,* **1997,** 679.

35. Sobota, P.;Utko, J.;Ejfler, J.;Jerzykiewicz, L. B. *Organometallics,* **2000,** *19,* 4931.

36. Utko, J.;Przybylak, S.;Jerzykiewicz, L. B.; Szafert, S.;Sobota, P. *Chem. Eur. J.* **2003,** *9,* 181.

37. (a) Gnanakumar, E. S.; Thushara, K. S.; Bhange, D. S.; Mathew, R.; Ajithkumar, T. G.; Rajamohanan, P. R.; Bhaduri, S.; Gopinath, C. S. *Dalton Trans.* **2011,** *40,* 10936. (b) Thushara, K. S.; Gnanakumar, E. S.; Mathew, R.; Ajithkumar, T. G.; Rajamohanan, P. R.; Bhaduri, S.; Gopinath, C. S. *Dalton Trans.* **2012,** *41,* 11311. (c) Gnanakumar, E. S.; Thushara, K. S.; Gowda, R. R.; Raman, S. K.; Ajithkumar, T. G.; Rajamohanan, P. R.; Chakraborty, D.; Gopinath, C. S. *J. Phys. Chem. C.* **2012,** *116,* 24115. (d) Gnanakumar, E. S Gowda, R. R.; Srikanth,K; S. K.; Ajithkumar, T. G.; Rajamohanan, P. R.; Chakraborty, D.; Gopinath, C. S. *ACS Catal* **2013,** *3,* 303.

38. Thushara, K. S.; Gnanakumar, E. S.; Mathew, R.; Jha, R. K.; Ajithkumar, T. G.; Rajamohanan, P. R.; Sarma, K.; Padmanabhan, S.; Bhaduri, S.; Gopinath, C. S. *J. Phys. Chem. C* **2011,** *115,* 1952.

39. Ye, Z.-Y.; Wang, L.; Feng, L.-F.; Gu, X.-P.; Chen, H.-H.; Zhang, P.-Y.; Pan, J.; Jiang, S.; Feng, L.-X. *J. Polym. Sci., Part A: Polym. Chem.* **2002,** *40,* 3112.

40. Tewell, C. R.; Malizia, F.; Ager, J. W., III; Somorjai, G. A. *J. Phys. Chem. B* **2002,** *106,* 2946.

Chapter 6

Conclusions and Future Outlook

6. Conclusions and Future Outlook

This chapter summarizes the present thesis work and describes the conclusions and possible future implications drawn based on the work.

Chapter 1 provides a brief introduction about Z-N catalyst and its discovery. It describes the types of Z-N catalyst available today for olefin polymerization and briefly discuss about the mechanism involved in Z-N catalyst. Also this chapter touches upon the discovery of heterogeneous $MgCl_2$ supported Z-N catalyst discovery and its importance in the industrial production of polyolefin. A part of this chapter explains elaborately about different polymorphs of $TiCl_3$ and $MgCl_2$ and structural correlation among them. It also describes role of $MgCl_2$ as an active support in the activity. Two different kind of electron donor (Lewis base) i.e., third component in heterogeneous Z-N catalyst have also been described briefly. Role of electron donors on activity and stereospecificity of the catalyst by specifically binding with different surface sites of $MgCl_2$ thereby influencing the catalyst have been presented. Till to date, different generations of heterogeneous Z-N catalyst and its components has been described well. Also this chapter explains the challenges present for the scientific community towards understanding in heterogeneous Z-N catalyst. Finally it briefly describes the objective of the present thesis.

Chapter 2 mainly addresses the detailed procedures involved in the materials preparation methods. We employed azeotropic distillation method for the synthesis of well defined molecular adducts using different alcohol and ether molecule with anhydrous $MgCl_2$. To understand the complications in the complex catalytic system, each component has to be characterized thoroughly to understand the system at molecular level. Indeed this is one of the prime reasons for the preparation of above molecular adducts in a single phase to understand the role of MgCl2 and associated textural characteristics generated during the preparation of Z-N catalyst system. Titanation of the support and ethylene polymerization

procedure have also been dealt extensively. Theory and experimental procedures involved in relevant physicochemical and spectroscopic characterization techniques were discussed.

Chapter 3 deals with the molecular adduct derived from very simple Lewis base i.e., methanol. First, $MgCl_2.6CH_3OH$ single phase molecular adduct was characterized thoroughly by various structural, spectroscopic and morphological characterization techniques. The above mentioned molecular adduct was used as support to synthesize active Z-N catalyst. Titanated catalyst shows support in δ-$MgCl_2$ form with less crystalline in nature. Also active catalyst possesses type-IV H3- mesoporosity with narrow pore size distribution. Titanium content in the active catalyst was estimated to be 13%. The active catalyst was screened for ethylene polymerization under different reaction conditions with different alkyl aluminium as co-catalyst. Among many reactions, co-catalyst of Me_3Al at 75 ^{o}C and 5 atm conditions gave highest PE production with ~6 times higher than commercial catalyst PE production. With many other factors, nature of the pores, and in general associated textural properties of the catalyst was found to be the major reason for higher PE production with Me_3Al as co-catalyst.

Further, $MgCl_2.6CH_3OH$ support was dealcoholated under controlled N_2 flow at different temperatures to synthesize different stoichiometries of $MgCl_2.xCH_3OH$ molecular adduct. Stoichiometry of the $MgCl_2.xCH_3OH$ (x = 5.6, 2.3 and 1.3) adducts have been estimated by NMR and thermal analysis method. Variable temperature NMR experiments demonstrate the changing stoichiometry of the adduct, which also induces structural alterations. Active catalyst derived from the respective molecular adducts showing type-1V isotherm with H3 hysteresis. Titanium content present in the active catalyst varies with the stoichiometry around Mg^{2+}. Lowest titanium content present in the active catalyst (Ti-MgMeOH-105) exhibit the best catalytic activity among all active catalysts. Structure-activity correlation indicates surface area is not the only factor for the better activity. This

chapter concludes the importance of molecular adduct stoichiometry as an important factor in the design of better heterogeneous Z-N catalyst with tailored properties.

Chapter 4 is divided into three parts – **Part A**, **Part-B** and **Part-C**. In general this chapter deals with three different bulky Lewis base namely cyclohexanol, benzyl alcohol and 9-FM. **Part-A** deals with the single phase molecular adduct derived from cyclohexanol. Structural insights of adduct have been revealed by various spectroscopic and morphological characterization methods. NMR and Raman data show the presence of six cyclohexanol molecules in an octahedral environment around Mg^{2+} with magnetically non-equivalent CyOH molecules in a 1:1 ratio. Using this support, active Ziegler–Natta catalysts with very high surface area and evenly distributed titanium active species have been prepared. This final active catalyst Ti-CyOH exhibits much better performance in terms of activity and polymer property compared to commercial Ziegler–Natta catalyst. Multimodal porous nature of catalyst is apparently responsible for high activity. High activity observed with iso-butyl aluminium cocatalyst on Ti-MgCyOH suggests a possible structural integration, which would also make it electronically integrated. If this is true, higher and selective activity could be achieved with other polymerization reactions. Detailed structural and spectral studies are essential to understand the present catalyst system to increase and/or fine tune the activity.

Part-B describes Z-N support as $MgCl_2.PhCH_2OH$. A new single phase supporting material for Z–N catalysts with an aromatic alcohol (benzyl alcohol) adduct of $MgCl_2$ has been successfully synthesized and characterized by variety of analytical and spectroscopic characterization methods. Notably a stronger interaction between the Mg and O atoms of the OH groups of $PhCH_2OH$ is observed in structural studies and Raman spectra. The titanated MgBzOH catalyst has been characterized by variety of techniques. Polymerization activity results suggest the surface area of the catalyst is not an important criterion governing the polymerization activity. A significantly high Ti content on the final catalyst surface indicates

a strong interaction between the support and Ti, which reduces the specific activity of Ti towards polymerization

Part-C of Chapter 3 demonstrate 9-FM as Lewis base in heterogeneous Z-N catalyst. Mg-9FM-EtOH molecular adduct has been synthesized and subjected to detailed spectroscopic and structural investigations. In order to see the effect of 9-FM molecule as an internal donor, active catalyst have been synthesized by conventional and merely fixing $TiCl_4$ over the support and both the catalysts were subjected to further investigations. The textural properties of the active catalysts shows conventional synthesized catalyst have higher surface area than the latter. Ethylene polymerization reactions were carried with different co-catalyst and shows iBu_3Al as best cocatalyst for the above supported Z-N catalytic system. Polymerization results suggests conventionally synthesized catalyst showing ~4.5 times better activity than commercial Z-N catalyst and still better than merely fixed $TiCl_4$ over the Mg-9FM-EtOH support. However, latter catalytic system shows lowest MWD of PE obtained confirms the role of 9-FM as an internal donor in the catalytic system. Detailed studies confirms the less lability of iBu_3Al and contribution of macropores are the likely reasons for the conventionally synthesized to give higher polymerization activity and merely $TiCl_4$ fixed catalyst to yield lower MWD of PE.

Chapter 5 is divided into **Part A** and **Part-B**. **Part-A** deals with differnt stoichiometries of $MgCl_2.xTHF$ (x = 1.5, 2, 4) adduct synthesized by simple procedure. Structural, spectroscopic and morphological studies of the adducts have been carried out using PXRD, IR, TGA, solid state NMR. The proposed structures of the adduct using different ratios of $MgCl_2$/THF have been verified and concluded for the synthesized adducts. Different amount of Ti has been fixed on the respective stoichiometry of the adduct. Activity of the catalyst varied with titanium content and stoichiometry of the molecular adduct. Highest activity was found with $MgCl_2.1.5THF$ with titanium content of 10%. Activity

results clearly confirms the influence of the molecular adduct stoichiometry on the catalytic activity.

Part B deals with the molecular adduct derived from bifunctional (alcohol and ether group) Lewis base i.e., THFA. Similar to $MgCl_2.xTHF$ molecular adduct, $MgCl_2.2THFA$ adduct have also been characterized thoroughly by various physico-chemical characterization techniques. IR spectra confirms the co-ordination of alcohol and ether funtionalities with Mg^{2+}. Different amount of titanation has been prepared by simple stirring of $TiCl_4$ over $MgCl_2.2THFA$. Active catalysts have been screened for ethylene polymerization using Et_3Al as cocatalysts. Active catalyst having Ti content of 10% shows the best activity. Among all other polymerization reaction studies in this thesis, active catalyst synthesized using $MgCl_2.2THFA$ support shows the lowest MWD of 5.3. Lowest MWD could be due to well controlled active sites formed by the help of bifuntional molecular adducts.

Though heterogeneous Z-N catalyst system for olefin polymerization is technologically well advanced, many aspects in the complex multi component catalytic system is yet to be studied. This thesis tried to address some of the fundamental aspects to understand the complicated system, particularly $MgCl_2$ based supporting molecular adducts. Outcome of the thesis clearly describes that by changing the nature of Lewis Base in $MgCl_2.xLB$, porosity and electronic structure of the active catalyst can be varied and thereby change in the olefin polymerization activity as well as the polymer properties could be obtained. The thesis wok can be extended in future to obtain more insights on the complex heterogeneous Z-N system.

❖ All the synthesized $MgCl_2$ based supporting material and active catalyst could be used in different polymerization reactions like propylene, hexane, 1,3-butadiene etc. polymerization reactions

- ❖ Mixture of different alcohols can be used in the molecular adduct to engineer the porosity and electronic structure of the active catalyst there by fine tune the polymerization activity of the catalyst.

- ❖ Spectroscopic studies could be conducted to better understand the role of co-catalyst (alkyl aluminium) in the active sites formation and the oxidation state of Ti^{n+} present in the active catalyst.

- ❖ Other internal donors could be used in the $MgCl_2$ base molecular adduct formation and there by its influence in the steroselective polymerization.

- ❖ Immobilization of active catalyst on the well-defined synthesized molecular adducts there by attaining single-site heterogeneous Z-N catalyst.

List of Publications

1. Toward an Understanding of the Molecular Level Properties of Ziegler-Natta Catalyst Support with and without the Internal Electron Donor. K. S. Thushara, **Edwin S. Gnanakumar,** Renny Mathew, Ratnesh K. Jha, T. G. Ajithkumar, P. R. Rajamohanan, Krishna Sarma, Sudhakar Padmanabhan, Sumit Bhaduri, and Chinnakonda S. Gopinath, *J. Phys. Chem. C* **2011,** *115,* 1952-1960.

2. $MgCl_2.6PhCH_2OH$ – A new molecular adduct as support material for Ziegler–Natta catalyst: synthesis, characterization and catalytic activity. **Edwin S. Gnanakumar,** K. S. Thushara, Deu S. Bhange, Renny Mathew, T. G. Ajithkumar, P. R. Rajamohanan, Sumit Bhaduri and Chinnakonda S. Gopinath, *Dalton Trans.,* **2011,** *40,* 10936-10944.

3. $MgCl_2·4((CH_3)_2CHCH_2OH)$: A new molecular adduct for the preparation of $TiClx/MgCl_2$ catalyst for olefin polymerization, K. S. Thushara, **Edwin S. Gnanakumar,** Renny Mathew, T. G. Ajithkumar, P. R. Rajamohanan, Sumit Bhaduri and Chinnakonda S. Gopinath, *Dalton Trans.,* **2012,** *41,* 11311-11318.

4. γ-$Al_{2-x}M_xO_{3\pm y}$ (M = Ti^{4+} through Ga^{3+}): potential pseudo-3D mesoporous materials with tunable acidity and electronic structure, Thomas Mathew, Kumarsrinivasan Sivaranjani, **Edwin S. Gnanakumar,** Yusuke Yamada, Tetsuhiko Kobayashi and Chinnakonda S. Gopinath, *J. Mater. Chem.,* **2012,** *22,* 13484-13493. **(Cover Page).**

5. $MgCl_2·6C_6H_{11}OH$: A High Mileage Porous Support for Ziegler–Natta Catalyst, **Edwin S. Gnanakumar**, K. S. Thushara, Ravikumar R. Gowda, Sumesh K. Raman, T. G. Ajithkumar, P. R. Rajamohanan, Debashis Chakraborty, and Chinnakonda S. Gopinath, *J. Phys. Chem. C* **2012,** *116,* 24115−24122.

6. $MgCl_2.6CH_3OH$: A Simple Molecular Adduct and its Influence as Porous Support for Olefin Polymerization, **Edwin S. Gnanakumar,** Ravikumar R. Gowda, Shrikant Kunjir, T. G. Ajithkumar, P. R. Rajamohanan, Debashis Chakraborty and Chinnakonda S. Gopinath, *ACS Catalysis* **2013,** *3,* 303-311.

7. Functional and Disordered Meso-Macroporous γ-$Al_{2-x}M_xO_{3\pm y}$ (M = Cu and/or Ce), **Edwin S. Gnanakumar,** Jino C. John, Thirumalaiswamy Raja and Chinnakonda S. Gopinath, *J. Nanosci. Nanotechnol.* **2013,** *13,* 2682-2688.

8. Rational Response and stable performance of $CuFe_2O_4$–mesoporous Alumina nanocomposite for high temperature water gas shift reaction, Vijayanand Subramanian, **Edwin S. Gnanakumar,** Dae Woon Jeong, Won-Bi Han, Chinnakonda S. Gopinath, Hyun-Seog *Chem. Commun. (Submitted).*